Vera C. Rubin Observatory
Systems Engineering

LSST Camera Electro-Optical Test Results

The LSST Camera group: Pierre Antilogus, Pierre Astier, John Banovetz, Seth Digel, Thibault Guillemin, Sean MacBride, Stuart Marshall, Andrew Rasmussen, Aaron Roodman, Yousuke Utsumi,

SITCOMTN-148

Latest Revision: 2025-01-08

D R A F T

Abstract

This note collects results from the LSST Camera electro-optical testing prior to installation on the TMA. We describe the CCD and Focal Plane optimization and the resulting default settings. Results from eopipe are shown for standard runs such as B-protocols, Dense and SuperDense PTCs, gain stability, OpSim runs of Darks, and Darks with variable delays. We also describe features such as e2v Persistence, ITL phosphorescence in coffee stains, remnant charge near Serial register following saturated images, vampire pixels, ITL dips, and others.

Change Record

Version	Date	Description	Owner name
1	YYYY-MM-DD	Unreleased.	

Document source location: https://github.com/lsst-sitcom/sitcomtn-148

Contents

LSST Camera Electro-Optical Test Results

1 Electro-optical setup

1.1 Run 7 Optical modifications

For Run 7 in the white room on Level 3 our electro-optical test setup had a few differences from the Run 6 setup in IR2 at SLAC. One difference was that we were not able to use the CCOB Narrow/Thin beam because we did not have the resources or expertise to configure it. As such, the majority of the testing was done with the CCOB Wide Beam projector. We did obtain an additional projector, the 4k projector, partway through Run 7 that will be discussed later. With the CCOB Wide Beam, we used a cone attached to the L1 cover as well as a shroud to create a dark environment (Fig. 1).
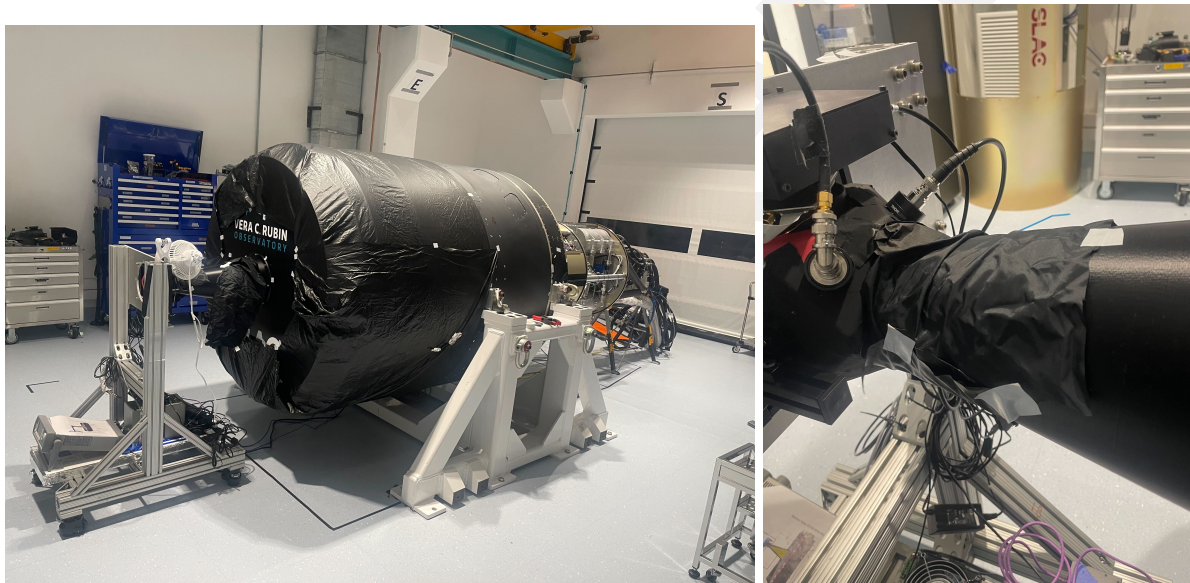
Figure 1: (left) Final shroud configuration of LSSTCam in Level 3 to reduce light leaks. (right) CCOB Wide Beam attached to the cone and shrouded.

This allowed us to operate on Level 3 with a dark current of <0.1 ADU/sec with the shutter open. The initial setup of the CCOB Wide Beam projector was the same as for Run 6, with a minimal ND filter (10 %) attached to a C-mount lens. One difference was that the f/stop of the lens was changed from 2.6 to 1.6 (fully open). This was done to try to reduce the effect of the 'weather' and the 'CMB pattern' two effects that we found in Run 6 and were found to be due to our projection setup (see [Banovetz2024]). While changing the f/stop did reduce the weather pattern, it also caused a much steeper illumination roll-off across the focal plane. We evaluated the weather pattern and illumination roll-off relative to Run 6.

To both reduce the effect of the 'weather' and 'CMB' but retain uniform illumination across the focal plane, we installed a diffuser in the cone attached to L1. Figure 2 shows the placement of the diffuser within the cone.
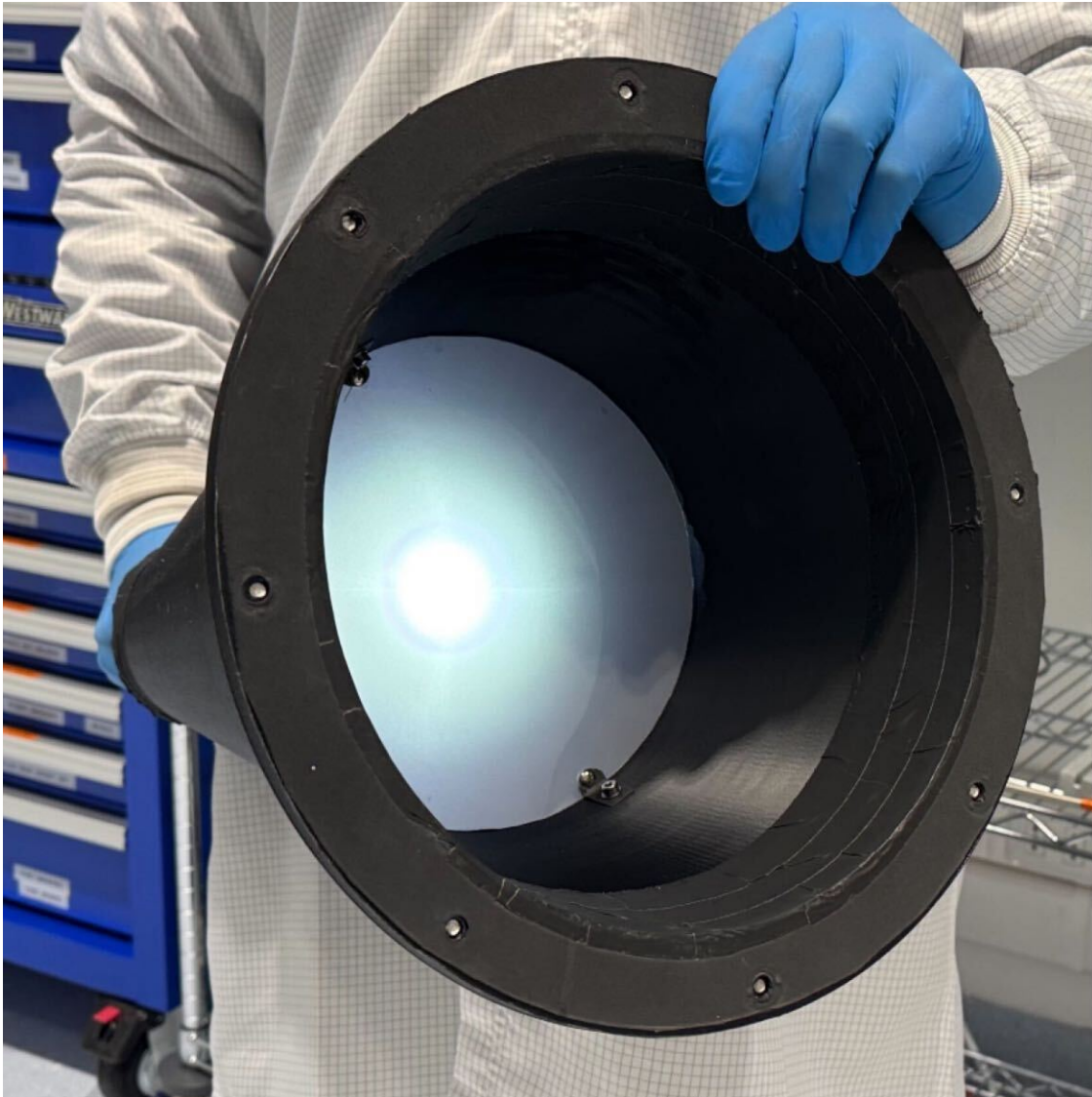
Figure 2: Diffuser installed into the light cone.

The diffuser combined with a fully open f/stop effectively reduced the incoming light by roughly 35%. Adjusting for that, we found that it greatly reduced the 'weather' (Fig. 3) and eliminated the CMB pattern, and more uniformly illuminated the focal plane (Fig. 4).

The diffuser was installed for all B protocol and PTC runs moving forward, being taken out only for pinhole projection runs and when using the 4K projector.
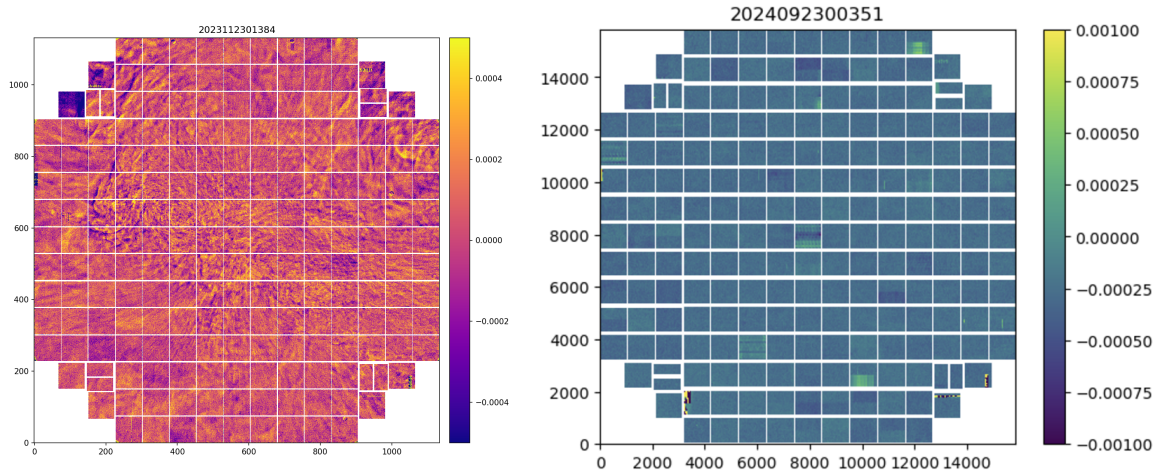
Figure 3: Full focal plane fractional difference images for Run 6 (left) and Run 7 (right).
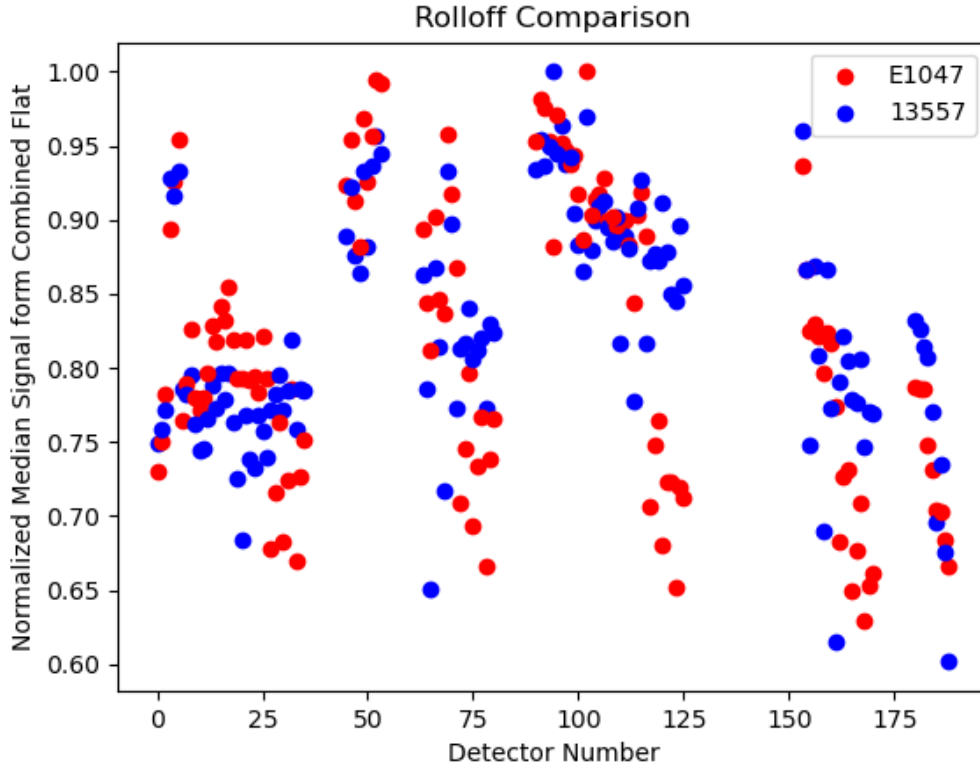
Figure 4: Illumination across the focal plane from Run 7 with the diffuser as compared to Run 6.

The addition to the projectors used for EO testing was a 4K projector, similar to those used in conference rooms. This projector was first tested at SLAC and arrived at the observatory about halfway through Run 7. It was used primarily as a spot projector, as the pinhole filter was not operational but more importantly, it could illuminate all 3206 amplifiers instead of the 21 illuminated by the pinhole projector. Most runs included the spots and the spot fluxes were controlled by the LSSTCam shutter instead of any flashing (e.g., CCOB Wide Beam). One downside that was found was that the projector illuminated the entire focal plane at some background level, not just the spot regions. The background illumination also had structure that changed with time and could not be easily subtracted. The resulting contrast between the spot and the background was only about a factor of 6. Changing the spot shape to large rectangles for crosstalk measurements increased the contrast ratio to 30.

1.2 Projector spots

This section describes the spots and rectangle patterns used for tests with the 4k projector.

- Projector background
- Spots on many amps
- Spots on one amp
- Optical setup

1.3 Dark current and light leaks

This section describes dark current and light leaks in Run 7 testing.

1.3.1 Light leak mitigation with shrouding the camera body

One of the first tests we attempted with LSSTCam was measuring dark current and sources of light leaks in the camera body. Before beginning we covered gaps between the L1 cover and the gaskets with tape, in locations where we felt comfortable applying it. Below shows the gaps that we could see between L1 and its cover.

Once these were sealed, we took some initial measurements and then started to cover the LSSTCam body with a shroud of .... Figure 5 shows the final shroud configuration covering the camera. We also found light leaks where the light cone attached to L1 was housed, and from the Utility Trunk.

Table 1 includes the observations, the corresponding measured dark currents, and comments on what changed during the leak chasing.

Figure 5: Final shroud configuration of LSSTCam in Level 3 to reduce light leaks.

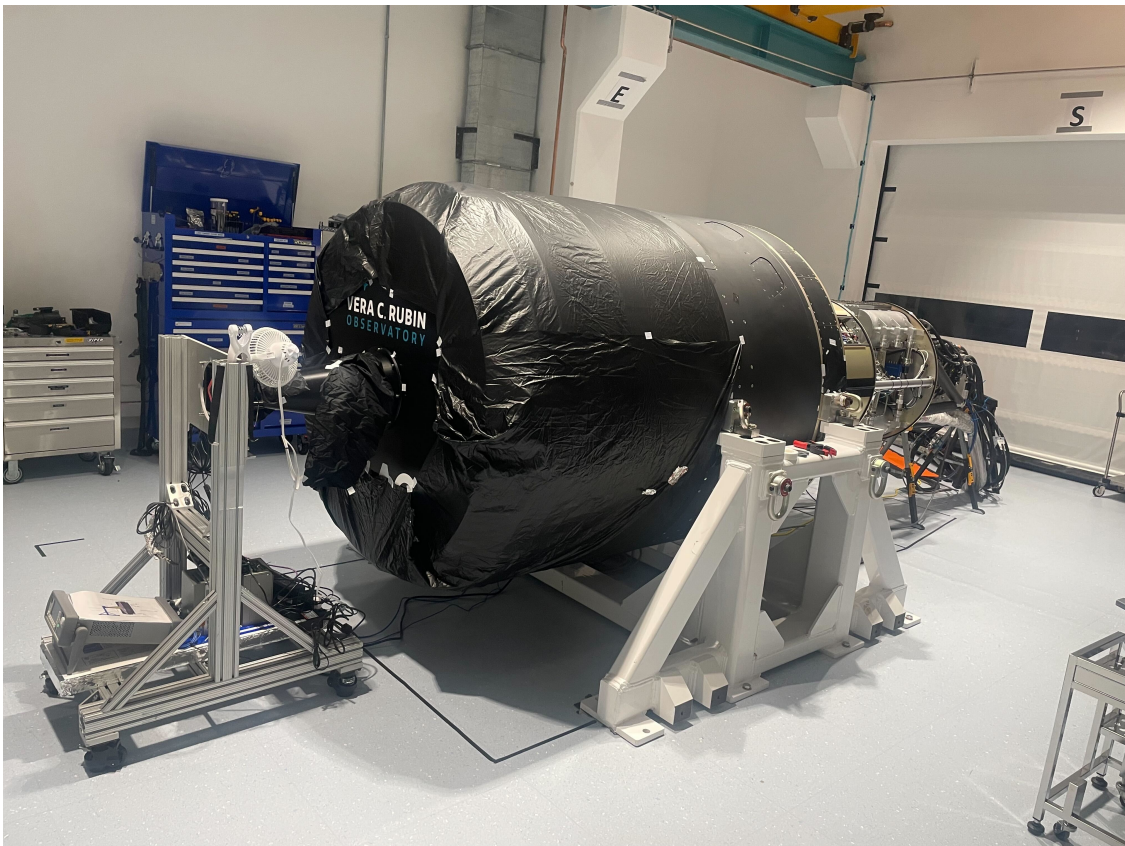Table 1: Summary of the 15 s dark exposures, the different conditions, and the resulting dark current. Exposure ID is preceded by "MC_C202409". The shroud was in place for each of these measurements. ("Initial Covering" was just the CCOB cone and around the L1 cover.)

Exposure	Dark Current	Room Lights	Shutter	Comments
09_000012	0.158	Off	Closed	
09_000018	0.158	On	Closed	
09_000038	2.94	On	Open	Initial Covering
09_000054	1.34	On	Open	+ Blanket over the FCS
09_000072	0.41	On	Open	+ Blanket over AND under the FCS
09_000078	0.18	Off	Open	+ Blanket over AND under the FCS
10_000031	0.033	On	Open	+ Blanket over AND under the FCS + UT

1.3.2 Filter Exchange System Autochanger light leak masking

A dedicated light leak study of the Filter Exchange System (FES) Autochanger (AC) was performed during Run 6 at SLAC in summer 2023 and a localized faint light source of up to ~0.04 e/s/pix was found to be associated with the 24 V Clean of the AC.

In the AC this voltage is used to power some probes and all controllers. In February 2024, as AC-1 was extracted from LSSTCam for global maintenance, a direct investigation to localize the light source was performed unsuccessfully. A light source in the AC was not expected, as in the AC all controllers' LEDs have been removed, and most electronics are in "black boxes". Still, two small probes, which had LEDs that could not be removed, were initially masked by a black epoxy. As we had doubts about the quality of this masking at IR wavelengths, we applied extra masking (aluminum black tape) on them during the Feb 2024 maintenance (on AC 1 and 2).

At the start of Run 7 a new study of the light leak based on 900 s dark exposures with the shutter open and the empty frame filter in place, showed that the AC light leaks were still present (see left hand image of Fig. 6). Following this finding, a full review of all the AC hardware powered by the 24 V dirty was performed, and a candidate was found: the encoders of the five main motors of the AC had only partial documentation from the vendor that did not mention the presence of LEDs. After interaction with the vendor, the encoders were understood to contain ~700 nm LEDs. The hypothesis of ~700 nm LED sources has been found compatible with the observation as no AC light leaks were detected using various filters (g, r, and y) in LSSTCam at the start of Run 7 (g, r, and y filters). A dedicated test in Paris using an AC spare encoder and a precision photometric set-up allowed identification of the leak in the masking of those LEDs in the vendor packaging. A complementary masking method based on a 3D printed part + tape + cable tie was qualified in

Paris. It was found to mask the light leak and to be safe (all parts correctly secured).

In November 2024, we masked all the lights in the back of the Level 3 white room (not the part containing LSSTCam) to set up a high-quality dark room allowing a direct observation with a CMOS camera of the light leak on the AC2 motor encoders. The level of darkness reached allowed us to validate the quality of the light masking of the AC encoders. Notice that the FES-prototype in Paris does not have encoders on the Online Clamps, so we had to tune/qualify the masking of those encoders directly on the AC 2 at the summit.

For both AC 1 and 2, the encoders of the five motors with the vendor issue on their LED masking have been successfully enveloped in a light-tight mask.

We note that the AC was turned off starting on 27 September 2024 at 21:15 UTC in the first part of Run 7. For the second part of Run 7 (i.e., after mid-November) the AC was back on: as the AC 1 was back in LSSTCam with the new light masks in place on the motor encorders, we were able to take a new series of 900 s darks with the AC turned on and off, confirming that the light leak associated with the FES was eliminated (see right hand image of Fig. 6).
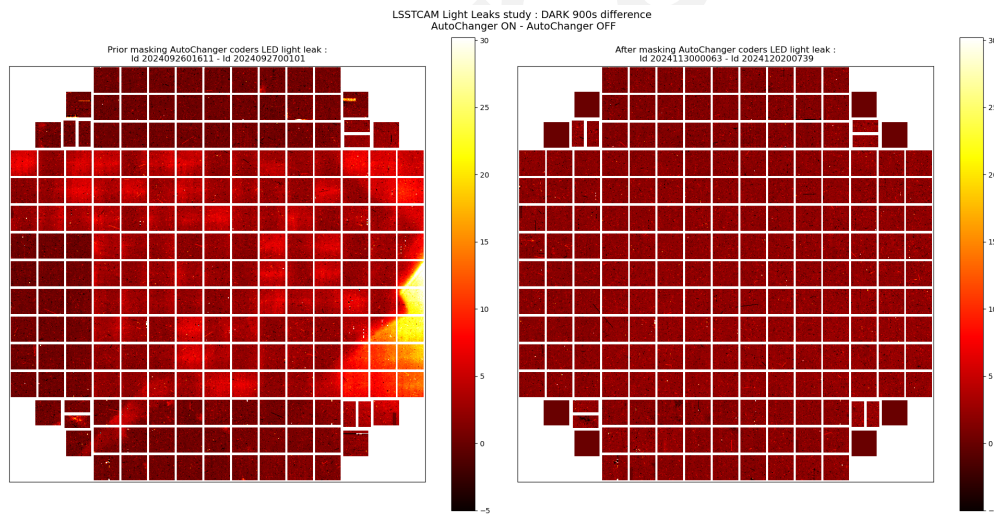

Figure 6: (left) The original impact of the AC light leak on a 900 s dark difference image (AC on minus AC off). (right) The result after masking the LEDsc of the motor encoders in the AC. No light associated with the FES is present in 900 s dark difference image.

1.3.2.1 Shutter condition impact on darks

1.3.2.2 Filter condition impact on darks

1.3.3 Final measurements of dark current

2 Reverification

All electro-optical (EO) camera test data is processed through the calibration products and electro-optical pipelines to extract key metrics from the data run. The key camera metrics from Run 7, and their comparison to previous runs are discussed below.

The naming of the EO runs was established during initial LSSTCam integration and testing. The final SLAC IR2 run from November 2023 was named "Run 6", while the data acquisitions from Cerro Pachon beginning in October 2024 are considered "Run 7." Additionally, individual EO acquisitions are tagged with a run identifier. This is commonly referred to as a Run ID. For all SLAC runs, the run identifier was a five digit numeric code, while the Cerro Pachon runs were "E-numbers" that started with a capital E followed by a numeric code.

Among the motivations for these measurements, the primary concern is whether LSSTCam has maintained its performance characteristics between Run 6 and Run 7.

2.1 Background

Initial characterization studies performed on LSSTCam during Run 7 primarily used two image acquisition sequences.

- B protocols: this acquisition sequence consists of the minimal set of camera acquisitions for electro-optical testing, including
  - Bias images
  - Dark images
  - Flat pairs - flat illumination images (flats) taken at varying flux levels
  - Stability flats - flats taken at constant flux levels
  - Wavelength flats - flats taken with different LEDs
  - A persistence dataset - a saturated flat, followed by several darks
- PTCs (photon transfer curves): this acquisition sequence consists of a sequence of flat pairs taken at different flux levels. The flat acquisition sequence samples different flux levels at a higher density than the B protocol flat sequence, enabling more precise estimates of flat pair metrics including pixel covariances (see Fig. 7).
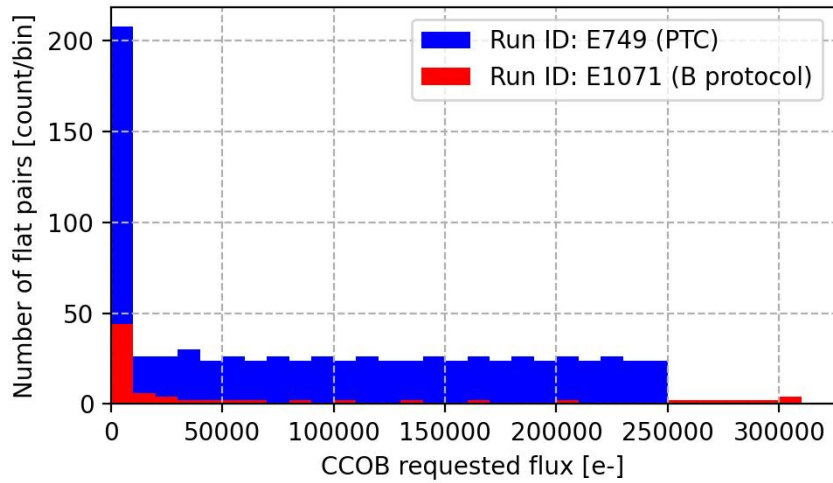
Figure 7: Flat-pair comparison between PTC and B protocol

For comparisons between Cerro Pachon EO runs and the final SLAC IR2 equivalents, the following runs are used (see Table 2).

Run Type	Run 6	Run 7
B Protocol	13557	E1071
PTC	13591	E749

Table 2: Reference runs for Run 6 and Run 7 comparisons

2.2 Stability flat metrics

2.2.1 Charge transfer inefficiency

CTI, or charge transfer inefficiency, measures the fraction of charge that fails to transfer from row to row during readout, and appears as trailing charge in the image area. Consequences of high CTI include loss of charge, distorted signals in the direction of parallel transfer, and reduced sensitivity in low light imaging. CTI measurements are made using the EPER method [EPER], for which the ratio of the residual charge in the overscan pixels to the total signal charge in the imaging region is evaluated. In the context of LSSTCam, we measure CTI along both the serial and parallel directions.
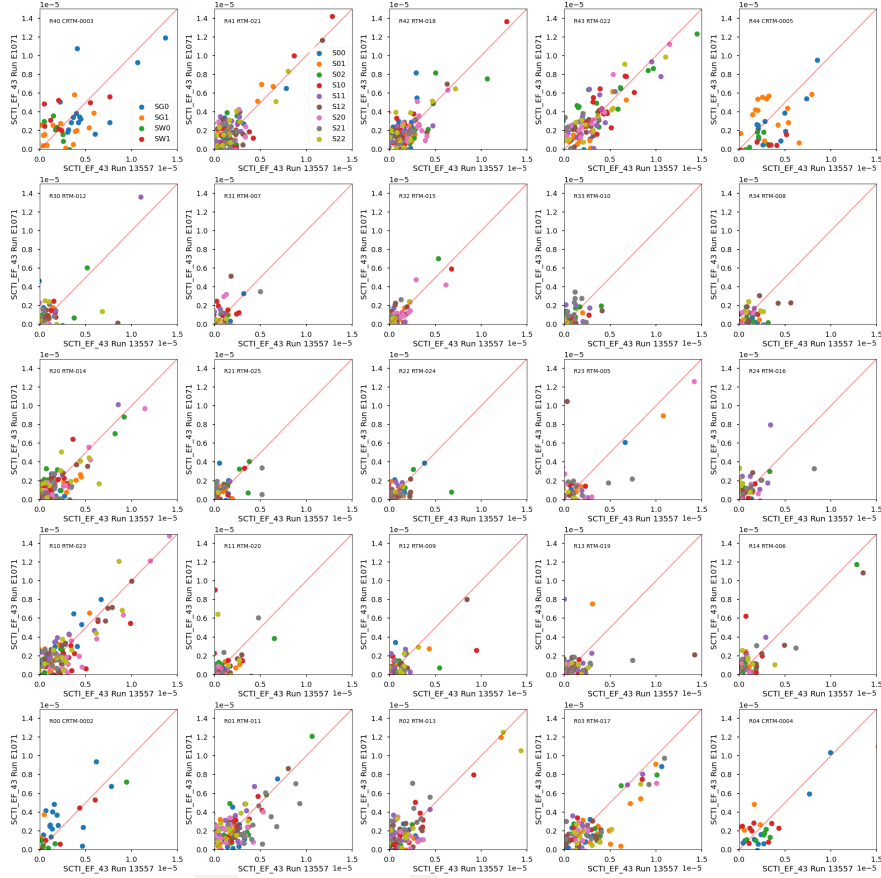
Figure 8: Serial CTI comparison by raft for Run 7 (E1017) and Run 6 (13557)

2.2.1.1 Serial CTI The CTI along the serial registers of the amplifier segments of the LSST-Cam CCDs is consistent between Run 6 and Run 7 (Fig. 8). Both sensor types show extremely low CTI on the order of 10^3 %, and span a range of ~2 » 10^5 % for e2v sensors, and by ~4 » 10^6 % for ITL sensors (Fig. 9).
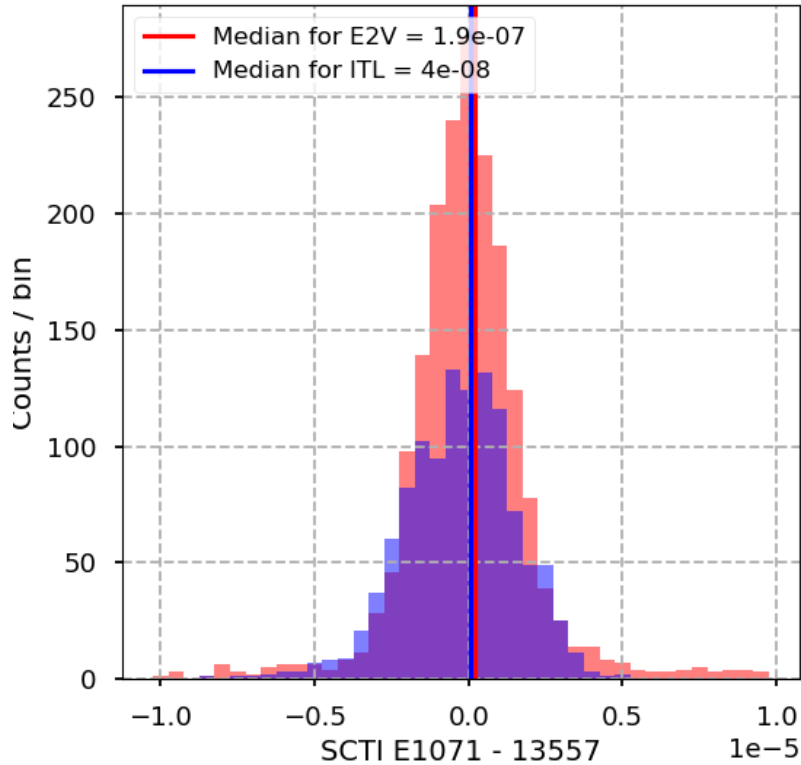
Figure 9: Distributions of differences in serial charge transfer inefficiencies between Run 7 (E1071) and Run 6 (13557), grouped by CCD type.

2.2.1.2 Parallel CTI The CTI along the parallel direction is consistent between Run 6 and Run 7 as well (Fig. 10). Both sensor types are found to have extremely low CTI on the order of 10^5 %, and span a range of ~2 » 10^7 % for e2v sensors, and by ~7 » 10^6 % for ITL sensors (Fig. 11).
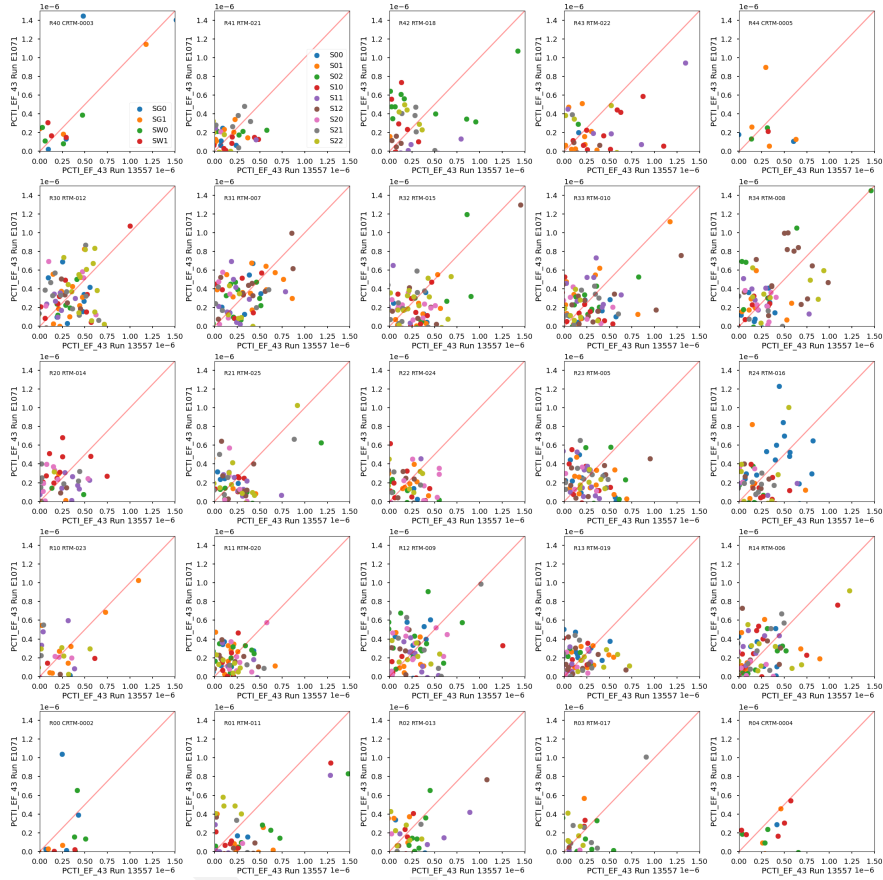
Figure 10: Parallel CTI comparison by raft for Run 7 (E1017) and Run 6 (13557).
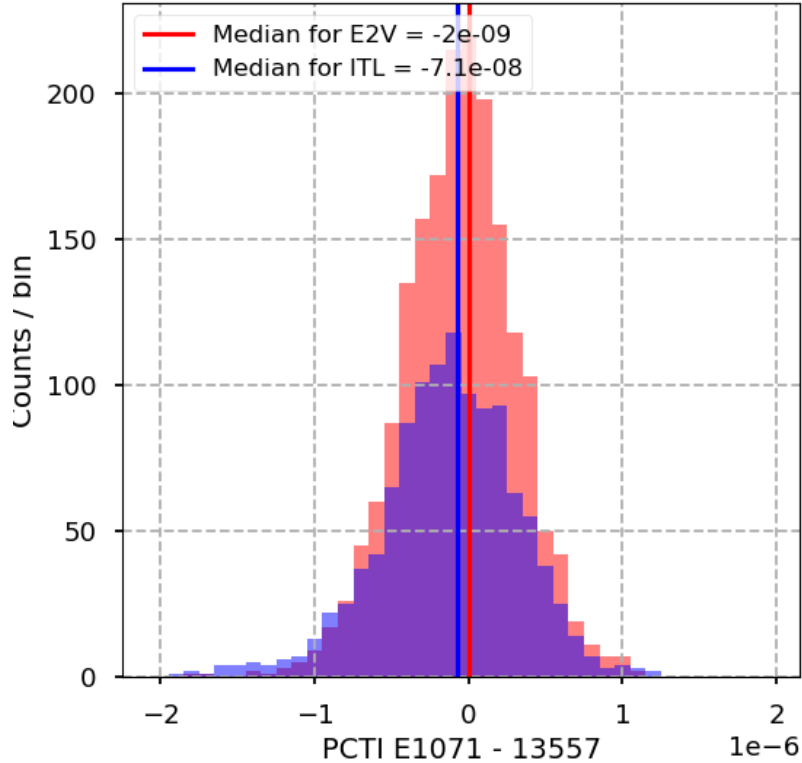
Figure 11: Distributions of differences in parallel charge transfer inefficiencies between Run 7 (E1071) and Run 6 (13557), grouped by CCD type.

2.3 Dark metrics

2.3.1 Dark current

Dark current is the small amount of electrical charge generated in the absence of light due to thermal activity within the semiconductor material of a CCD. This effect occurs when electron/hole pairs are thermally released into the conduction band in the CCD, mimicking the signal that light would produce. Dark current increases with temperature, so cooling the CCD is a common method to reduce it in sensitive imaging applications. Dark current introduces noise into an image, degrading its quality, particularly in low-light conditions or long exposures. In the context of LSSTCam, we measure dark current from the combined dark images across all amplifiers.
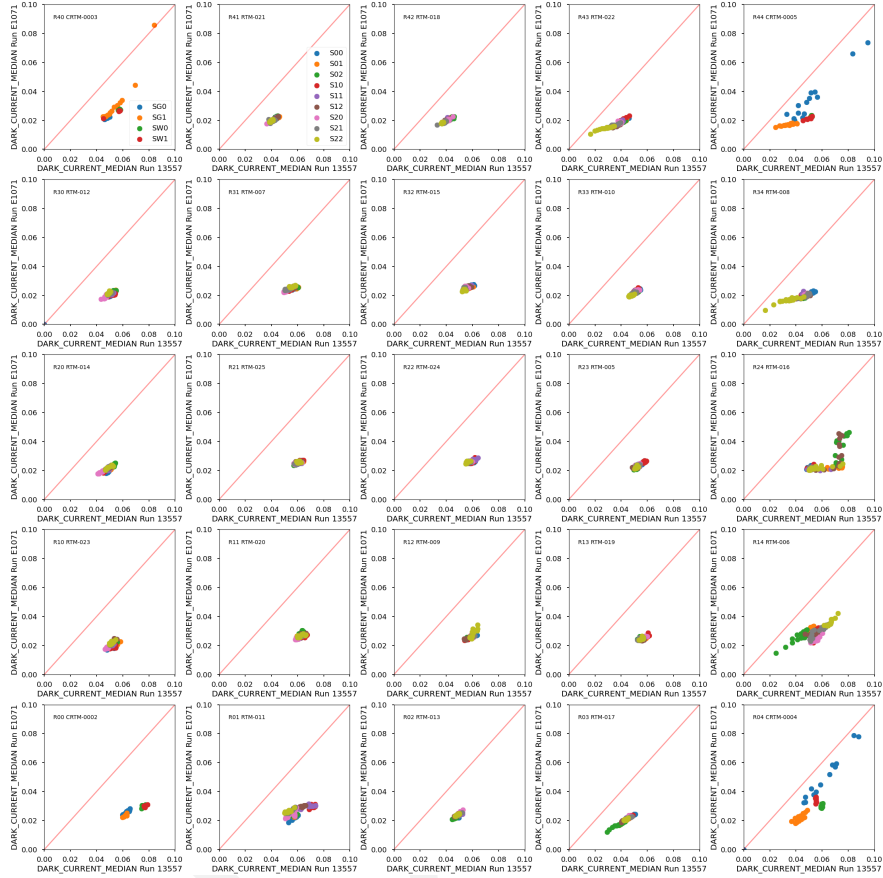
Figure 12: Dark current comparison by raft for Run 7 (E1017) and Run 6 (13557).

Unexpectedly, the dark current was significantly less in Run 7 than Run 6 (Fig. 12). A possible reason for this could be improved shrouding on the camera in the Level 3 white room relative to the IR2 clean room SLAC.

2.3.2 Bright defects

Bright defects are localized regions or individual pixels that produce abnormally high signal levels, even in the absence of light. These defects are typically caused by imperfections in the semiconductor material or manufacturing process of the CCD. Bright defects can manifest as "hot pixels" with consistently high dark current, small clusters of pixels with elevated dark current, or as "hot columns" (pixels along the same column that have high dark current). In the context of LSSTCam, we identify and exclude bright pixels from the dark current measurement, with the threshold for a bright defect set at 5 e/pix/s, above which the pixel/cluster/column is registered as a bright defect. In addition to the bright pixel metric, eo-pipe also computes a bright column metric, which is any region of bright pixels that is contiguous over 50 pixels or more.
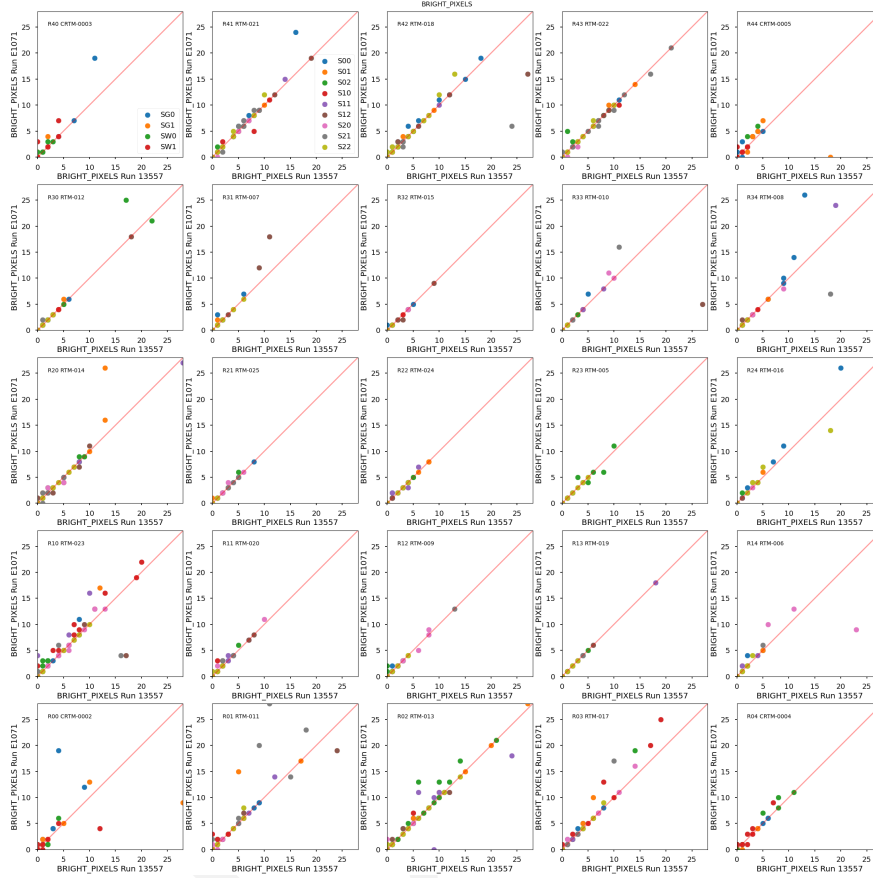
Figure 13

Evaluating the change in defect counts on each amplifier segment between Run 6 and Run 7, and aggregating the amplifiers by the detector manufacturer shows a small increase of bright defects in Run 7 (Fig. 14). For ITL sensors, we find that 12% of the amplifiers have more bright pixels than in Run 6. For e2v sensors, we find 4% of the amplifiers that have more bright pixels. Despite this, the number of bright defects between runs does not increase for most sensors.
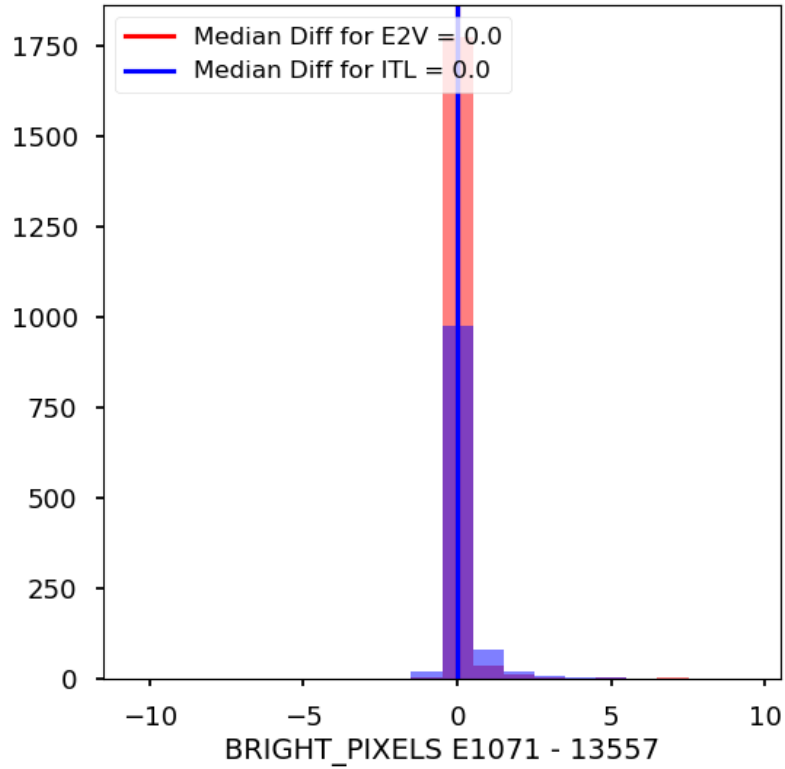
Figure 14: Distributions of differences in bright pixel count per amplifier between Run 7 (E1071) and Run 6 (13557), grouped by CCD type.

2.4 Flat pair metrics
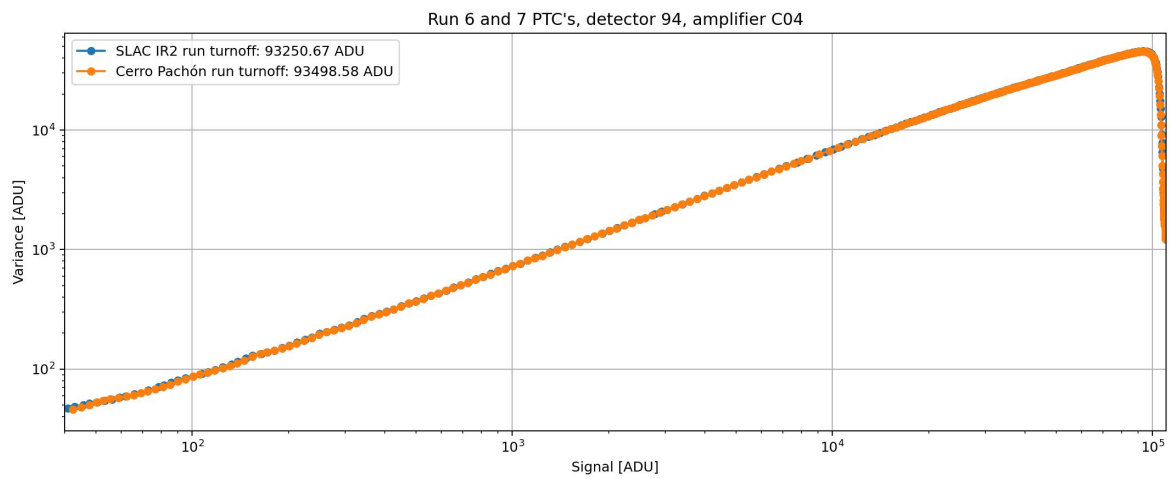
2.4.1 Linearity and PTC turnoff

Linearity turnoff and PTC turnoff are two closely related metrics used to characterize the upper limit of the usable signal range for accurate shape measurements and photometry. Linearity turnoff is the signal level above which the PTC curve deviates from linearity and is measured for each amplifier segment of each CCD. We have defined the deviation threshold as 2%. PTC turnoff refers to the high-signal region of the PTC above which the PTC variance decreases with increasing signal. This is due to saturation within the pixel wells of the CCDs. While slightly different, both metrics provide important information about the upper limits of the dynamic range in our sensors. Linearity turnoff is measured in units of e, while PTC turnoff is measured in ADU.
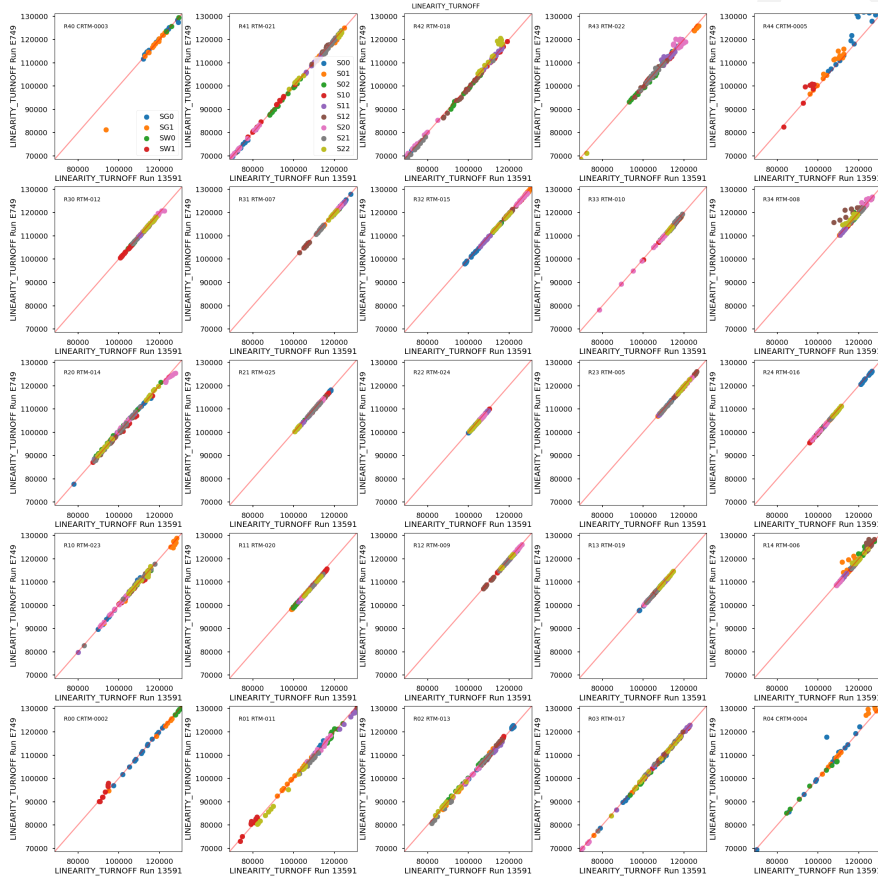
In our linearity turnoff measurements, we find close agreement between our Run 7 and Run 6 measurements for both ITL and e2v sensors.
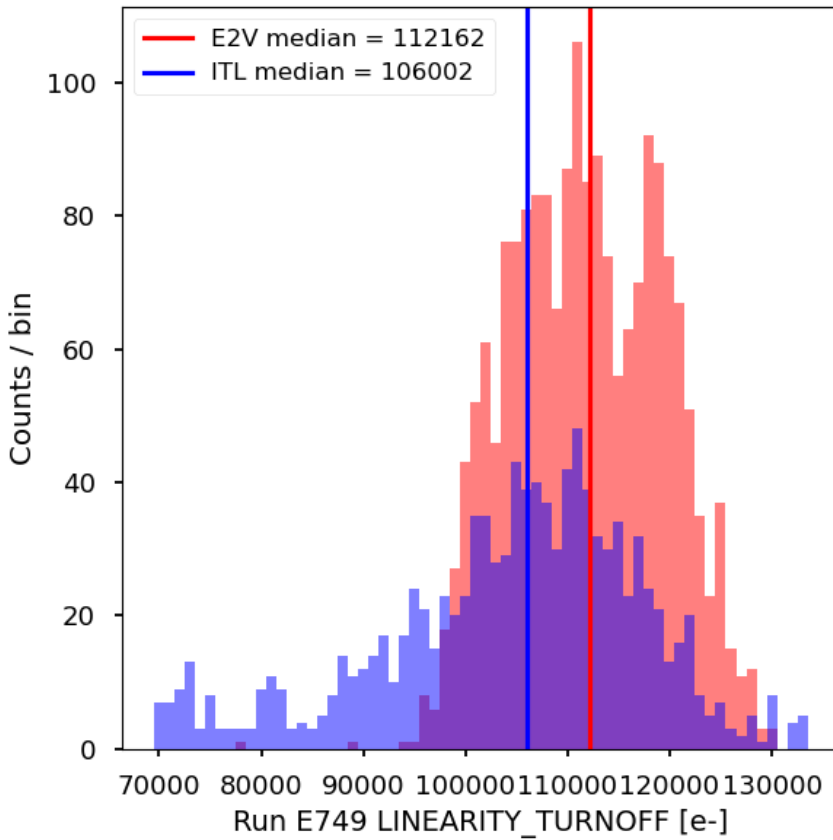
Run 7 PTC turnoff measurements agree closely between run 6 and run 7, differing by 200 e- for both ITL and E2V sensors. Notably, they are lower on average for both detector types.
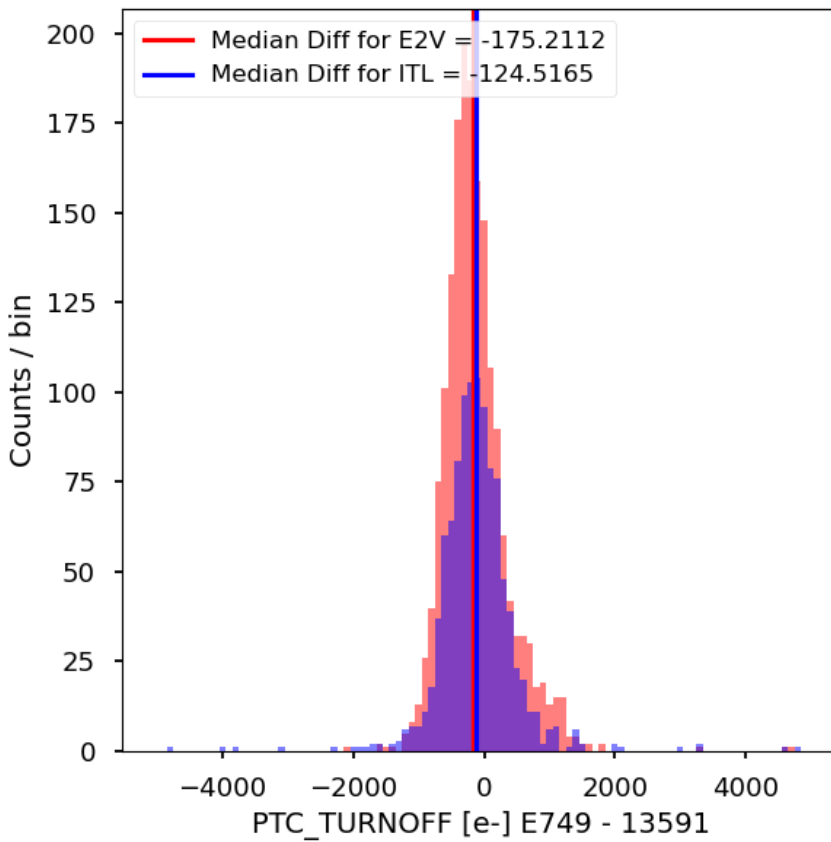
2.4.2 PTC Gain

PTC gain is the conversion factor between digital output signal and the the number of electrons generated in the pixels of the CCD. It is one of the key parameters derived from the Photon Transfer Curve, as it is the slope above the flux range at which the variance is dominated by shot noise, and below the PTC turnoff. Gain is expressed in e/ADU, and scales the digitized analog signals from the ASPICs to units of e[1].
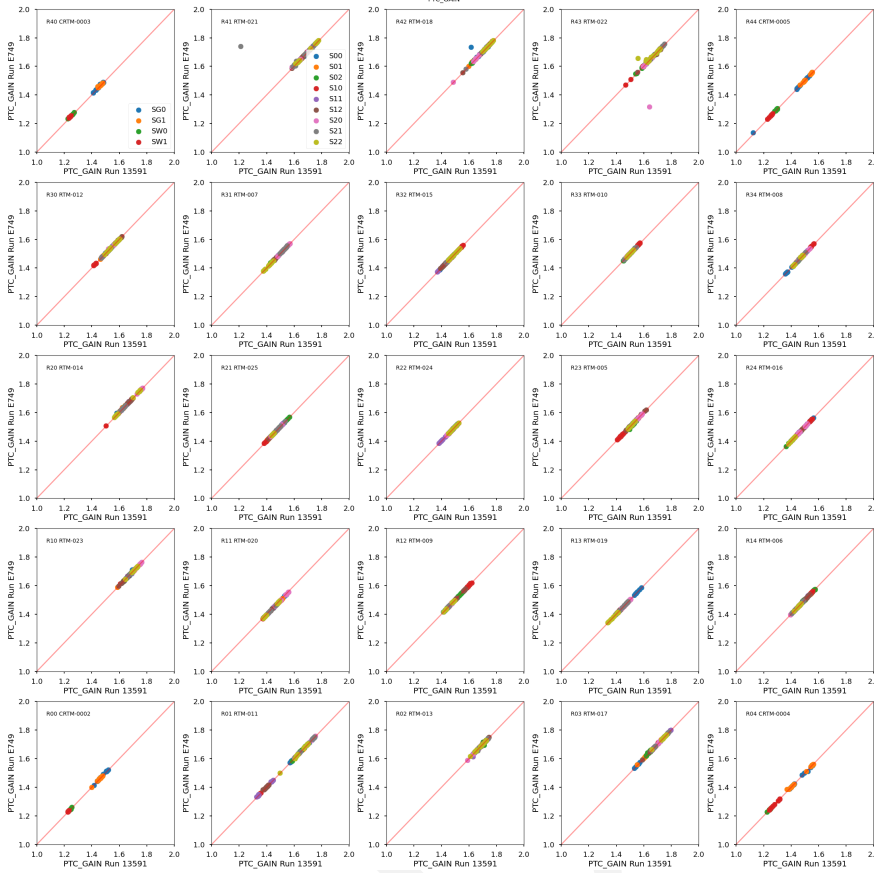
PTC gain measurements agree extremely closely across all sensors in the focal plane.

2.4.3 Brighter fatter a00 coefficient

This redistribution causes the charge to "spill" into adjacent pixels, effectively broadening the point spread function (PSF). The brighter-fatter effect is the most dominant source of covariance in the PTC curve. The brighter-fatter effect in CCDs refers to the phenomenon where brighter pixels appear larger (or "fatter" than dimmer ones). This occurs due to electrostatic interactions within the pixel wells of the CCDs, when a pixel accumulates a high charge from incoming photons and creates an electric field that slightly repels incoming charge carriers into neighboring pixels. The brighter fatter effect can be modeled as the most dominant source of pixel-pixel correlations. Following the PTC model from Astier et al. (2019), $_{00}$ describes the change of a pixel area due to its own charge content, or the relative strength of the brighter-fatter effect. Since same-charge carriers repel each other, the pixel area decreases as charge accumulates inside the pixel well, which implies $_{00} < 0$. In eo_pipe, an absolute value is taken of the $_{00}$ parameter, so the tabulated quantities are positive.
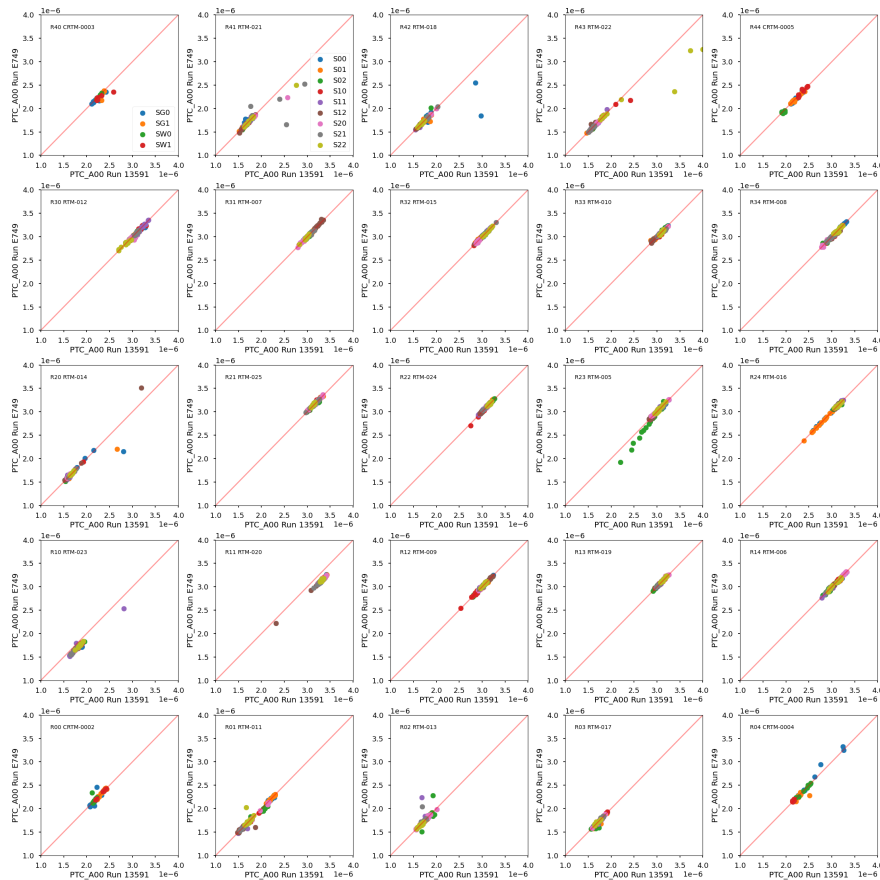
The strength of the brighter-fatter effect is generally comparable between Run 6 and Run 7. A few outliers exist across the focal plane, of both CCD types.
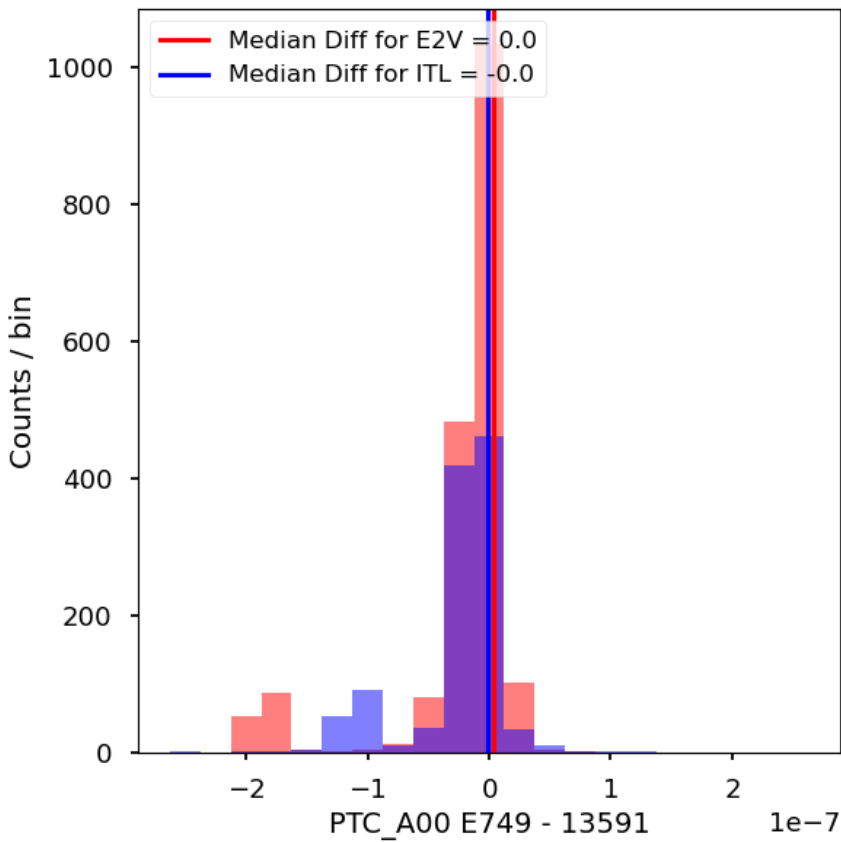
However, the differences in the brighter-fatter $_{00}$ coefficient between Run 6 and Run 7 show that the magnitude of $_{00}$ decreased for most of the outliers, which implies an improvement in imaging for those pixels.

2.4.4 Brighter-Fatter Correlation

The strength of the brighter fatter covariance correlation, and its subsequent error, provides a direct comparison of the PTC covariances across different runs.
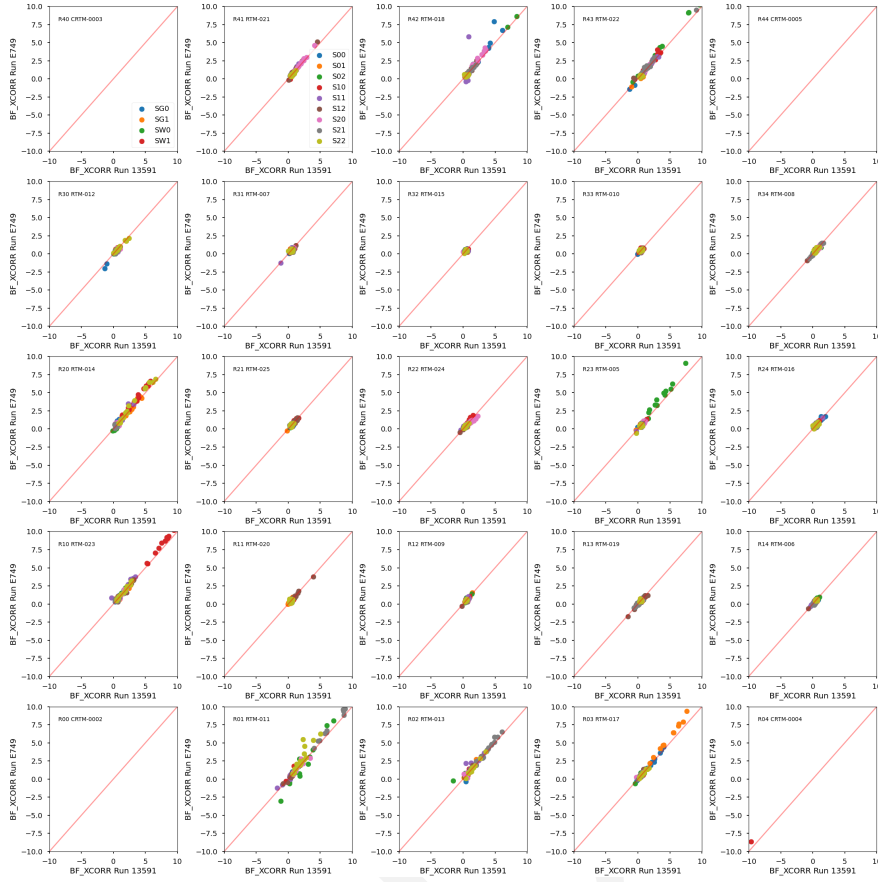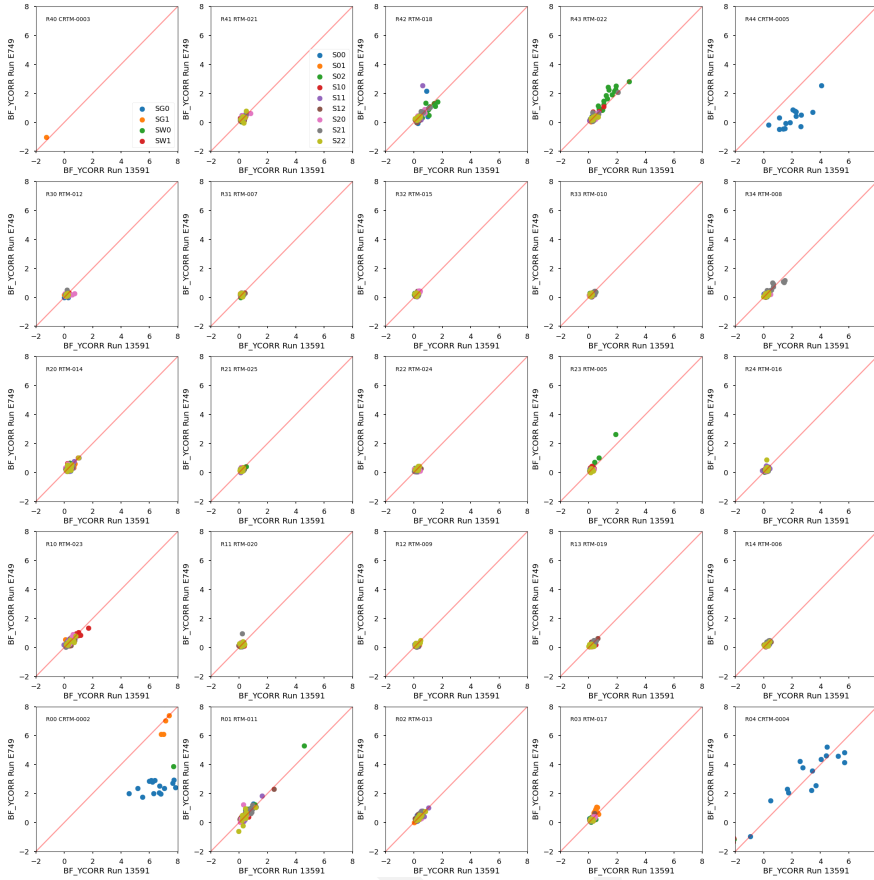
The brighter-fatter correlation is comparable across different runs, regardless of detector type. The strongest deviation comes from a lower Run 7 x-correlation, with a difference of ~0.07, which is negligible.
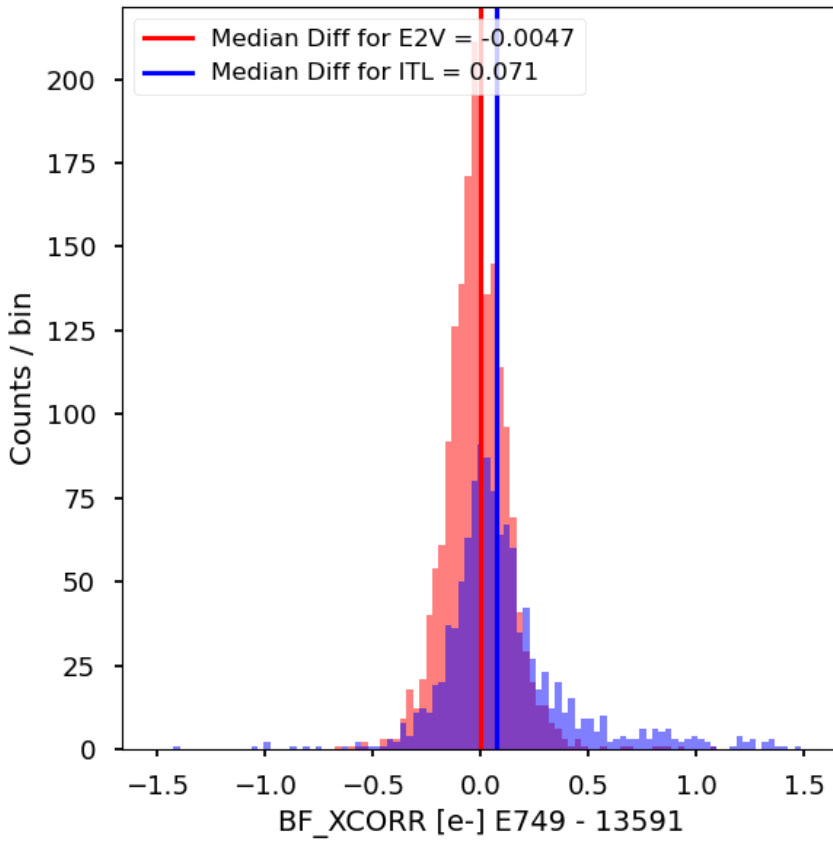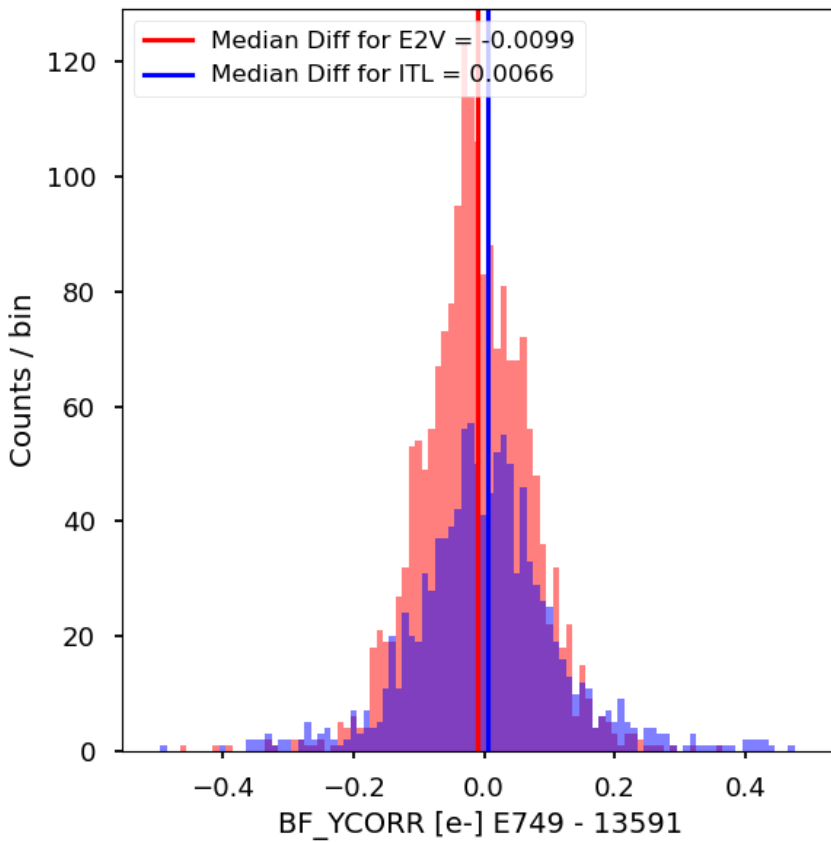
2.4.5 Row-means variance

Row-means variance is a metric that measures the row-to-row variance in flat frames. By computing the ratio of the row variance (or measured variance) to the expected Poisson signal (or expected variance) at the flux level, we can measure if additional noise enters the PTC curve at any point.
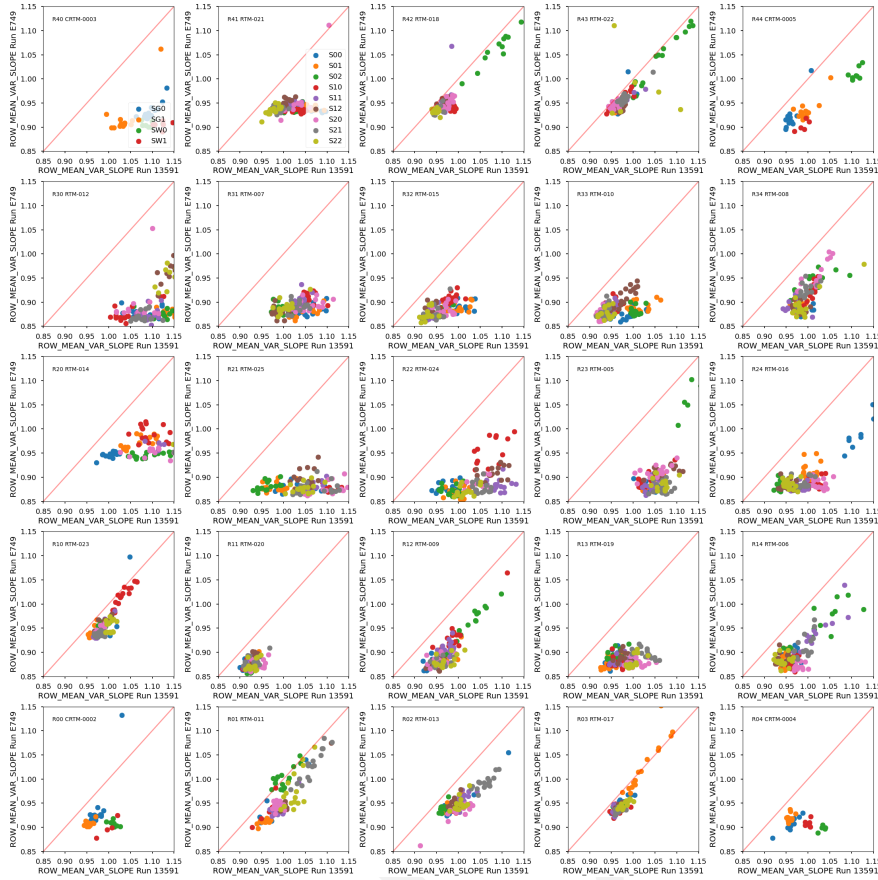
Differences in row-means variance between runs are evident, and are distinctly different for different detector types. The difference between runs is more significant for ITL sensors, ~9% smaller on average in Run 7. For E2V sensors, the effect is ~3% smaller in Run 7. This indicates that the non-shot noise contributions to sensor noise are smaller in run 7 compared to run 6, a positive result for the camera.
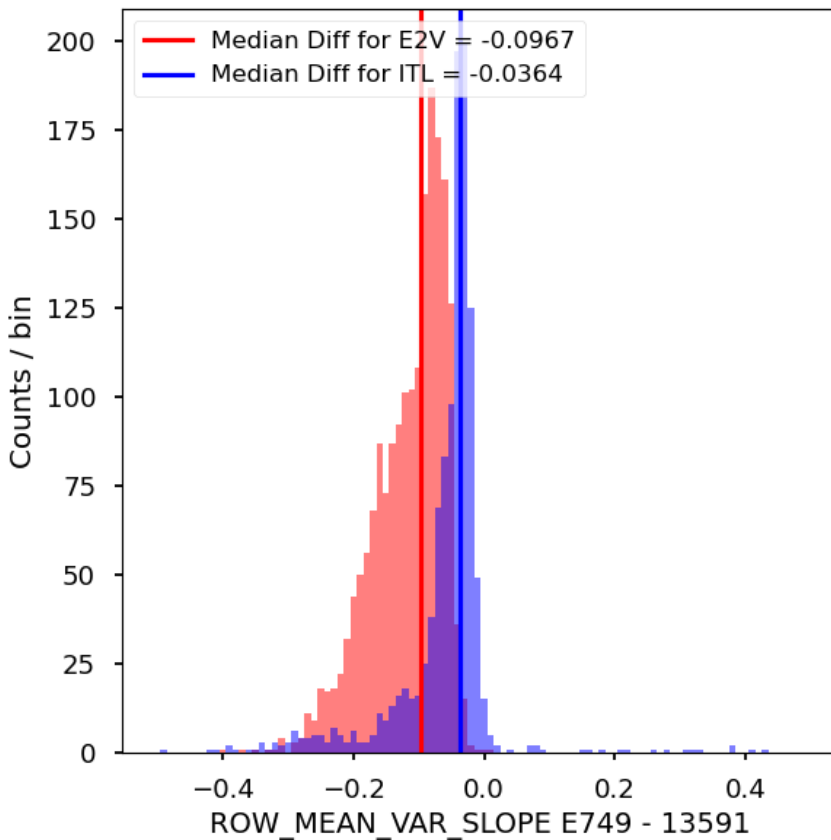
2.4.6 Divisadero Tearing

Divisadero tearing is manifested as signal variations near amplifier boundaries, connected features that are often jagged. These variations are on the order of ~1% relative to the flat field signal. To quantify divisadero tearing in a given column, we measure the column signal, and compare it to the mean column signal from flat fields.
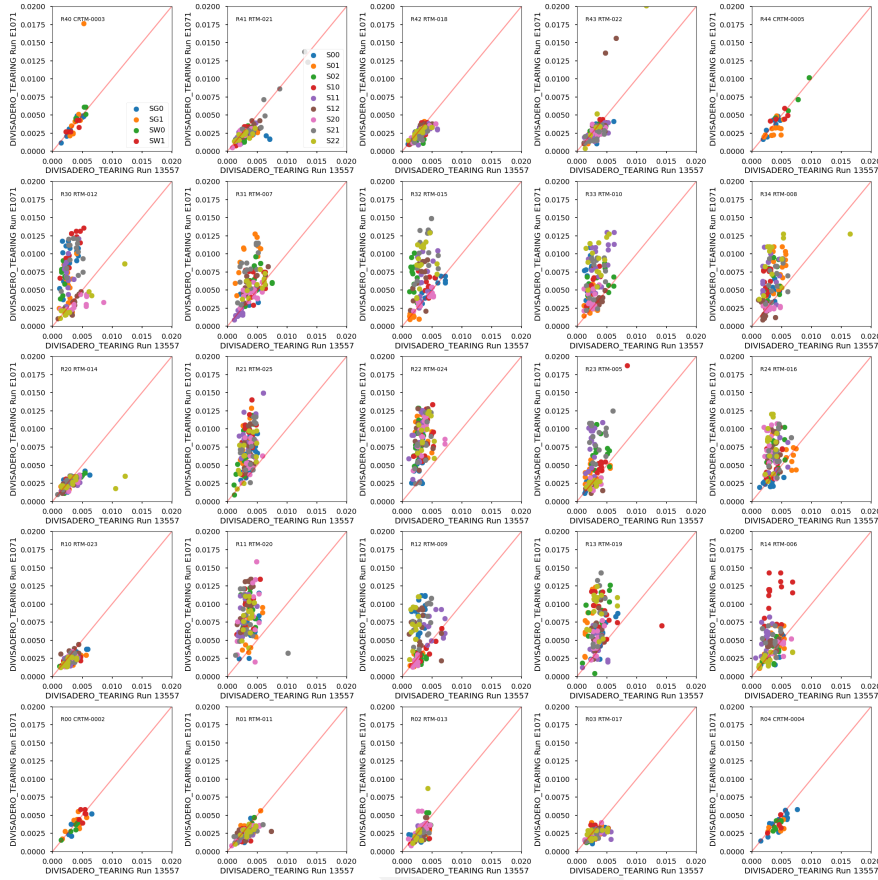
Divisadero tearing in e2v CCDs is greater in Run 7 than in Run 6. The tearing signal in ITL sensors is very consistent between Run 7 and Run 6, and much weaker than for e2v (Fig. 15.
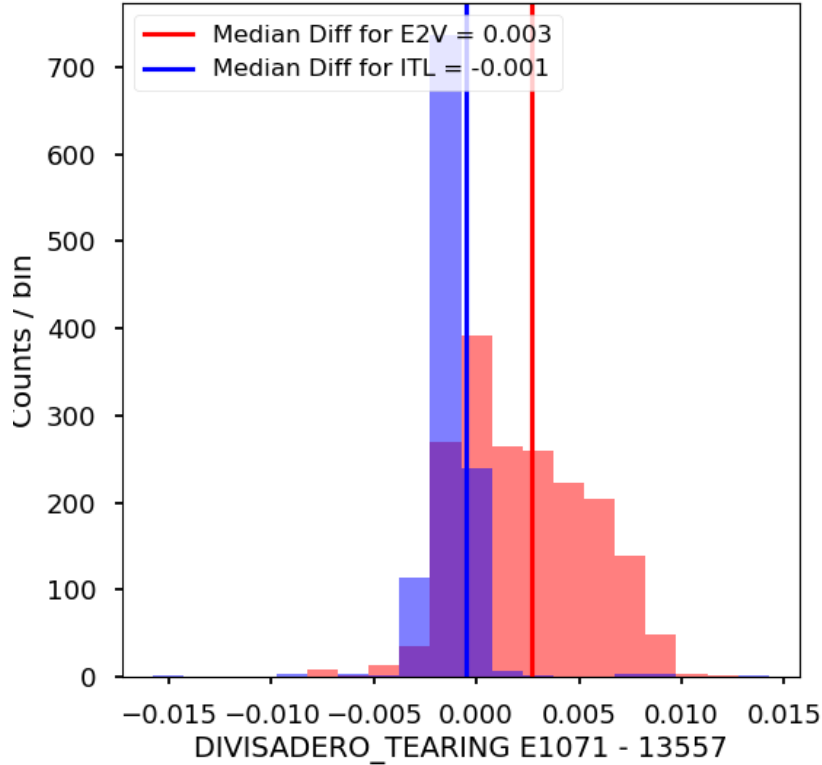
Figure 15: Distribution of difference between divisadero tearing in Run 7 (E1071) and Run 6 (13557), grouped by CCD type.

In Run 7 the median divisadero tearing amplitude for e2v CCDs is ~0.3% greater. In ITL sensors, maximum divisadero tearing is ~0.1% greater in Run 6.

2.4.7 Dark defects

Dark defects are localized regions or individual pixels that produce abnormally low signal levels, even in the presence of light. Similar to bright pixels, dark pixels are also quantified in dark columns over 50 pixel contiguous regions. These defects are caused by imperfections in the semiconductor material, imperfections during the manufacturing process of a CCD. For our evaluation, we extract dark pixels from combined flats, with the threshold for a dark defect defined as a 20% deficit from the average flux measured in the image segment.
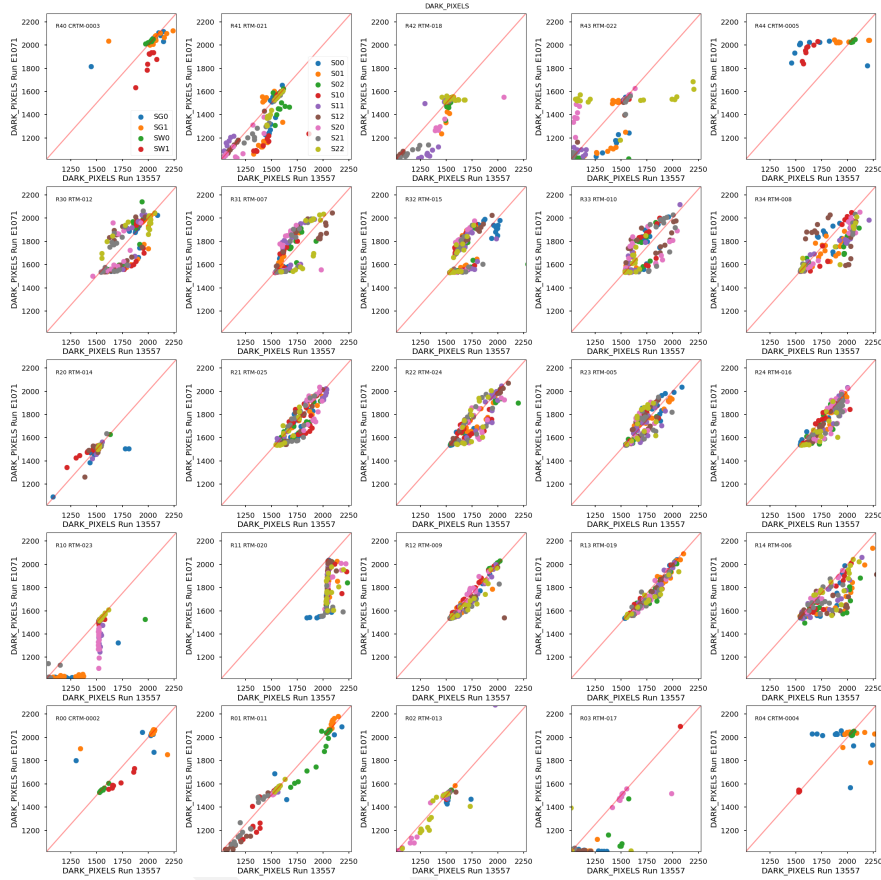
Figure 16: Comparison of dark pixel counts in Run 7 (E1071) and Run 6 (13557), with separate plots for each raft. Within each plot the color coding for all amplifier segments in a given CCD is the same.

Dark pixel counts measured in both Run 6 and Run 7 average ~1800 per amplifier (i.e., approximately 1M pixels), regardless of manufacturer. The high dark pixel counts are due to the 'picture-frame response' (also called 'edge roll-off') near the edges of the amplifier segments. The correlation between Run 7 and Run 6 dark pixel counts by CCD (Fig. 16) is generally good, with some notable exceptions...
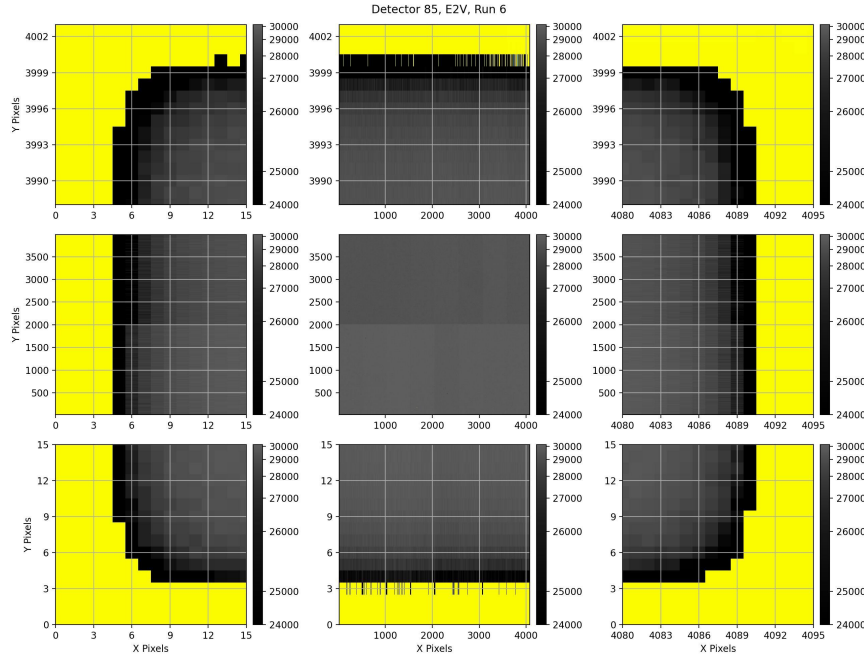
Figure 17: Illustration of masked border pixels (yellow) for detector 85 (R21_S11). [Needs more explanation.]

The eo-pipe configuration for evaluating dark defects considers a border pixel region that is masked differently from the dark pixels. The default size for this edge is zero pixels. Due to the inclusion of the picture-frame response in the counts, it is difficult to extract useful information about the dark defects in the focal plane. The default configuration has no border masking. The largest region allowed for the picture frame region is 9 pixels, determined by LCA-19363. Due to incompatibility of Run 6 data with the current pipelines, a direct comparison of a 9 pixel mask using Run 6 data is not currently available. However, a 9 pixel mask can be applied to the Run 7 data. Here is a reference to Figure 17, which needs some explanation here about how it relates to this paragraph.

Add conclusion when pipelines on E1071 are complete

2.5 Persistence

Persistence is a feature of CCDs and how they are operated involving charge trapped in the surface layer after high-flux exposures Banovetz et al. (DMTN-276). Persistence is described in detail in Section 3.1. Here we consider the measurements taken as part of a persistence measurement task in the typical B protocol. For measuring persistence, a high-flux acquisition is taken, followed by a sequence of dark images. The persistence signal has been observed to decrease in subsequent dark images as the trapped charge is released (see Fig. 18 for an example). As a metric for persistence, we evaluate the difference between the residual ADU in the first dark image and the average of the

residual ADU in the final dark images. This residual signal is found to be ~10 ADU.
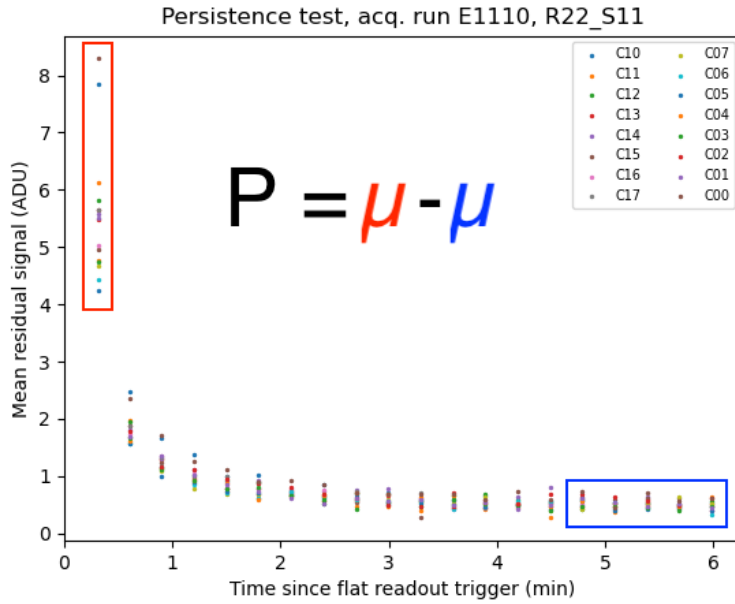
Figure 18: Persistence signal observed in R22_S11 in Run 7 (E1110) as a function of time after the high-flux flat image. The color coding indicates the individual amplifier segments. The persistence metric is defined as the residual signal in the first dark image after the flat acquisition (red box). Note that over time the signal does not decay entirely to zero.

In the initial Run 7 measurements, we had not changed any operating parameters of LSSTCam, so we would expect persistence to still be present images at the same level as in Run 6.
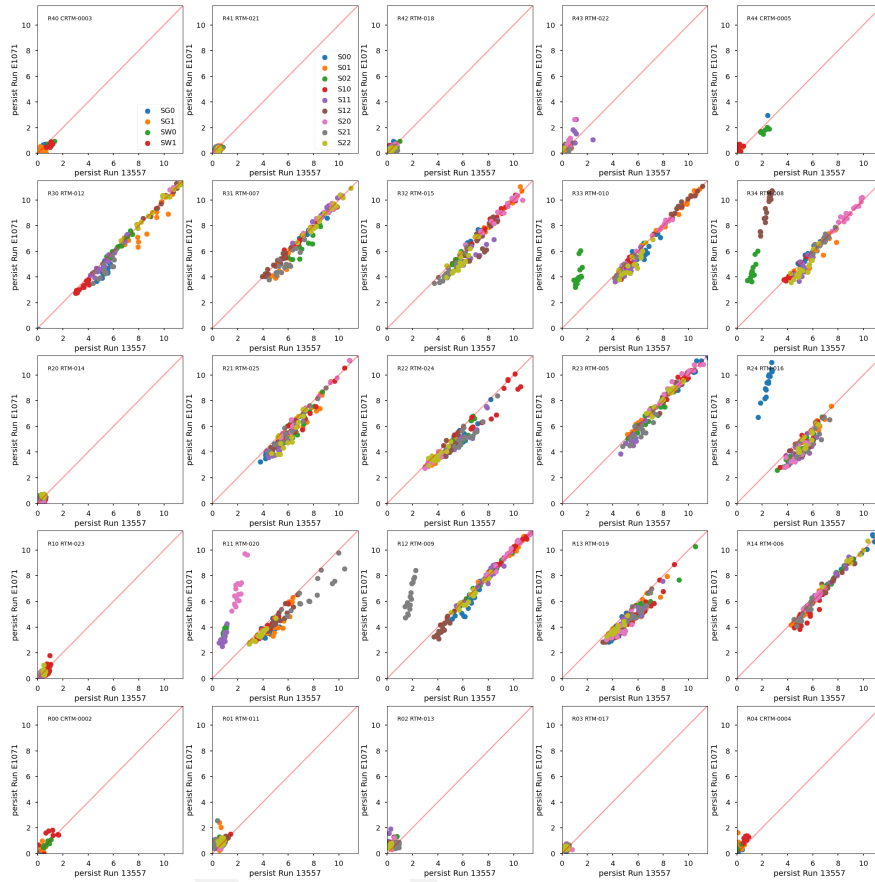
Figure 19: Comparison of persistence metric between Run 7 (E1071) and Run 6 (13357), organized by raft. The color coding indicates individual CCDs. Several e2v CCDs have markedly greater persistence in Run 7.

The persistence signal is generally consistent in e2v sensors between Run 6 and Run 7. Several e2v CCDs have greater persistence metric value in Run 7 (Fig. 19). The outliers in these measurements are due to higher initial persistence signal measurements, resulting in an excess of ~5 ADU when comparing Run 6 with Run 7 (see Fig. 20).
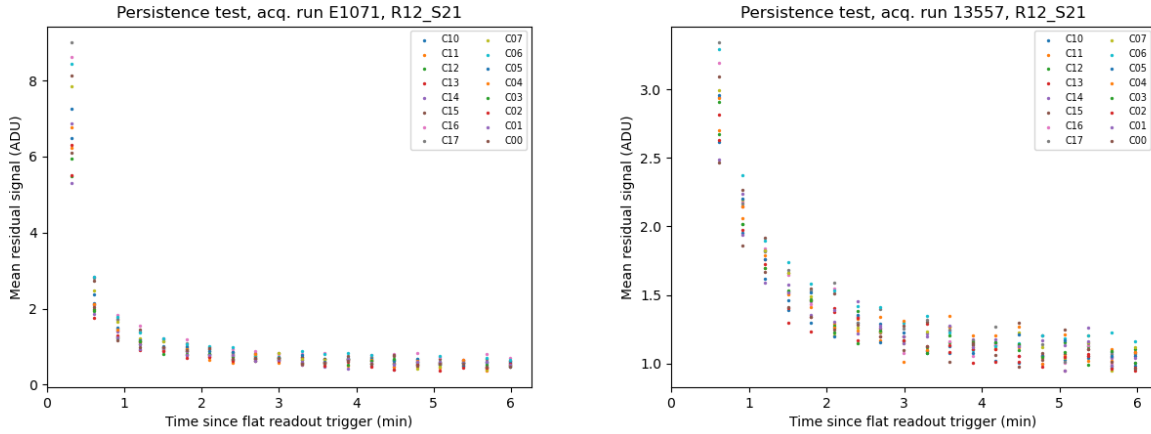
Figure 20: Comparison of persistence profiles for R12_S21 between (left) Run 7 (E1071) and (right) Run 6 (13557). The decay time constants are similar but the initial persistence level is greater in Run 7. The asymptotic levels are also different.

2.6 Differences between Run 6 and Run 7

Parameter [unit]	E2V		ITL	
	Run 6	Run 7	Run 6	Run 7
Serial CTI [%]	3.6816E-7	1.1357E-7	1.5922E-6	1.6478E-6
Parallel CTI [%]	1.2162E-7	1.0554E-7	1.6931E-8	-4.7849E-8
Dark current [e-/pix/s]				
Bright defects [count]				
Linearity turnoff [e-]	112410.98	112162.66	105960.37	106002.95
PTC turnoff [e-]	90422.94	89697.03	78209.44	77913.08
PTC Gain [e- / ADU]	1.4785	1.4811	1.6717	1.6760
PTC $_{00}$ [$\frac{1}{2}$]	3.0854E-6	3.0863E-6	1.7119E-6	1.7031E-6
BF x-correlation	0.5236	0.5169	0.7155	0.7521
BF y-correlation	0.1785	0.1707	0.2859	0.2869
Row-means variance	0.9927	0.8836	0.9924	0.9466
Dark defects [count]				
Divisadero tearing maximum [%]				
Persistence [ADU]				

3 Camera Optimization

3.1 Persistence optimization

Leftover signal ("persistence") in the first dark image acquired after intense illumination has been observed. Persistence has been observed in an early prototype e2v sensor as early as 2014 [D2014]. It was confirmed that the amplitude of the persistence decreased as the parallel swing voltage was

decreased. This is consistent with the effect being a residual surface image [J2001], i.e., the excess charges are being held at the surface layer. The level of persistence is about 10–20 ADU, and the decay time constant is about 30 s [dmtn-276].

During the EO testing in 2021, we also found the persistence made a streak toward the readout direction from the place where a bright spot illumination occurred in a previous image. We call this "trailing persistence".

As noted in Section (ref. tearing section above), depending on operating conditions e2v sensors have another major non-ideality, so-called "tearing", which is considered a consequence of the non-uniform distribution of holes. Over the past few years, our primary focus in the optimization of the operating parameters was mitigation of the tearing, and we successfully eliminated the tearing by changing the e2v voltages from unipolar (both parallel rails high and low are positive) to bipolar (the parallel high is positive, and the low is negative) following the formula [Bipolar]. However, the persistence issue remained unchanged.

For the persistence issue, if this is a residual surface image, two approaches could be taken as discussed in [U2024]: either 1) establishing the pinning condition where the holes make a thin layer at the front surface so that the excess charges recombine with the holes, or 2) narrowing the parallel swing so that the accumulated charges in the silicon do not get close to the surface state.

The pinning condition could be established by decreasing the parallel low voltage to as low as -7 V or lower. The transition voltage needs to be empirically determined. However, Teledyne e2v advised that the measured current flow increases as the parallel low voltage is decreased, which increases the risk of damaging the sensor by inducing a breakdown[1]. Also, the excess charges could be recombined by the thin layer of the holes, which could affect linearity at high flux levels when charges start to interact with the holes.

The parallel swing determines the full-well. Depending on whether the accumulated charges spread over the columns or interact with the surface layer, there are blooming full-well regimes and the surface full-well regime. A full-well level between these two regimes is considered to be optimal [J2001], with no persistence and dynamic range as great as possible. Because we observe the persistence effect, we likely operate the sensor in the surface full-well condition and we need to decrease the parallel swing to get the blooming full-well or the optimal full-well. The obvious downside decreasing the full-well capacity.

The sensor control voltages are defined relative to each other. Changing, e.g., the parallel swing

---

[1]We note that ITL operates at a parallel low voltage of 8.0 V. We have observed the increased current flow. But we have software protection so that the current does not increase too much.

also requires changes to all other voltages to operate the sensor properly, e.g., to properly reset the amplifier. The initial voltages were given in the original formula [Bipolar] but to decrease the parallel swing we had to switch to the new formula in order to satisfy the constraints [PersistenceMitigationVoltage].

[S2024], set up a single sensor test-stand at UC Davis. They attempted multiple different approaches mentioned above and reported the results [DavisReport]. The summary is as follows:

- The new voltages following the rule work fine.
- Narrowing the parallel swing eliminates the persistence.
- Lowering the parallel low voltage did not work as we expected; going to a more negative voltage is probably needed.

Note that the e2v sensor in the UCD setup did not exhibit persistence. This might be due to the characteristics of the sensor, or perhaps the differences in the electronics (e.g., the long cable between CCD and REB). They need to move the parallel rails up.

3.1.1 Persistence optimization

Based on this test result, we decided to test the new voltages with the narrower parallel swing on the LSSTCam focal plane. Keeping the parallel low voltage at -6 V in order to operate the sensor safely (very conservative limit), we changed the parallel swing voltage from 9.3 V to 8.0 V as well as all the other voltages using the new formula. We overexposed the CCDs and took 20 darks afterward. Figure 21 compares the mean and median of pixel-by-pixel differences between the first and the last dark exposures, as a function of the parallel swing. As the parallel swing is decreased, the residual signal decreases, reaching roughly 10» less than the original level at 9.3 V. Although we sampled midpoints between 8.0 and 9.3 V, 8.0 V appears to work the best and could be lower with the penalty of decreasing the full-well capacity.

Figure 22 displays how the persistence is reduced by the parallel swing decrease. The images were processed with the standard instrumental signature removal and assembled in the full focal-plane view. The dark exposure was taken right after a 400 ke-equivalent flat exposure. The figure shows the distinct pattern of elevated signal associated with the e2v sensors, which fill the inner part of the focal plane.

The right-hand figure shows the same dark exposure but taken with the narrow parallel swing voltage of 8.0 V. The distinct pattern goes away. This demonstrates the persistence in e2v sensors becomes the (low) level of the ITL sensors.
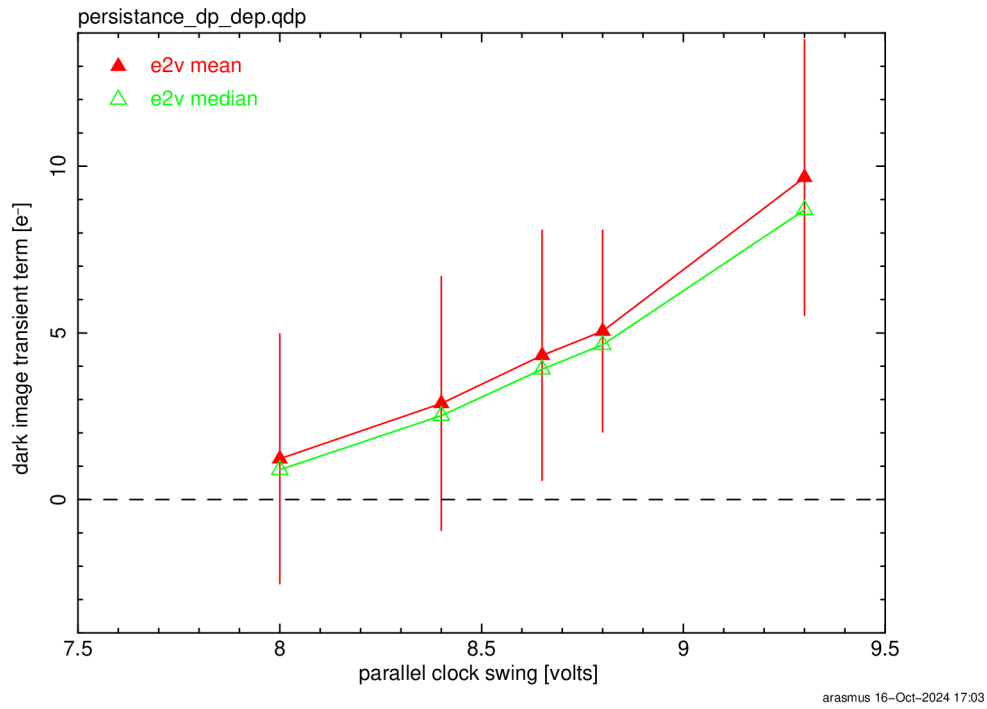
Figure 21: The remaining charges measured in every amplifier but aggregated by mean and median as a function of the parallel clock swing are shown.
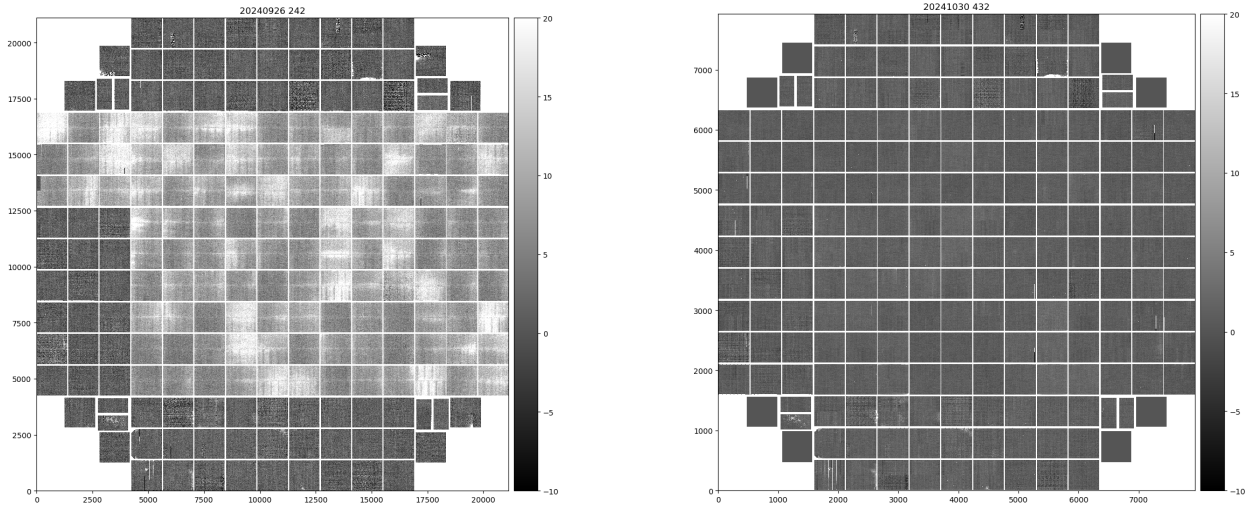
Figure 22: Comparison of dark exposures under different parallel swings. (left) The first dark exposure after a 400 ke flat image under the parallel swing of 9.3 V (Run E1110); (right) The first dark exposure after a 400 ke flat image under the parallel swing of 8.0 V (Run E1880). The figure shows no distinct patterns from persistence in e2v sensors. Note that the guide sensors were not displayed here because they were being operated in guider mode. Also some of the residuals in ITL caused by defects disappeared here because of the employment of the new sequencer file (v30).

3.1.2 Impact on full-well

Reduction of the full well is expected from narrowing the parallel swing voltage. This subsection explores how much reduction in the PTC turnoff is observed in the dense PTC runs. Two runs were acquired with identical setting except for the CCD operating voltage (E1113 for 9.3 V and E1335 for 8.0 V). As the PTC turnoff is defined in ADU, it needs to be multiplied by PTC_GAIN to compare the turnoff values in electrons. Figure 23 compares the PTC turnoffs in electrons and also shows their fractional difference. The median reduction was 22%.

3.1.3 Impact on brighter-fatter effect

Reducing the parallel swing is expected to enhance the brighter-fatter effect (BFE), possibly in an anisotropic way. The BFE can be characterized via the evolution of the variance and covariances of flat field exposures as a function of flux, i.e., via a PTC analysis. To evaluate the impact of reducing the parallel voltage swing on e2v sensors, we acquired two series of flat field exposures with the respective voltage setups and extracted the "area" coefficients (Equation (1) in [A2023]). The area coefficients describe by how much a unit charge stored in a pixel will alter the area of some other pixel (or itself). We find that reducing the parallel swing from 9.3 V to 8.0 V typically increases the area coefficients by 10% (between 5 and 19% depending on distance), and the increase is almost isotropic (i.e., very similar along serial and parallel directions; see Fig. 24). From these measurements, we anticipate that the increase of star sizes with flux in LSST data will not become
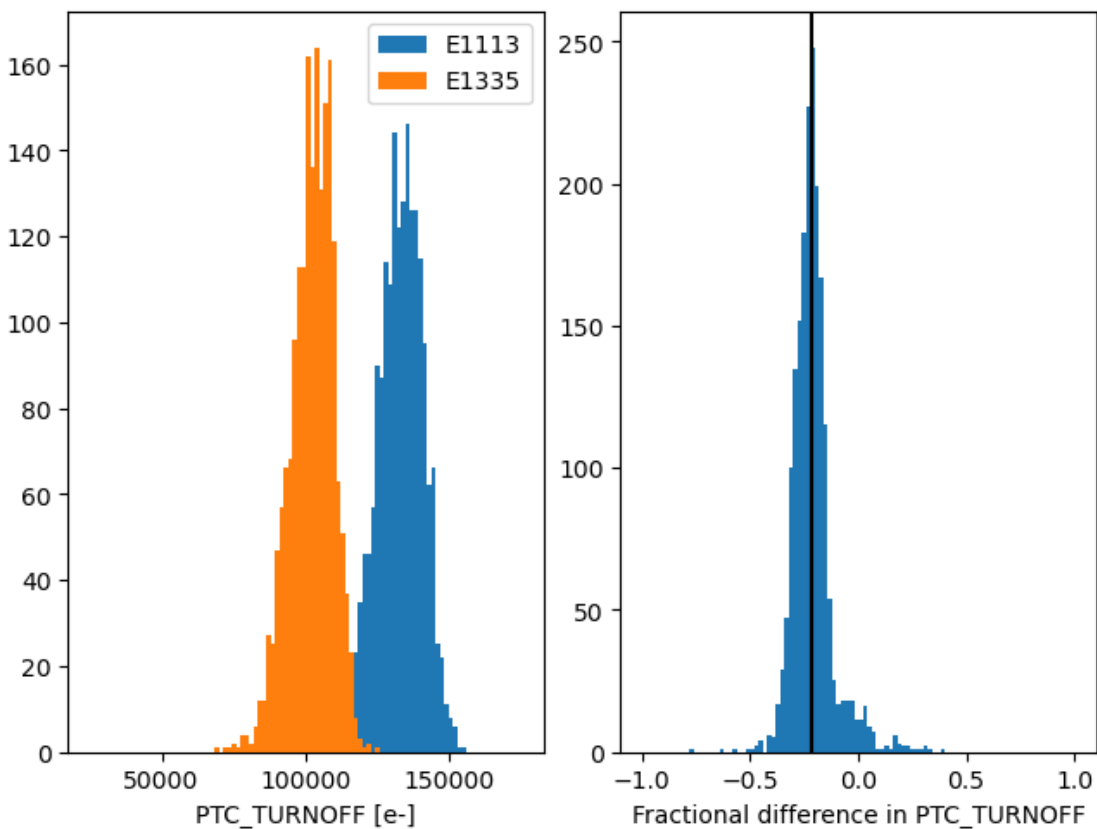
Figure 23: Histograms of the PTC turnoff values scaled to electron units (left) and the ratios of differences (right) between E1113 (9.3 V) vs E1335 (8.0 V). The median of the reduction is 22%.

more isotropic at $8.0\,\mathrm{V}$ than it was at $9.3\,\mathrm{V}$, and hence this reduction of parallel swing does not risk increasing systematic uncertainty of the PSF ellipticity.
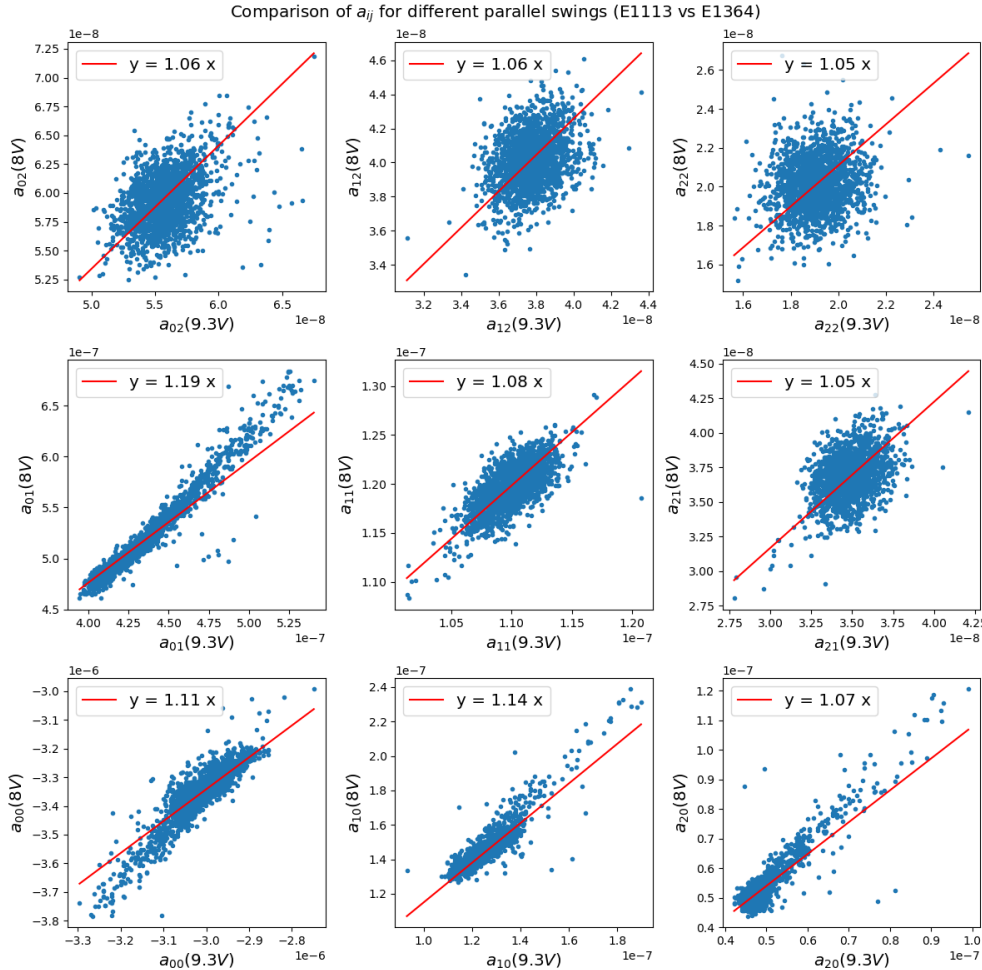
Figure 24: Scatter plots of area coefficients (one entry per amplifier) measured at $8.0\,\mathrm{V}$ and $9.3\,\mathrm{V}$. The sub-figures correspond to separations in rows () and columns () between the source of the area distortion and its victim, with the self interaction coefficient $_{00}$ at the bottom left. The first neighbors increase respectively by 19% in the parallel direction by 14% in the serial direction. So the BFE is slightly larger at $8.0\,\mathrm{V}$ but not significantly more anisotropic.

3.2 Sequencer Optimization

Several efforts were undertaken to optimize the sequencer configurations during Run 7. The following points summarize the key investigations:

- Clears: Here we summarize the discussion provided in Improvement of Clear CCD:

    - **No Pocket** We introduced the v29_Nop (No Pocket) sequencer, which is an improved

clear method using a serial register configuration that reduces the formation of pockets at the Image/Serial register interface. This clear method showed an approximately 2» improvement in the saturated image clear for e2v devices and completely resolved the issue for ITL devices, except for R01_S11, where the No Pocket method performs approximately 2» worse than the default clear. For an unknown reason, this ITL CCD retains a significant amount of uncleared charges (hundreds of lines) after a saturated flat. This issue prevents the use of the No Pocket configuration with ITL devices.

– **No Pocket with Serial Flush** We introduced V29NopSf (No Pocket with Serial Flush), an enhanced version of the No Pocket Clear sequencer, which includes a variable configuration of the serial register during the clear process (mimicking a serial flush), to further prevent the formation of pockets. This solution has been shown to completely prevent the presence of leftover charges after clearing a saturated image for e2v devices.

- Phase overlap during parallel transfer for e2v: e2v sensors feature four parallel phases. To improve the uniformity of the full well across a sensor, overlapping two phases during each time slice of the parallel transfer was introduced. However, this overlap is known to cause trailing persistence, as reported in DavisReport   . We conducted several runs using both intermediate overlapping and non-overlapping sequencers. By optimizing the operating voltages to avoid charge trapping, the trailing persistence is no longer a concern.

3.3 Improved Clear

3.3.1 Overview

In this section, we describe the work done during Run 7 to improve the image clear prior to collecting a new exposure.

The problem we wanted to address is the presence of residual charges in the first lines read for an image taken just after the clear of a saturated image. These "hard to clear" charges are associated with highly saturated flats or columns (or stars as observed in AuxTel or ComCam), which leave signal in the first lines of the subsequent exposure. The effect has a sensor-specific signature:

- In all ITL CCDs (except in R01_S10 for which the effect is much more significant and which will be addressed later in this section):

  The first CCD line of an exposure read after an image with saturated overscan is close to saturation and in most of cases a small leftover signal is also present in the second line.

- In e2v CCDs:

Although the effect is slightly amplifier dependent, as for ITL, the first line read after an exposure that follows an exposure with saturated overscan, is close to saturation, and a significant signal is visible in the subsequent 20–50 lines (see left-hand plot in Fig. 25).

These leftover electrons are not associated with what we usually call residual image or persistence. They are suspected to be associated with pockets, induced by the electric field configuration in the sensor and the field associated with saturated pixels: pocket(s) that survive to a clear, will prevent charges to be cleared. A change of the electric field (e.g., a change in the configuration of the clocks) can remove the pockets, and free the charges, allowing them to be cleared. If charges stuck in pocket(s) are not removed by a clear, we observed that an additional image read (e.g., a bias) will fully remove them: only the first exposure taken after an image with saturated overscan is impacted. If the clocks configuration used in our standard clear is not able to flush away those charges, a standard readout of $>\sim$ 2000 lines does remove them.

The localization of these uncleared electrons in the first lines of the CCDs, indicates that the interface between the image area and the serial register is the location of the pockets. For this reason we investigated changes in the field configuration of the serial register during the clear, to avoid pockets at the image-serial register interface.

3.3.2 New sequencers

To address this clear issue, we focussed on updating the serial register field as the lines are moved to it. The constraint being that the changes introduced should not significantly increase the clear execution time. It should be noted that in 2021 we tried a sequencer called "Deep Clear" [sequencerV23_DC] as a first attempt to address the clear issue: it added one full line flush on top of the existing one at the end of the clear. This sequencer did improve the clear, but did not fully fix the clear issue (see Table 3).

Table 3: *Clear methods used so far.*

Clear Type	Clear Duration (ms)	e2v after Saturated Flat	ITL after Saturated Flat	R01_S10 ITL "unique"
Default Clear 1 clear (seq. V29)	65.5	First row saturated signal up to row 50	1st row saturated signal up to 2nd row	First 500 rows saturated for 4 amp, 13 amp with signals
Multi Clear 3 clears (seq. V29)	196.5	No residual electrons	No residual electrons	First 150 rows saturated for 2 amp, 5 amp with signals

Multi Clear 5 clears (seq. V29)	327.4	No residual electrons	No residual electrons	First 100 rows saturated for 2 amp, 2 amp impacted
Deep Clear 1 clear (Seq. V23 DC)	64.69	1st row saturated signal up to row <20	Tiny signal left in the first row	not measured
No Pocket (Nop) 1 clear (seq. V29)	65.8	signal up to row 20	No residual electrons	First 1000 rows saturated for 16 amp, 16 amp with signals
No Pocket Serial Flush (NopSf) 1 clear (seq. V29, V30)	67.0	No residual electrons	No residual electrons	first 750 rows saturated for 16 amp, 16 amp with signals

In Run 7, we considered on top of the default clear, two new configurations. The changes are in the ParallelFlush function, which moves the charges from the image area to the serial register:

- The default clear (V29): In the default clear, all serial clock voltages are kept up as the parallel clocks move charges from the image area to the serial register ([sequencerV29]). The charges once on the serial register are expected to flow to the ground: the serial register clocks being all up, without pixel boundaries, and with its amplifier in clear state. At the end of the clear, a full flush of the serial register is done (~ the serial clocks changes to read a single line).

- The No-pocket Clear (Nop): a clear where the serial register has the same configuration (S1 & S2 up, S3 low) when the parallel clock P1 moves the charges to the serial register than in a standard image read. Still we kept all phases up for the rest of the time for a fast clear of the charges along the serial register ([sequencerV29_Nop]). The idea is that the S3 phase is not designed to be up when charges are transferred to the serial register, and is probably playing a major role in the creation of pockets.

- The No-Pocket with Serial Flush Clear (NopSf): this sequencer is close to the Nop solution, except that during the transfer of one line to the serial register, the serial phases are also manipulated to transfer two pixels along the serial register. The changes in electric field at the image-serial register interface are then even more representative of what a standard read produces, and should further prevent the creation of pockets. ([sequencerV29_NopSf]).
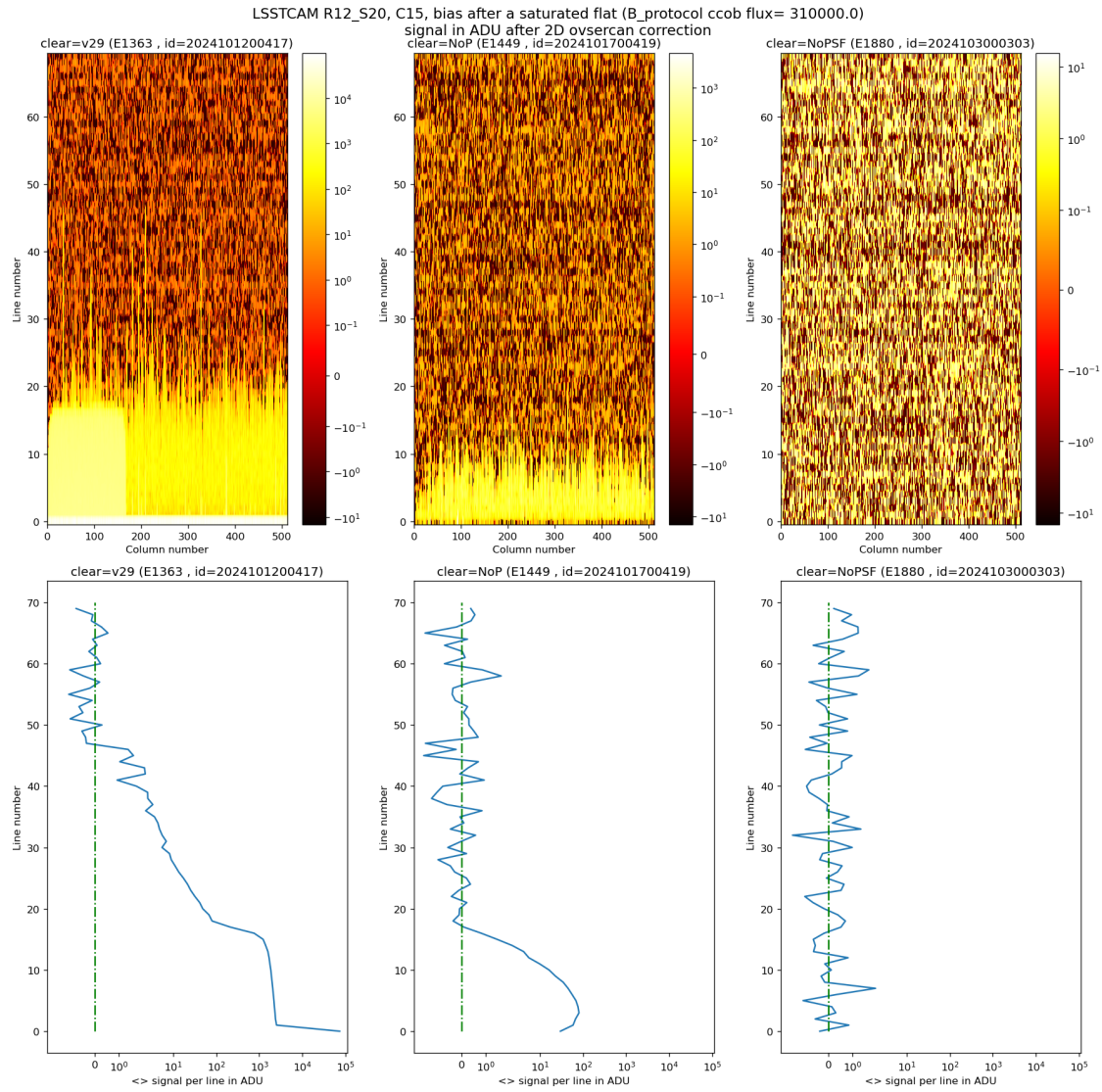
Figure 25: Impact of the various types of clear on a bias taken after a saturated flat for an e2v sensor (R12_S20).
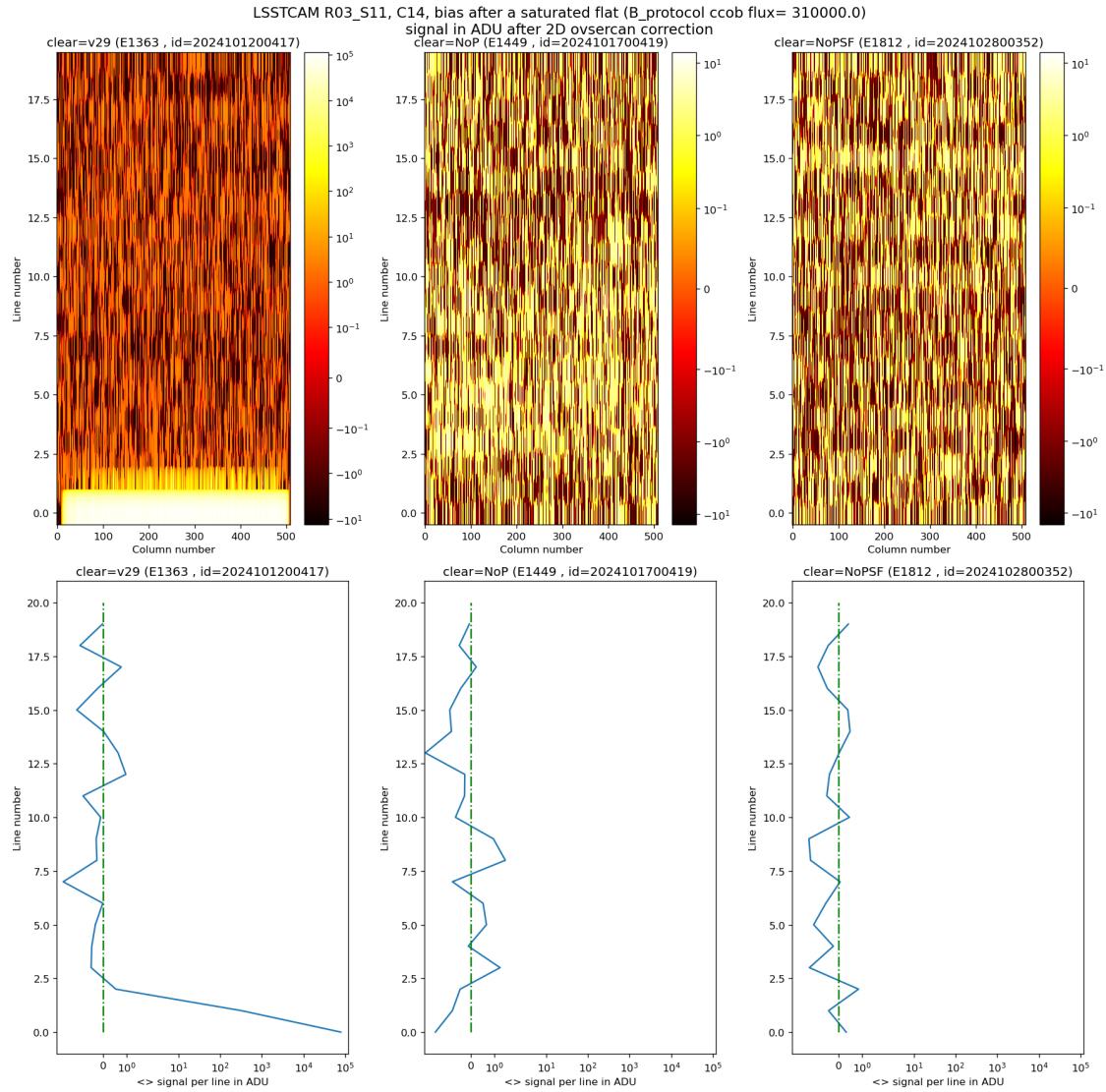
Figure 26: Impact of the various types of clear on a bias taken after a saturated flat for an ITL sensor (R03_S11).

3.3.3 Results on standard e2v and ITL CCDs

In Figures 26 and 25, we present for three types of sequencer (from left to right: V29, Nop, and NopSf), a zoom on the first lines of an ITL or e2v amplifier (for ITL R03_S11_C14 and for e2v R12_S20_C10 shown as a 2D lines-columns image (top plots) or as the mean signal per line for the first lines read of an amplifier (bottom plots).

As seen in the left-hand panel of Figure 25 for an e2v CCD, a bias taken just after a saturated flat will show a residual signal in the first lines read when using the default clear (left images, clear= V29): the first line has an almost saturated signal (~ 100 kADU here), and a significant signal is seen up to row ~50. In practice, depending on the amplifier, signal can be seen up to line 20–50. When using the Nop clear (central plots), we can already see a strong reduction of the uncleared charges in the first acquired bias after a saturated flat. Still a small residual signal is visible in the first ~20 lines. The NopSf clear (right plots) fully clears the saturated flat, and no uncleared charges are observed in the following bias.

As seen in the left-hand panel of Figure 26 for an ITL CCD, a bias taken just after a saturated flat will show a residual signal in the first rows read when using the default clear (left images, clear=v29): the first line has an almost saturated signal (~ 100 kADU here), and a significant signal is seen in the following line. Both Nop clear (central plots) and NopSf clear (right plots) fully clear the saturated flat, and no uncleared charges are observed in the following bias.

3.3.4 Results on ITL R01_S10
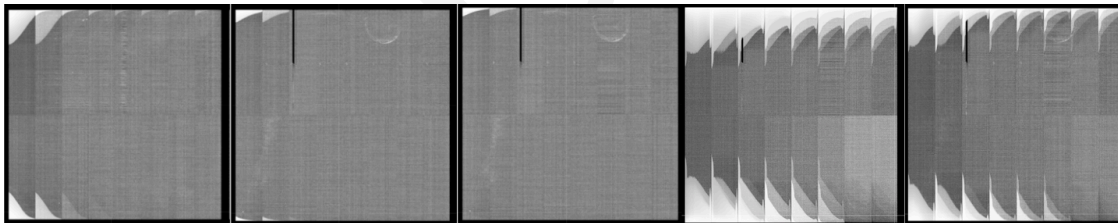
Figure 27: Impact of the various types of clear on ITL R01_S10 after a saturated flat (bias after a saturated flat), from left to right: 1 standard clear, 3 standard clears, 5 standard clears, 1 Nop clear, 1 NopSf clear.

One ITL sensor, R01_S10, presents a specific behavior that is not understood:

- It has a quite low full well (2/3 of nominal).
- The 3 CCDs of this REB (REB1) have a gain 20% lower than all other ITL CCDs.
- The images taken after a large saturation, as seen in Figure 27, show a large amount of uncleared charged (with the standard clear: 4 amplifiers retain ~500 rows of saturated signal!).

It appears that putting S3 low during the clear as done in Nop and NopSf, is even worse than

a standard clear. This is strange, as a full frame read, which does this too, manages to clear a saturated image. We can notice that NopSf is ~50% better than Nop, but still worse than the standard clear, in particular for the 12 amplifiers that are almost correct with the standard clear.

At this time we do not have a correct way to clear this sensor once it collects a saturated flat, but it is not known if a saturated star in this sensor, leaving signal in the parallel overscan, will present the same clear issue.

3.3.5 Conclusion

Even if Nop or NopSf overcome the clear issue we had with ITL sensors, the exception of R01_S10 prevented the usage of those sequencers for ITL devices for Run 7. Note that aside from R01_S10 the numbers of lines potentially "not cleared" in ITL devices after saturated images are small (2 first rows), and they correspond to a CCD area that is difficult to use anyway (sensor edges with low efficiency). So at this stage the default clear is still our default for ITL, and further studies to overcome the problem with R01_S10 are forseen (e.g., investigate using a continuous serial flush during exposure at low rate, 10^6 pixel flushes in 15 s).

> For the other CCD type, after the studies in Run 7, we now have a good way to fully clear the e2v devices through the NopSf clear. The NopSf clear grants that the first 50 rows of e2v CCDs that had un-cleared electrons from the previous exposure are now free of such contamination.

For the time being:

- For e2v, NopSf will be the default clear method.
- For ITL, the original clear (serial phase 3 always), slightly extended in time to match the NopSf e2v clear execution time, will stay the default method.

3.4 Toggling the RG Bit During Parallel Transfer

This investigation comes from an analogy drawn with the ITL sequencer file. Although the vendor recommended toggling the RG bit at the end of the parallel transfer, it was unclear whether this step was truly necessary. Given the improvements observed in ITL devices, applying this approach to e2v devices also became an area of interest.

3.5 Disable IDLE FLUSH

IDLE_FLUSH is one of the main settings in the sequencer file that enables the sequencer output to run while in the IDLE state (the period between one exposure and the next). The specific implementation of IDLE_FLUSH can be selected from various functions in the sequencer file. In Run 5, we chose the `ReadPixel` function, which reads out a pixel. This choice was initially made to mitigate the so-called yellow corner issue, a 2D structure of elevated signal near an amplifier corner

observed in bias and dark exposures for certain amplifiers on e2v CCDs (see details in [U2024]).

However, it was reported that running IDLE_FLUSH exacerbates the Divisidero tearing issue. Divisidero tearing appears as a signal deficiency at amplifier boundaries in e2v sensors, accompanied by increased signal in adjacent columns. Additionally, using `ReadPixel` as the IDLE_FLUSH function has the highest thermal impact because it continuously operates the Analog-to-Digital Converter at its maximum rate. This results in a significant difference in power consumption, more than 50 W over all rafts, between the exposure state and the IDLE state. Consequently, the focal plane experiences a temperature variation of approximately 2 deg C between periods of image acquisition and idle periods (Figure 28).

Figure 28: Impact of enabling and disabling IDLE_FLUSH on focal-plane temperature and power consumption.

This temperature variation in the focal plane can lead to changes in the REB temperature, potentially causing gain variations or instability in the bias. Based on these considerations, we decided to disable IDLE_FLUSH. The impact of this change on bias stability is discussed in Sections 4.7 and 4.8.

Figure 29 shows the impact on the Divisadero tearing. The runs shown here are selected B protocol runs with different settings in the time order. There were few changes: (1) switching to narrower parallel swing voltage, (2) changing the number of clears before the exposure, (3) disabling IDLE_FLUSH. Some minor changes in each changes are also included such as changing the number of clears, or changing the sequencer file (the change from v29 to v30 is primarily in-
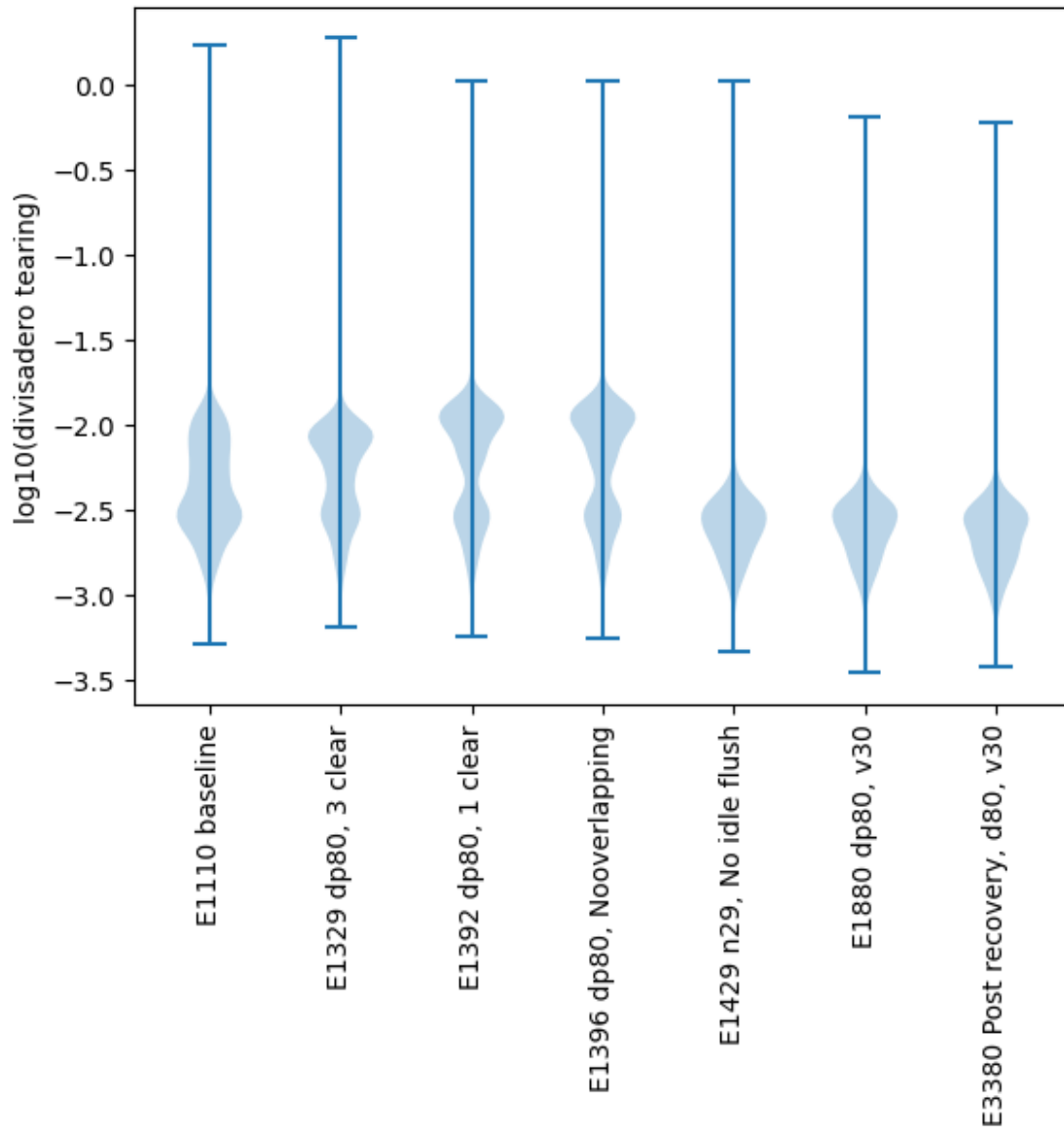
Figure 29: Impact of disabling IDLE_FLUSH on Divisadero tearing

corporation of the change in the clear). The figure includes both ITL and e2v results. The two distinct distributions in earlier runs correspond to the differences between the two types of CCD (the higher one is e2v and the lower one is ITL). The greatest change can be seen when we switched to not running IDLE_FLUSH at E1429, which brought the overall distribution down. The two distributions became indistinguishable, which indicates the majority of the Divisadero tearing for e2v is mitigated.

E3380 was the run taken after the recovery from the shutdown due to poor performance of the Pumped Coolant System. This fact confirms that the metric is consistent over power cycling of LSSTCam.

3.6 Summary

e2v sensors had persistence. We confirmed that narrowing the parallel swing voltage of the e2v CCD operation greatly reduced persistence. As penalties, we observed a full well reduction of 22% and a ~10% increase of the brighter-fatter effect, essentially in an isotropic way.

We developed v30 sequencer files that have guider functionality built in and an improved clear of No Pocket Serial Flush.

We also disabled IDLE_FLUSH to improve the thermal situation and the Divisadero tearing.

Sequencer files have undergone evolution for both ITL and e2v versions. The final sequencer file from Run 6 was the v26noRG version for ITL and the regular v26 for e2v. The suffix noRG indicates that the RG bit is not toggled during parallel transfer. This modification appears to enhance the stability of the bias structure for most ITL amplifiers.

During Run 7, several changes were implemented, as described below:

- v27 incorporated guider functionalities, including ParallelFlushG and ReadGFrame. However, the noRG change was inadvertently included. Consequently, we abandoned this version and switched to v28.
- v28 sequencer files merged v26noRG and v27. https://rubinobs.atlassian.net/browse/LSST CAM-5
- v29 introduced changes to speed up the guider. https://rubinobs.atlassian.net/browse/LS STCAM-34
- v30 primarily focused on e2v. We introduced a new approach to NopSf for e2v CCDs https://github.com/lsst-camera-dh/sequencer-files/pull/17. To align timing with the ITL version, a change was made. https://github.com/lsst-camera-dh/sequencer-files/pull/18

4 Characterization & Camera stability

4.1 Final characterization background

Run Type	Cerro Pachón Initial Run	Cerro Pachón Final Run
B Protocol	E1071	E
PTC	E749	E

Table 4: Reference runs for Run 6 and Run 7 comparisons

4.1.1 Stability flat metrics

4.1.1.1 Serial CTI

4.1.1.2 Parallel CTI

4.1.2 Dark metrics

4.1.2.1 Dark current

4.1.2.2 Bright defects

4.1.3 Flat pair metrics

4.1.3.1 Linearity and PTC turnoff

4.1.3.2 PTC Gain

4.1.3.3 Brighter fatter a00 coefficient

4.1.3.4 Brighter-Fatter Correlation

4.1.3.5 Row-means variance

4.1.3.6 Divisadero Tearing

4.1.3.7 Dark defects

4.1.4 Persistence

4.1.5 Differences between run 7 initial and run 7 final measurements

Parameter [unit]	E2V		ITL	
	Run 7 initial	Run 7 final	Run 7 initial	Run 7 final
Serial CTI [%]				
Parallel CTI [%]				
Dark current [e-/pix/s]				
Bright defects [count]				
Linearity turnoff [e-]				
PTC turnoff [e-]				
PTC Gain [e- / ADU]				
PTC $_{00}$ [$\frac{1}{2}$]				
BF x-correlation				
BF y-correlation				
Row-means variance				
Dark defects [count]				
Divisadero tearing maximum [%]				
Persistence [ADU]				

4.2 List of Non-Functional Amplifiers

We classify amplifier sections as non-functional if they produce effectively no signal (dead) for incident light, or if the read noise level is above 18 (hi-noise). Dead amplifiers are found with either read noise levels below 4 which indicates no signal is reaching the ADC, or gains below 0.8 or above 1.8.

A list of non-functional amplifiers was produced from both single raft testing as well as a selection of runs from the BOT data taking period. A summary of those amplifiers is shown in Table **?**. As the table indicates two amplifiers, R01_S01_C00 and R10_S00_C00 transitioned from dead to working during the course of the BOT testing. Furthermore another

Raft	Slot	Segment	(Amp)	Problem	Single Raft testing	Run 12433 9-Raft (Oct '19)	Run 1261(
R01	S01	00	(16)	Dead Channel	Dead	Dead	OK
R03	S11	00	(16)	Dead Channel	OK	NA	OK
R10	S00	00	(16)	Dead Channel	Dead	NA	OK
R30	S00	10	(1)	Dead Channel	Dead	Dead	Dead
R01	S02	07	(9)	Noise > 18e	OK	27e	22e
R01	S11	00	(16)	Noise > 18e	OK	24e	OK
R41	S11	14	(5)	Noise > 18e	OK	NA	36e
R41	S21	02	(14)	Noise > 18e	OK	NA	OK
R43	S02	03	(13)	Noise > 18e	18e	NA	18e
R43	S20	14	(5)	Noise > 18e	OK	NA	OK

4.3 Full well measurements

4.4 Non-linearity studies

PTC runs are meant primarily to measure variance and co-variance curves. We collect pairs of flat images, from an integrating sphere fed by various LEDs, that illuminates the focal plane. To cover the entire dynamic range of the CCDs, we vary the length of the LED flash, the number of flashes, and the current of the LED. These data sets can be used to measure nonlinearity by comparing the CCD response to the integrated signal measured from a photodiode installed on a port of the integrating sphere that feeds a picoammeter. To avoid any shortcomings from picoammeter nonlinearity, we only compare photodiode signals of the same amplitude (illumination intensity) but different durations. We do not assume that integrated charges measured at different LED currents (and hence different photodiode currents) are on the same scale, although this turns out to be essentially true, as discussed later.

For the nonlinearity study, we use the average signal measured on each CCD channel separately, using 2D overscan subtraction and masking outlier pixels. The photodiode signal is simply bias-subtracted and time-integrated.

Technically, we model the nonlinearity using a spline function that we fit to the CCD/photodiode data pairs by minimizing:

$$= {}^2 \left(\frac{() + }{} \quad 1 \right)^2 \tag{1}$$

where is the CCD signal measured in exposure at LED current , is the corresponding photodiode signal, is the "photodiode factor" for current , is the spline nonlinearity correction, and is some weight. We add two constraints: the average of the spline over the fitting range is zero ¡ () = 0 ¿, and (0) = 0. We carry out this fit for all video channels separately. The weights are modeled using an expression determined empirically, $= 1/{}^2 + {}^2/$, and the two extra parameters, and are also fitted by modifying the expression 1:

$$= {}^2 \left(\frac{() + }{} \quad 1 \right)^2 \quad 2 \log \tag{2}$$

We fit the spline coefficients, the factors (there are typically 3 of them), and the weight parameters and . We perform an iterative 5 outlier rejection which rejects on average 0.5 % of the data points. We are firstly interested in the spline correction, and we give an example in Fig. 30.

4.5 Guider operation

This section describes guider operation.
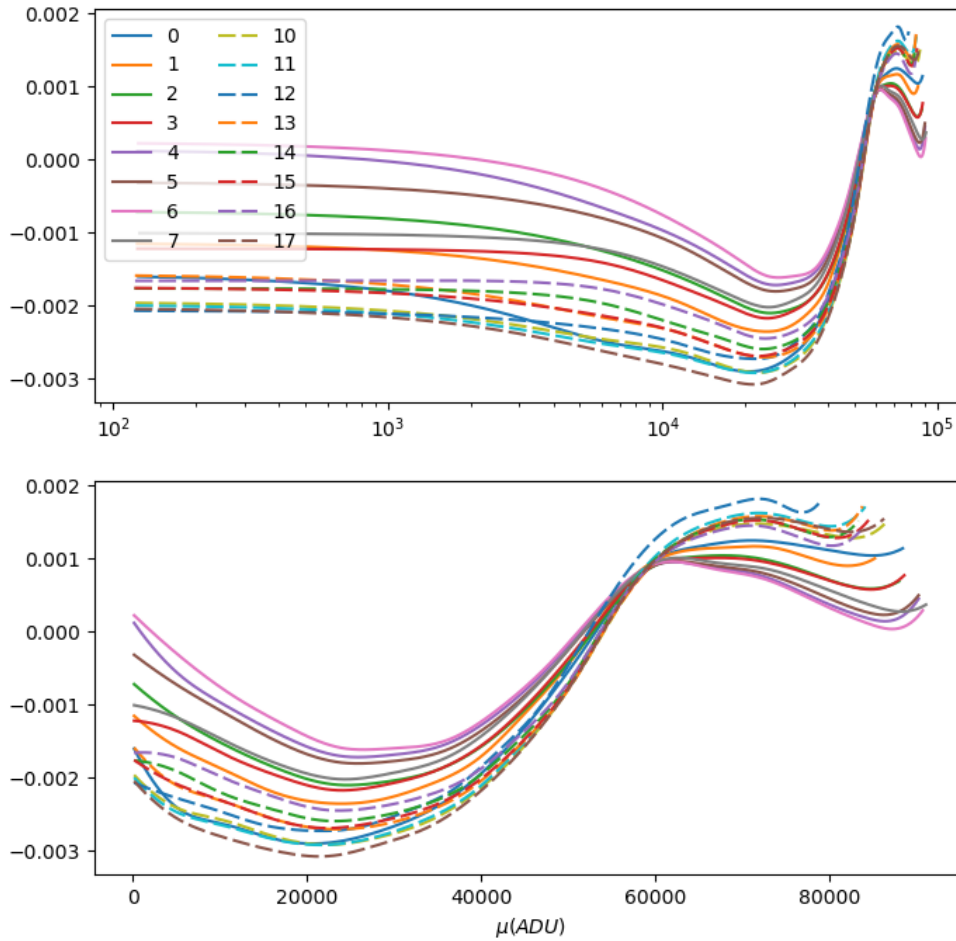
- Initial guider operation

Figure 30: Fitted non-linearity spline for the 16 channels of R22_S11 (using the PTC run E2016). The distortion around 60000 ADUs is due to the preamplifier. The curves obtained for the same sensor from another data set are extremely similar.

- Power cycling the guiders to get to proper mode
- Synchronization
- Guider ROI characterization

4.6 Defect stability

This section describes defect stability.

- Bright defects
- Dark defects with picture frame

4.7 Bias stability

We have found bias instabilities, typically above the 1 ADU level, for a number of CCDs in the focal plane, both ITL and e2v. Two main kinds of instability are observed:

1. ITL bias jumps : large variations of the column-wise structure from exposure to exposure.
2. e2v yellow corners : a residual 2D shape of the bias even after 2D-overscan correction. These residuals depend on the acquisition sequence and the exposure time, and the enhancement is greatest near the readout nodes (hence 'yelllow corner').

Both issues were observed and deeply studied in Run 6 EO data. The ITL issue is believed to be phase shifts in clocks between Readout Electronics Boards (REBs) because REBs rely on the frequency converted from their natural frequency. We tried to mitigate the e2v issue by optimizing the acquisition configuration in Run 7.

For the baseline acquisition configuration (see conclusion), three relevant stability runs were recorded:

1. Run E2136: 15 s darks with some very long delays throughout the run
2. Run E2236: 50 15 s darks, 50 biases recorded with 30 s delays between exposures
3. Run E2330: 15 s and 30 s darks with variable delays between exposures

To analyze these runs for bias instability, the eo_pipe bias stability task is used. For the ISR part, a serial ('meanper_row') overscan correction and a bias subtraction (computed from the corresponding B-protocol run) are applied. The final data product of the task is the mean of the per-amplifier science image over the full set of exposures of the run. Two typical examples from Run E2136 are shown in Figure 31. In the stable case, the variations are typically at the 0.1 ADU level; in the unstable case, the variations range up to 4 ADUs.

A comparison of the results for an unstable e2v CCD (R33_S02) is shown in Figure 32 for the three runs.
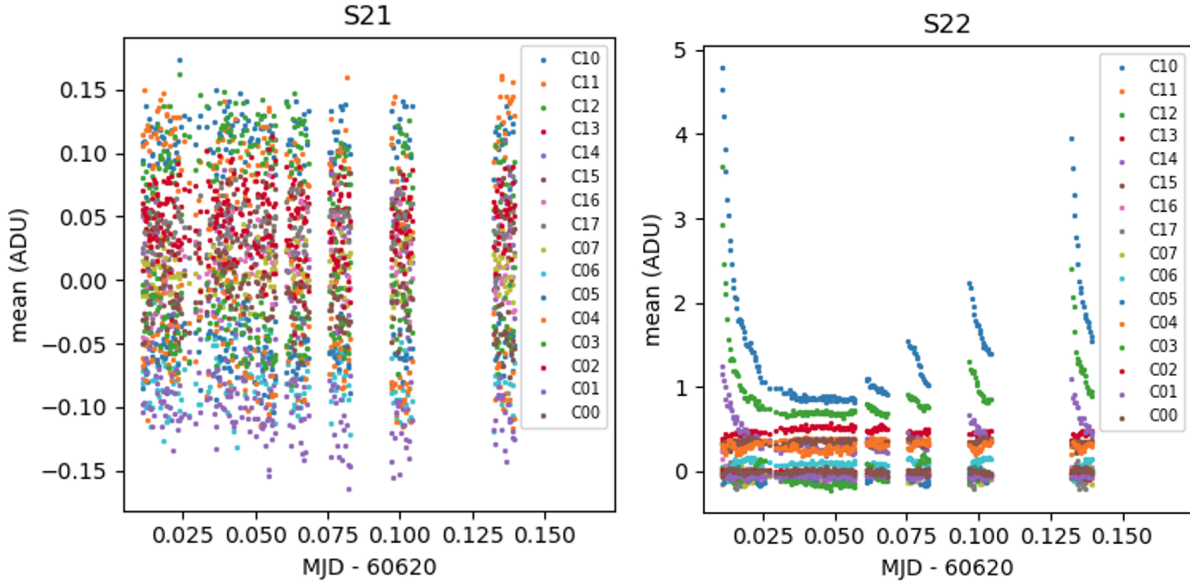
Figure 31: (left) Stable case for bias (R21_S21); (right) Unstable case (R23_S22)

To highlight the 2D shape differences in e2v bias instability, a 2D-overscan correction is applied. A few exposures illustrating the variations of the 2D shape for the same unstable CCD R33_S02 are shown in Figures 33-35. The 2D shape of the image in amplifier C01 is different in the 3 cases.

In order to quantify the number of unstable e2v amplifiers, a stability metric d is defined from the eo_pipe stability task data products. More precisely, d is defined, for a given amplifier in a given run, as the difference between the 5th and 95th percentiles of the image mean over all the bias image acquisitions. The distribution of d for run E2136 is shown in Figure 36. Applying a threshold at $0.3\,\text{ADU}$, 51 amplifiers are identified as unstable (see the corresponding mosaic in Fig. 37). This corresponds to ~3% of the e2v amplifiers.

Further studies are required in order to converge on the best mitigation strategy for the start of the LSST survey.

4.8 Gain stability

The "relative gain" is defined as the ratio of the signal observed in a CCD image segment divided by the integration of the photodiode current with respect to an arbitrary normalization. With a fixed flat illumination, the variation of the relative gain over successive exposures can be utilized to investigate the gain stability. We acquired flat images at the same flux level with two distinct temperature conditions: either intentionally altered or maintained constant.

- E1496 (dp80, constant temp, v29_Nop, nm750, 10k e-)
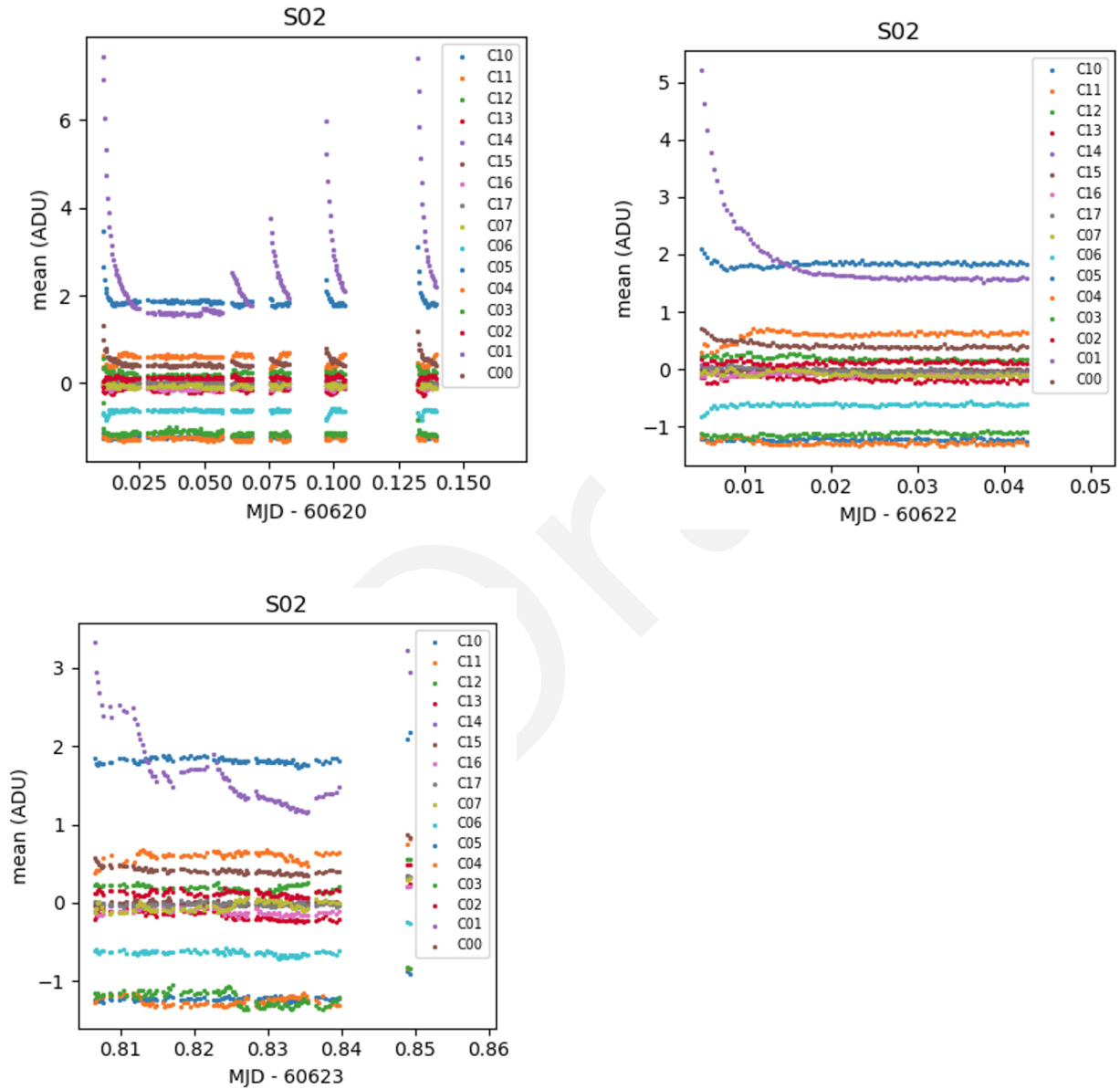
Figure 32: Bias level variations for R33_S02, an unstable e2v CCD for three runs: (upper left) E2136, (upper right) E2236, (lower left) E2330. The segments CXX and CYY are most strongly variable in each run. Note that the range of the time axes is different in each plot.
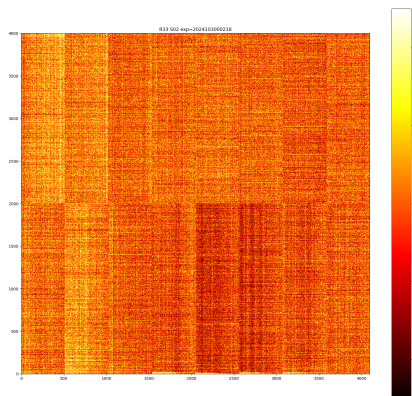
Figure 33: Bias exposure, run 1880, R33_S02
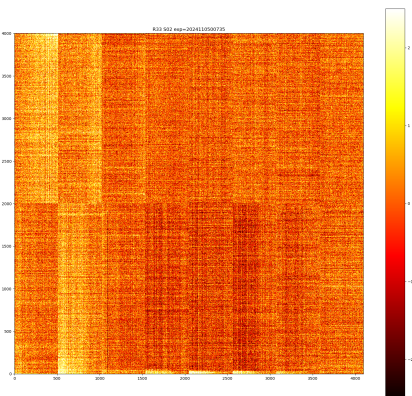
Figure 34: 15-s dark exposure, run E2136 in 'stable' conditions, R33_S02
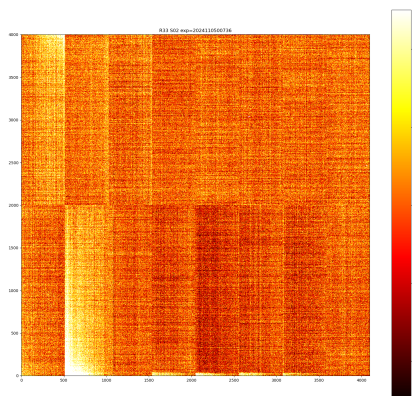
Figure 35: 15 s dark exposure, run E2136 after a 3 min delay, R33_S02
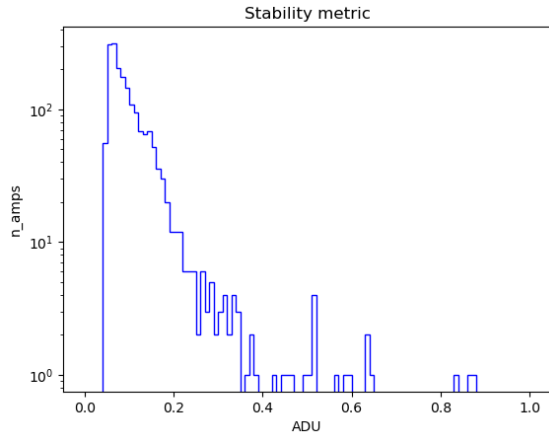
Figure 36: Distribution of the stability metric for the e2v amplifiers in run E2136
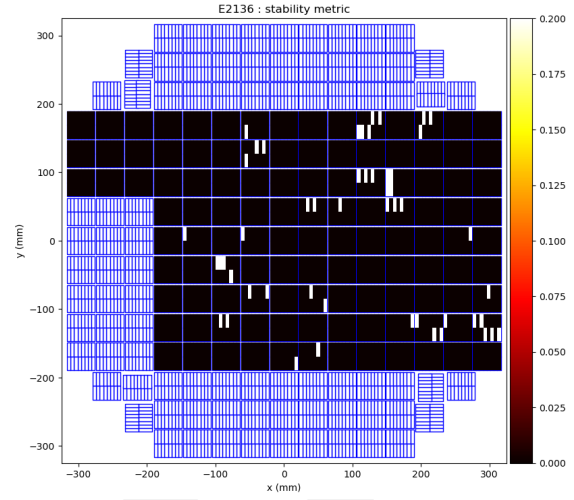
Figure 37: Mosaic of e2v amplifiers identified as unstable (white color) in run E2136

- E1367 (dp80, temp swing, v29, nm750, 50k e-)

- E756 (dp80, gain stability @ 50k e-)

- E1362 (dp80, 10k e-)

(YU: WORK IN PROGRESS)
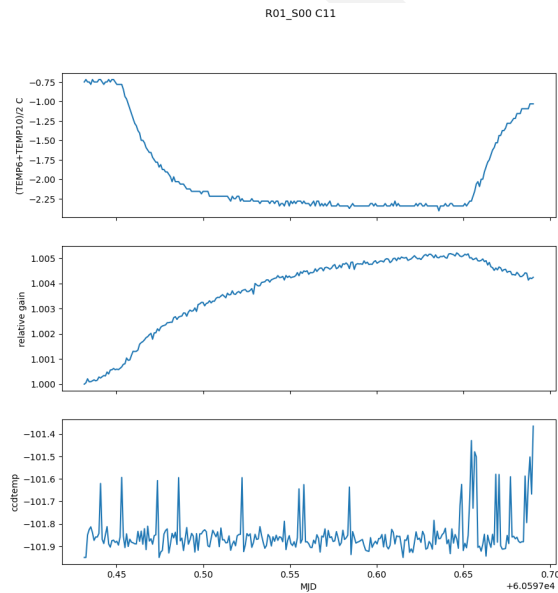
Figure 38: Distribution of the stability metric for the e2v amplifiers in run E2136
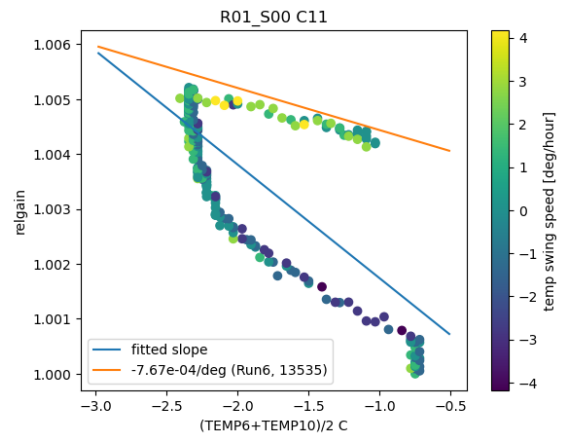
Figure 39: Mosaic of e2v amplifiers identified as unstable (white color) in run E2136

5 Sensor features

5.1 Tree rings

5.1.1 Center of the Tree Ring

So far we have been using the four average position for the center of the Tree ring, according to the pattern direction, however now we have new data with $0\,\text{V}$ of back bias voltage, we wanted to make sure if the error in center of the ring position is small enough and if we need to use individual center position for each sensor.

Figure 40 shows the positions of the Tree ring centers measured for the 189 sensors. We decided to use center of each sensor instead of the average value.
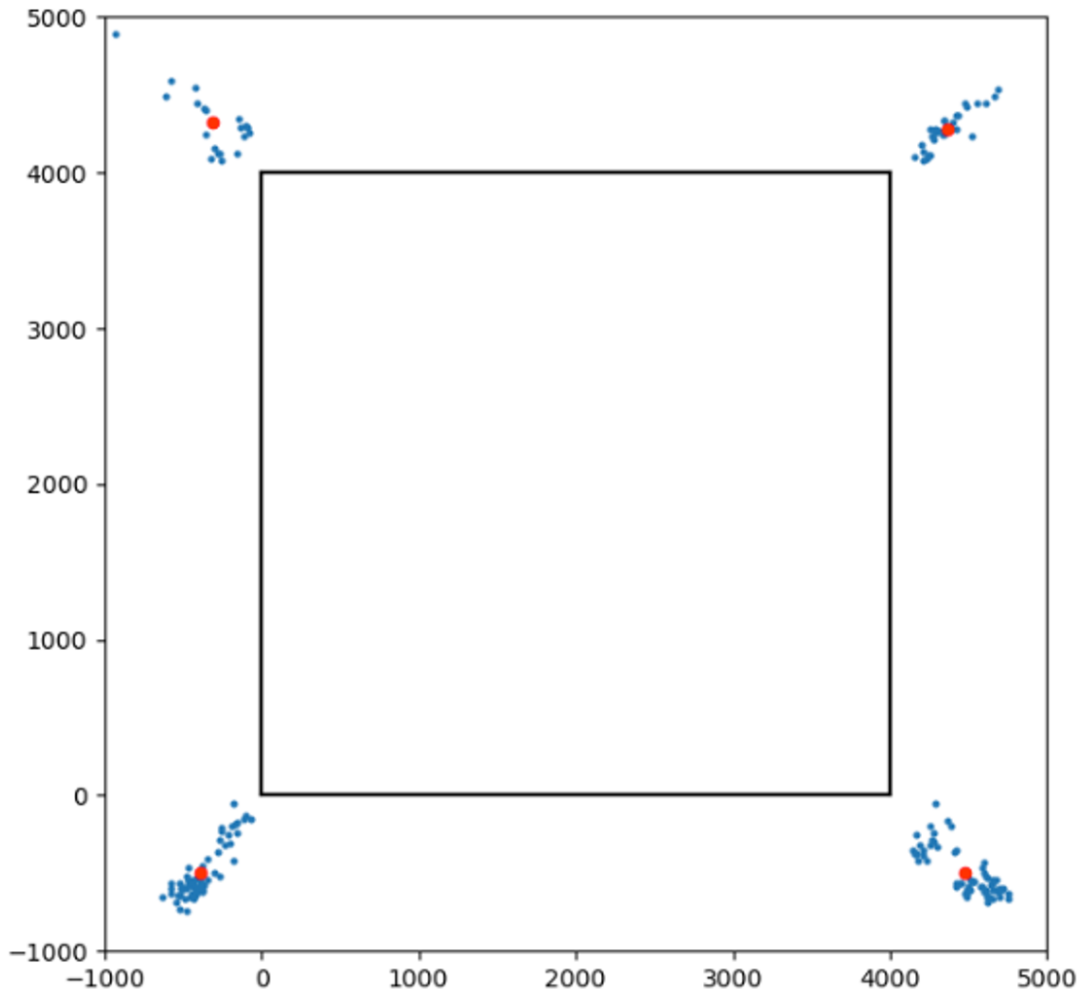
Figure 40: The center of the Tree Rings were measured for all 189 LSST sensors. Red point indicates the average center on each direction.

5.1.2 Radial study

Radial study for Tree rings pattern has been done to see if the rings are perfectly circular in shape.

Figure 41 illustrates the transformation of a flat image into a radial profile plot as the y axis to be the distance from the center of the rings.
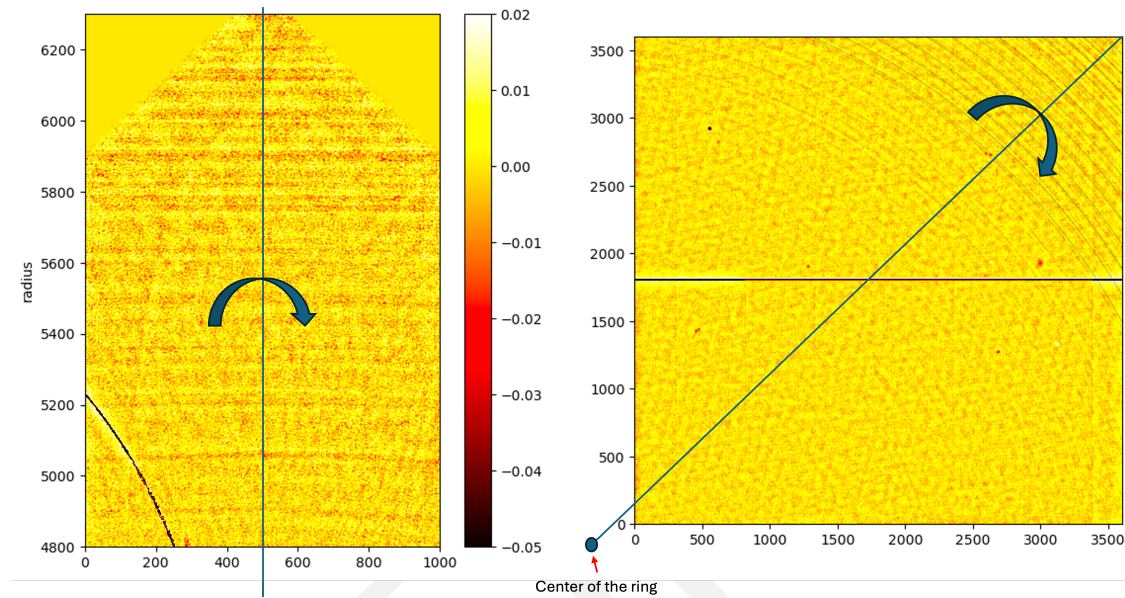
Figure 41: Folding image on diagonal line from the center of the ring, and subtracting from each other.
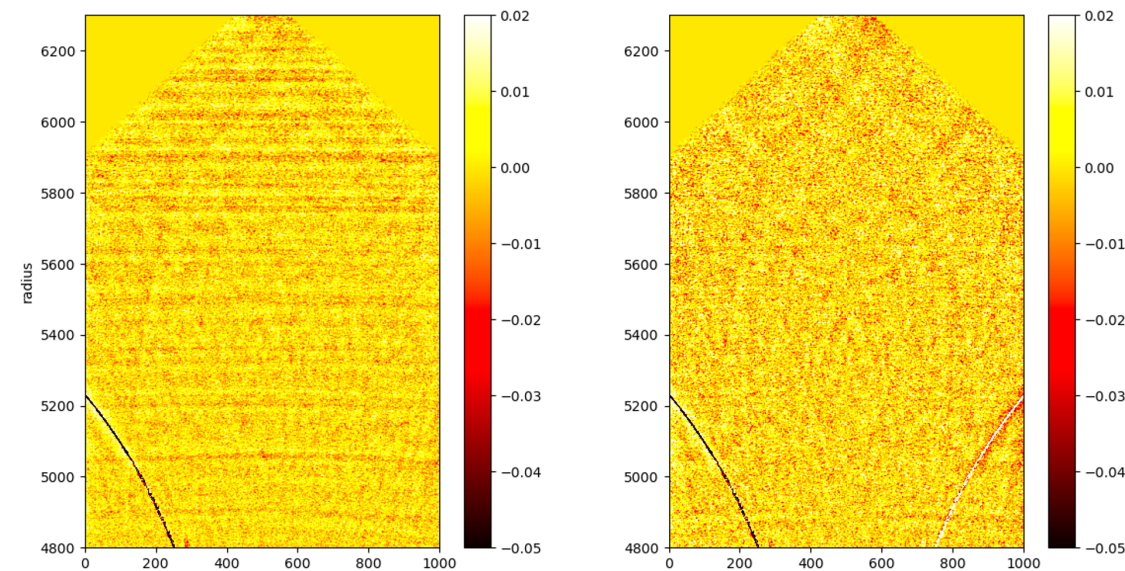
Figure 42: Radial study of the Tree Rings. Right: image subtracting left to right, right to left.

5.1.3 Effect of diffuser

We expect that with the diffuser installed, there will be less contribution from effects such as CMB and weather patterns discussed in § XX. Comparing R22_S12 of Run 6 run 13379 (without diffuser) with Run 7 E937 (with diffuser), we verified the significant improvement from use of the diffuser.
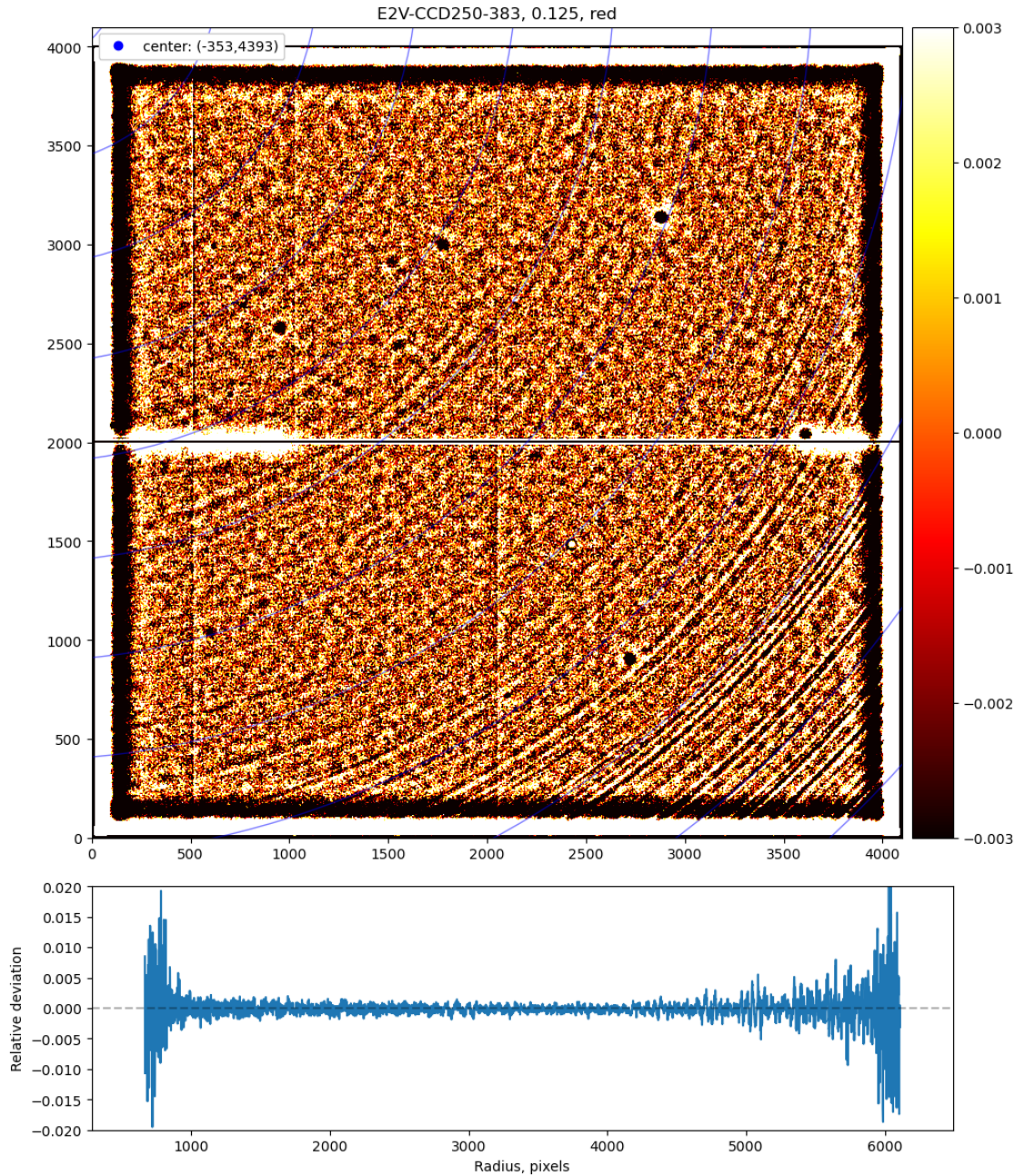
Figure 43: Tree ring without diffuser

5.1.3.1 Tree rings without diffuser
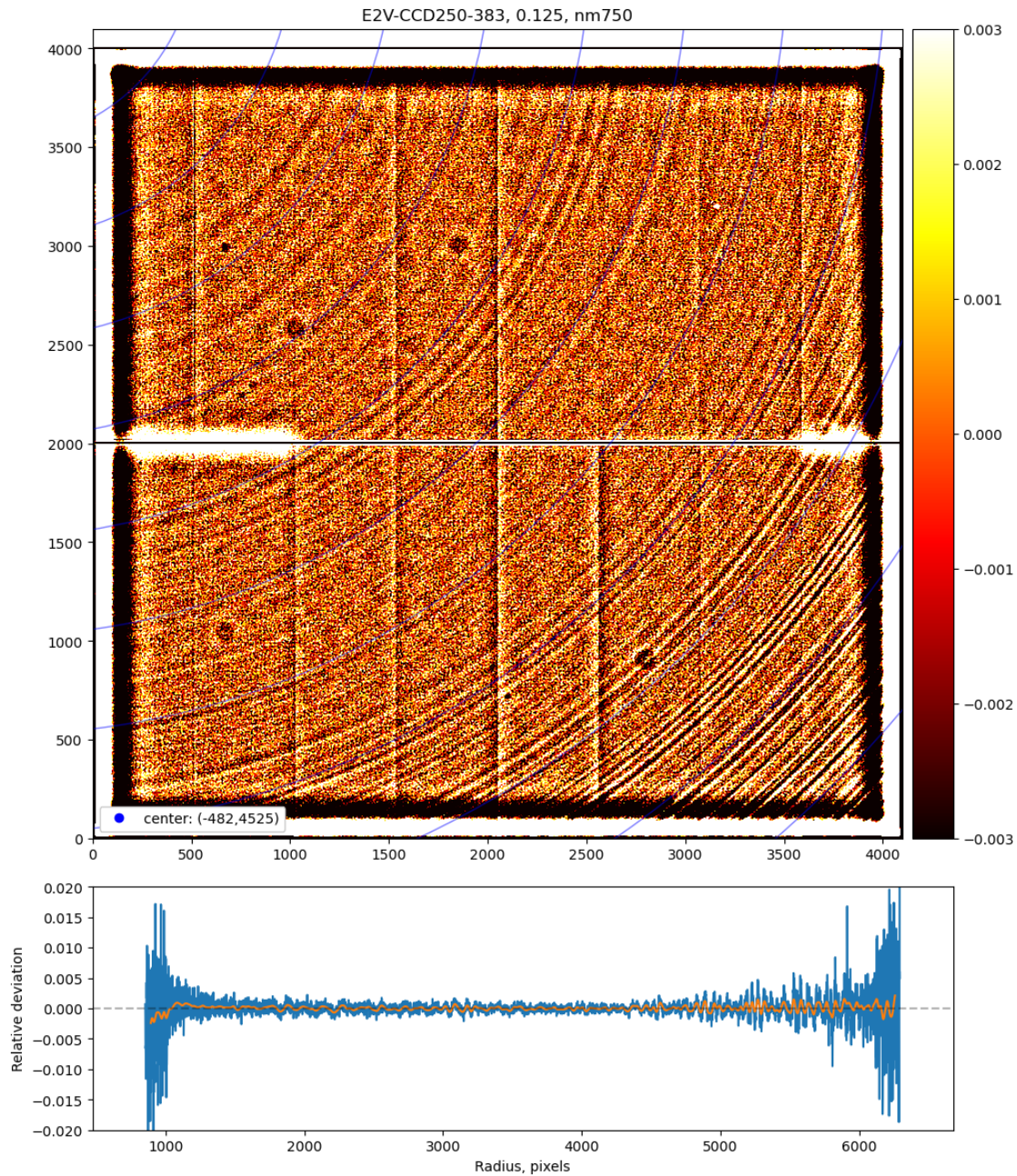
Figure 44: Tree ring with diffuser

5.1.3.2 Tree rings with diffuser

5.1.4 Voltage dependency

5.1.5 Wavelength dependency

5.2 ITL Dips

One of the phenomena that was studied in the later part of Run 7 was so-called 'ITL dips'. These were discovered in LSST ComCam on-sky data as bleed trails from bright stars that traversed the entire detector, crossing the amplifier boundaries. These bleed trails are unique though in that the core of the bleed trail is actually 'dark' compared to the wings of the trail, with a flux 2% less relative to the rest of the bleed trail.

We investigated whether ITL dips could also be observed in the CCDs of LSSTCam. For this study, we used spots and rectangles projected onto the focal plane by the 4K projector. The spots were approximately 30 pixels across and were projected onto every amplifier segment of each detector. The rectangles were only in the top right amplifier (C10). One consideration with this spot projection was that the projector also provided background illumination. This led to the spots having a peak signal only 6 times greater than the background and the rectangles having a peak signal 30 times greater than the background.

We were unable to find any evidence of ITL dips in the images. Below are the images themselves along with binned horizontal cutouts of the the amplifier below the source. These show the background pattern of the projector, but no 2% dip.

While we were not able to find evidence of the ITL dip in Run 7 data, it is still not clear whether the effect will be visible in LSSTCam on-sky data. The photon rate of the in-lab data was roughly XXX per second for the 15 s exposures. The stars that were seen in ComCam with the ITL dip have a magnitude of XXX corresponding to a photon rate of XXX. This is combined with a sky background of XXX as compared with the lab sensor background of XXX.

5.3 Vampire pixels

5.3.1 First observations

Vampire pixels were first observed in ComCam observations [need more info to properly give context] - Andy's study on Oct. 8 - Agnes masking effort

5.3.2 LSSTCam vampire pixel features

The vampire pixels have distinct features, both on the individual defect level, and across the focal plane

5.3.2.1 Individual vampire features

- General size
- Radial kernel
- uniformity

5.3.2.2 Vampire features across the focal plane

- sensor type
- static or dynamic
- higher concentrations? Particularly bad sensors?

5.3.3 Current masking conditions

- Bright pixels
- Dark pixels
- Jim's task

5.3.4 Analysis of flats

- LED effect
- Intensity effect

5.3.5 Analysis of darks

- Previous LED effect
- Intensity of LED effect
- dark cadence and exposure times

5.3.6 Current models of vampires

- Tony & Craig model
- Others?

5.4 Phosphorescence

The Run 7 persistence optimization process (cf. §3.1.1) used a short EO image acquisition sequence and analysis script, which rapidly provided persistence performance metrics as feedback for each configuration tested. Thus, as soon as the e2v sensors were shown to be nearly free of *their* undesirable effects by reducing their clock swing voltages from $9.3\,\mathrm{V}$ down to $8.0\,\mathrm{V}$, a similar persistence (or memory effect) was immediately noticed, affecting a subset of the ITL sensors. This discovery gained immediate interest for at least two reasons: (1) that it had not been detected in prior EO campaigns, and (2) that the new memory effect on certain ITL sensors was morphologically distinct from what had just been cured on the e2vs.

The ITL sensors with the largest memory effect were evaluated, and the following observations were made:

1. The morphology of the expressed memory effect in the first dark image acquired after the trigger (the saturation flat) was reminiscent of the *"coffee stains"* seen on the same sensors in flat field response, but with the opposite polarity. The "coffee stains" are commonly assumed to be associated with minor, localized variations in the sensors' antireflective coatings or

perhaps a very thin, dead layer associated with the backside surface: they tend to be larger in amplitude when shorter wavelengths are used to expose the sensors with flat field illumination.

2. The attenuation timescale of the memory effect is curiously comparable to the timescales that were seen in the persistence suffered by the e2v sensors (which are believed due to exposure of surface states by the collected conversions, on the semiconductor-insulator interface on the front side): exponential time constants of between 20 and 40 s, which unfortunately are in turn very close to the nominal exposure cadence for the LSST survey.

3. The similarity in memory effect time constants (de-trapping charges from surface states near the channel on the front side – the e2v case – vs. either de-trapping of charges located near the backside window surface or relaxation by photon emission by some excited states there – the ITL case) can be thought to favor the electron de-trapping mechanism, just from the other surface. Otherwise, the nearly matched time constants would have to be seen as an improbable coincidence.

4. A list of 12 ITL sensor serial numbers corresponding to those showing the memory effect was communicated to Mike Lesser at ITL. The list of parts shared certain properties according to his notes, and led him to develop a placeholder theory that would partially explain the mechanism. If true, it could explain what might be responsible for both the coffee stains and the memory effect with similar spatial distribution. He wrote that he tried, but was unsuccessful in diagnosing, using optical characterization tools (e.g., ellipsometer), any changes in optical constants on the affected regions of the "stained" sensors. The origin of the "stains", according to this theory, is as a consequence of there being "raised spots" on the sensors' backside surfaces that survive the final silicon acid etch. The raised silicon areas could potentially be trapping the resist used during the cleaning process that directly follows the etching step. Lesser wrote that the resist is wax-based and *does* fluoresce. If the theory is correct, he suggests that the medium would definitely be located *under* the AR coating and related neither to the coating nor the oxidation processes.

5. Discussions among the Rubin team led to the following distinction of terminology that served to name the ITL memory effect in question. The main difference between "fluorescence" and "phosphorescence" is in that the former is considered prompt re-emission and the later could be re-emission following a finite characteristic time constant. Characteristic time constants are in the nanosecond scale for fluorescence, while for phosphorescence it would be in the milliseconds to seconds range. For the purpose of this discussion, we adopt the word "phosphorescence" to refer to the memory effect present in some ITL sensors.

6. Lesser mentioned that the wax-based resist fluoresces (that would be the prompt mechanism with very short relaxation time). If there is any such residual material between the coating and the passivated silicon, it would be natural to expect a halo that would accompany any sharp (PSF-scale features) illumination that passes through these "stains" on the sensor surface: a scatter term with low integrated amplitude, whose scale should depend upon the re-emission wavelength. This has not yet been seen in lab data but may appear once the Camera goes on-sky.

5.4.1 Measurement techniques for detecting and quantifying phosphorescence

We mentioned above that certain phosphorescent morphologies strongly resemble the "coffee stains" seen on the same (ITL) sensors. It should be noted that measurement of the *shadow* caused by excess absorption (usually a couple percent) is a great deal simpler than collecting any deferred charge with adequate sensitivity and confidence. This section describes the methods used to identify the transient term we consider phosphorescence in the ITL sensors, and list the regions where it was detected. Following that, we describe in some detail the kinematics of its expression (cherry-picking specific easy-to-measure cases), together with the wavelength- and its excitation flux-level dependence.

We parasitically used a series of B-protocol and BOT-persistence EO testing runs that were executed for the purpose of tuning the operation of e2v sensors. The reason for this was that the ITL operating parameters were left unchanged from run to run, and thereby provided multiple instances of the same EO measurement conditions, although the acquisitions were captured over a span of a few weeks. The relevant EO runs acquired a series of dark images (with the nominal 15 s integration time, or 'EXPTIME') that followed a deliberate overexposure and readout of a FLAT (CCOB LED 'red', target signal 400 ke/pix). The dark images acquired in succession following the FLAT image recorded the re-emitted or deferred signal collected within each 15 s period, and there were 20 such dark images acquired within each EO run. In all, we identified and analyzed a total of 22 runs containing this data, where the excitation flat had the properties described above. The first and the twentieth dark images were stacked and medianed following a nominal instrumental signal removal (ISR) step. The twentieth median dark images were then subtracted from the first median darks. This further suppressed any remaining ISR residuals from the pixel data, which nominally now contain the *transient term* of the ITL phosphorescence, because as far as we could tell, the 15 s expression of the deferred signal 300 s after overexposure had almost completely attenuated.

5.4.2 Results of phosphorescence detection in ITL sensors

Table 5 provides the EO run IDs analyzed according to the process outlined above. Figures 48 through 59 display the transient term in 8»8 blocked images of the 12 rafts containing ITL sensors. These serve primarily to help identify which ITL sensors exhibit regions where we suspect presence

of the phosphorescence effect. It should be noted that we retained the full 1»1 pixel resolution images for follow-up inspection, because there is no guarantee that high spatial frequencies in the phosphorescence expression will not be washed out by the rebinning routinely performed for display purposes.

A subset of the 88 sensors, specifically those that either show high-signal diffuse, or morphologically unique structure in the transient term of the phosphorescence detected, are singled out to compare side-by-side with *blue* CCOB LED flat illumination, in Figures 60 through 65 in the Appendix. It is apparent from viewing these side-by-side comparisons that generally, expression of phosphorescence has a complex relationship with the *much-easier-to-detect* coffee stains (or other diffuse variations in quantum efficiency) seen on the same sensors: Presence of a coffee stain seen in flat field response may be suggestive of phosphorescence on the sensor, but predicting where it might be (or its transient amplitude) is another matter entirely. In some cases (as in Fig. 45 noted above), the phosphorescence appears to be correlated with the darker absorbed features of the coffee stain. In others (e.g., Fig. 61), the opposite correlation is seen. In still other cases (e.g., Fig. 62), there are regions of strong detail in the phosphorescence without very much coffee stain action at all. Our conclusions are that presence of coffee stains do not provide a useful proxy for the phosphorescent properties of the sensor.

Table 5: Zephyr Scale E-numbers and corresponding SeqIDs analyzed to estimate phosphorescence in the 88 ITL sensors.

Run numbers and SeqIDs of first dark following trigger		
B-protocol runs, HVBias *off*, HVBias *on* for Corners		
E1003:20240920_000056	E1009:20240921_000222	E1003:20240920_000056
B-protocol runs, HVBias *on*		
E1071:20240924_000300	E1110:20240926_000242	E1144:20240927_000369
E1146:20240928_001525	E1195:20241002_000235	E1245:20241003_000245
E1290:20241008_000286	E1329:20241011_001555	E1363:20241012_000546
E1392:20241014_000444	E1396:20241014_000701	E1411:20241015_000322
E1419:20241016_000397	E1429:20241016_000742	E1449:20241017_000548
E1497:20241020_000225	E1812:20241028_000481	E1880:20241030_000432
E2233:20241108_001468	E3380:20241130_000355	
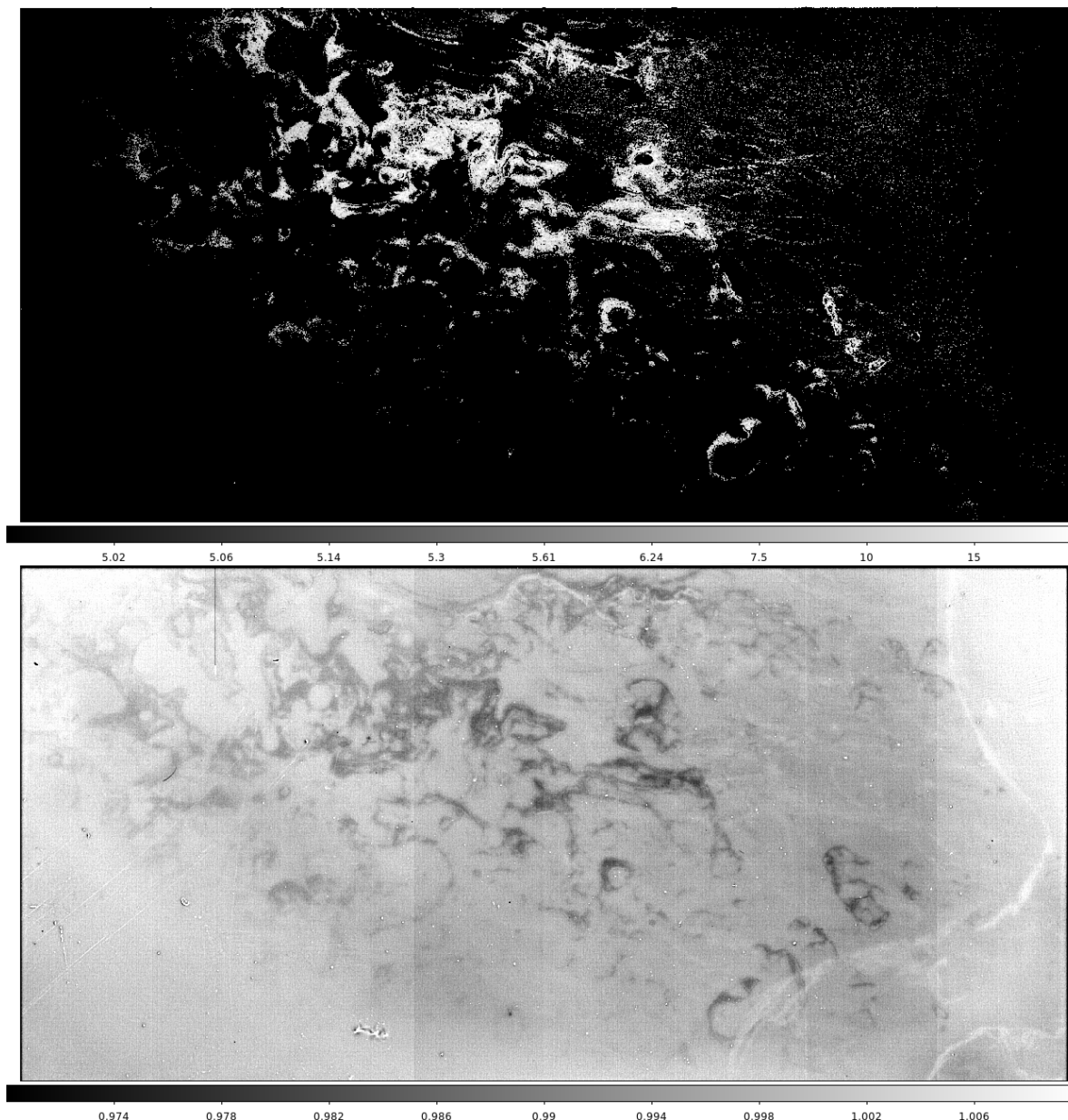
Figure 45: R00_SW1 image showing phosphorescence (top) with morphology similar to the "coffee stains" (bottom) observed with *blue* CCOB LED illumination. The phosphorescence acquired in dark exposures within the first 15 s following trigger (top) uses a logarithmic stretch with limits 5–25 e/pixel. The *blue* flat field (bottom) is displayed normalized, with 4% stretch limits (0.97 to 1.01), for a target signal level of 10^4 e/pixel. Note that the phosphorescence pattern resembles the dark wisps in the flat (with opposite polarity) but that there are apparently no significant phosphorescence features corresponding to the bright wisps.

While characterizing the phosphorescence expressed by ITL sensors using the data products described above, we have also identified correlations that concerns the localized, phosphorescence centers that tend to appear as circular disks. While we typically see a dozen or so (on average) per sensor, those with larger amplitude are strongly associated with *vampire pixels* (which are easily identified by their localized flat field response). The correlation is not perfect, meaning that not all localized (circular) phosphorescence centers can be associated with *vampire pixels* but that nearly all *vampire pixels* express localized phosphorescence with some amplitude.

When data products of the 88 ITL sensors are inspected for transient phosphorescent response, very few, perhaps only a single sensor, show insignificant phosphorescence. Although 24% of the ITL sensors show diffuse phosphorescence, a majority of sensors (83%) show spot-like phosphorescence centers. Presence of diffuse phosphorescence probably can frustrate spot-like phosphorescence detection by eye, and the estimated frequency of the latter may consequently serve as a lower limit to the true frequency. The identification of the sensor groups is given in Table 6.

Table 6: Qualitative grouping of the 88 ITL sensors based on inspection of full resolution representations of Figures 48 through 59. In cases of spot-like phosphorescence, the number of features counted are given within ellipses. Transient features appearing similar to *hot columns* or as other connected pixel groups are additionally signified with a double-plus (++).

Sensor Grouping		
Sensors exhibiting insignificant phosphorescence		
R44_SW1		
Spot-like phosphorescence (vampire transients)		
R00_SG0(¿36)	R00_SG1(¿36)	R00_SW0(¿10)
R01_S00(¿33)	R01_S01(¿4)	R01_S02(¿6)
R01_S10(¿25)	R01_S11(18)	R01_S12(14)
R01_S20(¿23)	R01_S21(¿30)	R01_S22(¿30)
R02_S00(¿32++)	R02_S01(¿36)	R02_S02(¿28)
R02_S10(6)	R02_S11(¿30)	R02_S12(¿25)
R02_S20(¿14)	R02_S21(¿9)	R02_S22(¿6++)
R03_S00(13)	R03_S01(12)	R03_S02(¿19)
R03_S10(9)	R03_S11(3)	R03_S12(10)
R03_S20(9)	R03_S21(18++)	R03_S22(16)
R04_SG0(¿12)	R04_SG1(¿30++)	R04_SW0(25)

Continued on next page

Table 6 – continued from previous page

Sensor Grouping		
R04_SW1(¿30)	R10_S00(¿30)	R10_S01(9)
R10_S02(32)	R10_S11(16)	R10_S12(¿26)
R10_S20(21)	R10_S21(¿11++)	R10_S22(¿10++)
R20_S00(2)	R20_S01(8)	R20_S02(7)
R20_S10(¿35)	R20_S11(7)	R20_S12(5)
R20_S20(10)	R20_S21(5)	R20_S22(5)
R40_SG0(¿50++)	R40_SG1(6++)	R40_SW0(6)
R40_SW1(8)	R41_S00(9++)	R41_S01(16)
R41_S02(10)	R41_S10(12)	R41_S11(3)
R41_S12(10++)	R41_S20(5++)	R41_S21(30)
R41_S22(3)	R42_S00(24)	R42_S01(6)
R42_S02(¿10)	R42_S10(4)	R42_S11(11)
R42_S12(33)	R42_S20(7)	R42_S21(5)
R42_S22(4)	R43_S00(22++)	R43_S01(30)
R43_S02(19)	R43_S10(26)	R43_S12(8++)
R43_S21(14)	R43_S22(4)	R44_SG0(¿12)
R44_SG1(¿10)	R44_SW0(18)	

Segments exhibiting diffuse transient phosphorescence		
R00_SG1_C10-12,C03-05 (++)	R00_SW0_C17	R00_SW1_C** (++)
R01_S00_C13-14 (++)	R01_S01_C07,C16-17	R01_S10_C00-01,C14-16
R01_S20_C04-07	R01_S21_C06-07,C17	R01_S22_C00-01,C15-17
R02_S02_C03-04	R02_S11_C13-17,C07 (++)	R02_S12_C04-07,C10-12
R02_S20_C06-07	R04_SG1_C01,C11 (++)	R10_S10_C10,C16-17,C07
R40_SG0 (++)	R41_S21_C00,C10	R42_S00_C01,C07,C17
R43_S11 (++)	R43_S20_C00-01 (++)	R44_SG1_C07

The correspondence between *vampire pixels* and spot-like phosphorescence is laid out in Figure 46, for two prominent cases. These two *vampire pixels* may appear intrinsically different in that their flat-field responses **do** (or do **not**) exhibit a central bright pixel, which could aid in their identification. Details of the underlying distribution of trapped surface charges near the back-side electrode - or variations in the conductive properties of the same - apparently drive these details of the

flat field response. However, it remains intriguing that these surface electrostatic properties are accompanied by an unmistakable transient phosphorescence signature.

(a) flat field (blue) response, R03_S10 ROI (b) transient phosphorescence, R03_S10 ROI

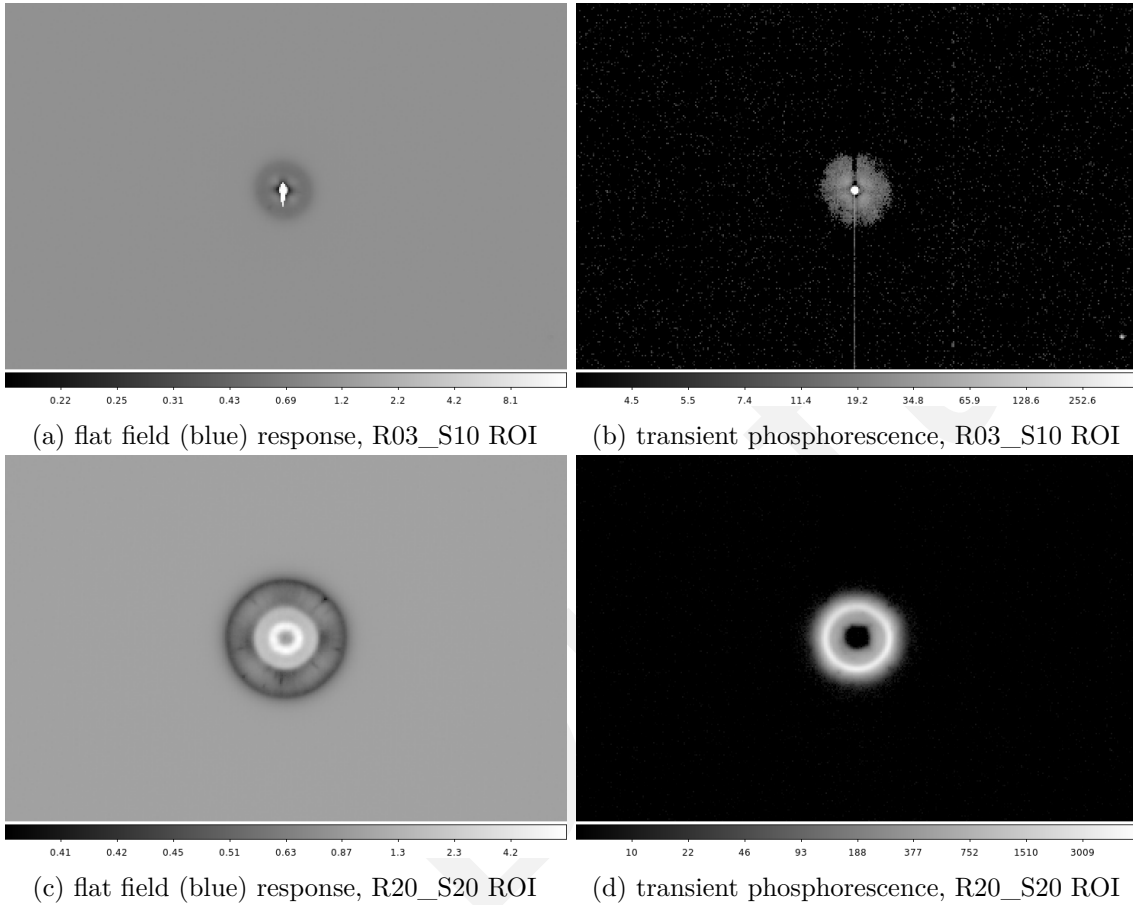(c) flat field (blue) response, R20_S20 ROI (d) transient phosphorescence, R20_S20 ROI

Figure 46: Vampire pixel comparisons between their flat field response and their transient phosphorescence. Signal levels are given (relative for flat field response, absolute electrons per 15s following overexposure for transient phosphorescence). The relative flat field response amplitudes swing between 0.2 & 16 (reaching full well) for R03_S10, and between 0.4 & 8 for R20_S20. The transient phosphorescence response also reaches nominal full well (135ke/pix/15s for the central pixel) for R03_S10, and a lower amplitude (3-4ke/pix/15s for several hundred pixels) is reached for R20_S20.

A curious aspect of the phosphorescence seen in ITL sensors lies in its voltage (HV Bias) dependence. The HV Bias, when turned on, reduces lateral diffusion of the photo-conversions and thereby maintains PSF image quality. In Figure 47 we compare side-by-side several phosphorescent regions with both HVBias states (off and on). There appears to be no trend that lends to predictability in these cases. In the cases of vampire pixels (R03_S10 & R20_S20), the geometry of the phosphorescence is indeed very sensitive to the HV Bias states (cf. Figs 47a vs. 47b; 47c vs. 47d). These might be understood qualitatively However, for the diffuse phosphorescence examples, the expres-

sion appears to vanish entirely (R43_S11, Fig. 47e) or become significantly stronger, together with morphological changes (R43_S20, Fig. 47g) when the HV Bias is switched off.

5.4.3 Other properties of phosphorescence

- Dependence on HVBiasOn vs. HVBiasOff
- Dependence on wavelength of the triggering exposure
- Kinetics of the phosphorescence (based on *blue* CCOB LED)

- phosphorescence background
- phosphorescence on flat fields
- phosphorescence on spot projections

6 Conclusions

6.1 Run 7 final operating parameters

This section describes the conclusions of Run 7 optimization and the operating conditions of the camera. Decisions regarding these parameters were based upon the results of the voltage optimization, sequencer optimization, and thermal optimization.

6.1.1 Voltage conditions

Table 7: Voltage conditions

Parameter	dp80 (new voltage)	dp93 (Run 5)
pclkHigh	2.0	3.3
pclkLow	6.0	6.0
dpclk	8.0	9.3
sclkHigh	3.55	3.9
sclkLow	5.75	5.4
rgHigh	5.01	6.1
rgLow	4.99	4.0
rd	10.5	11.6
od	22.3	23.4
og	3.75	3.4
gd	26.0	26.0

6.1.2 Sequencer conditions

(a) HVBias off, R03_S10 ROI

(b) HVBias on, R03_S10 ROI

(c) HVBias off, R20_S20 ROI

(d) HVBias on, R20_S20 ROI

(e) HVBias off, R43_S11 ROI

(f) HVBias on, R43_S11 ROI
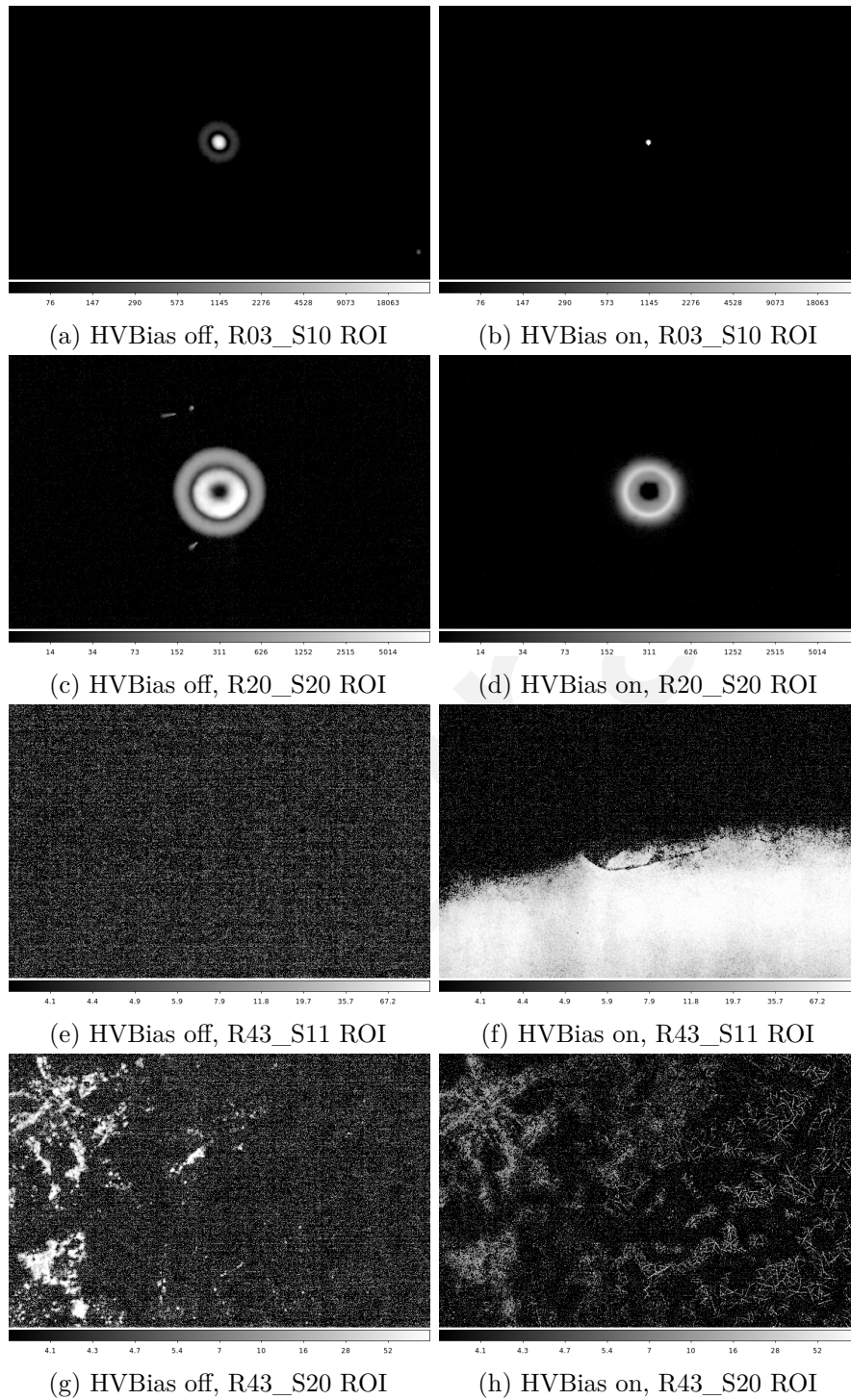
(g) HVBias off, R43_S20 ROI

(h) HVBias on, R43_S20 ROI

Figure 47: Comparisons of transient phosphorescence between conditions where HV Bias is off (left) vs. on (right). Four different ROIs are shown, but with image scales set to match across HV Bias conditions.

Table 8: Sequencer conditions

Detector type	File name
e2v	FP_E2V_2s_l3cp_v30.seq
ITL	FP_ITL_2s_l3cp_v30.seq

- v30 sequencers are identical to the FP_ITL_2s_l3cp_v29_Noppp.seq and FP_E2V_2s_l3cp_v29_NopSf.s
  All sequencer files can be found in the GitHub repository.

6.1.3 Other camera conditions

- Idle flush disabled

6.2 Record runs

This section describes Run 7 record runs.

All runs use our camera operating configuration, unless otherwise noted.

Table 9: Record runs

Run Type	Run ID	Links	Notes
B protocol	E1880		
	E2233		Identical to E1880. Acquired after CCS subsystem reboot
	E1886		Red LED dense. Dark interleaving between flat pairs
	E1881		Red LED dense. No dark interleaving between flat pairs
PTCs	E748		nm960 dense
	E2237		Red LED dense. Acquired after CCS subsystem reboot.
	E2016		Super dense red LED. HV Bias off for R13/Reb2. jGroups meltdown interrupted acquisitions, restarted
Long dark acquisitions	E1117		
	E1116		
	E1115		
	E1114		
	E1075		
Projector acquisitions	E1558		Flat pairs, fine scan in flux from 1–100 s in 1 s intervals. E2V:v29Nop, ITL:v29Nopp
	E1553		Flat pairs, coarse scan in flux from 5–120 s in 5 s interval.E2V:v29Nop, ITL:v29Nopp

Run Type	Run ID	Links	Notes
	E1586		One 100 s flat exposure, spots moved to selected phosphorescent regions.E2V:v29Nop, ITL:v29Nopp
	E2181		Flat pairs from 2–60 s in 2 s intervals. Two 15 s darks interleaved after flat acquisition. Rectangle on C10 amplifier.E2V:v29Nop, ITL:v29Nopp
	E2184		10 30 s dark images to capture background pattern
	E1717		Long dark sequence, no filter changes
	E2330		Short dark sequence, filter changes in headers through OCS
OpSim runs	E1414		30 minutes OpSim run with shutter control, filter change, and realistic survey cadence
	E2328		Flats with shutter-controlled exposure
	E1657		10 hour OpSim dark run, ~50% of darks were acquired properly
	E2015		10 flats at 10 ke followed by 10»15 s darks
	E2014		1 flat at 10 ke followed by 10»15 s darks
Phosphorescence datasets	E2011		20 flats at 10 ke followed by 10»15 s darks
	E2012		10 flats at 1 ke followed by 10»15 s darks
	E2013		10 flats at 10 ke followed by 10»15 s darks. Interleaved biases with the darks
	E1050		
	E1052		
	E1053		
	E1055		
Tree ring	E1056		
flats	E1021		
	E1023		
	E1024		
	E1025		
	E1026		
	E1955		
	E2008		
Gain	E1968		
stability	E1367		
runs			

Run Type	Run ID	Links	Notes
	E1362		
	E756		
	E1496		
	E1503 E1504		
	E1505		
	E1506		
	E2286		
	E1502		
	E1501		
	E1500		
	E1499		
	E1498		
	E1494		
Persistence datasets	E1493		
	E1492		
	E1490		
	E1491		
	E1489		
	E1488		
	E1487		
	E1486		
	E1485		
	E1478		
	E1477		
	E1479		
	E1483		
	E1484		
	E1510 E1518		
	E1519		
	E1508		
	E1509		

Guider ROI
acquisitions

Run Type	Run ID	Links	Notes
	E1520		
	E1511		
	E1521		
	E1512		
	E1513		
	E1514		
	E1517		

A2023 https://arxiv.org/pdf/2301.03274

Astier https://www.aanda.org/articles/aa/abs/2019/09/aa35508-19/aa35508-19.html

Bipolar https://github.com/lsst-camera-dh/mkconfigs/blob/master/newformula.py

D2014 https://ui.adsabs.harvard.edu/abs/2014SPIE.9154E..18D/abstract

DavisReport https://docs.google.com/document/d/1V4o9tzKBLnI1nlOlMFImPko8pDkD6qE7 jzzk-duE-Qo/edit?tab=t.0#heading=h.frkqtvvyydkr

EPER https://www.spiedigitallibrary.org/journals/Journal-of-Astronomical-Telescopes-Instrum ents-and-Systems/volume-7/issue-4/048002/Characterization-and-correction-of-serial-defer red-charge-in-LSST-camera/10.1117/1.JATIS.7.4.048002.full

J2001 https://www.spiedigitallibrary.org/ebooks/PM/Scientific-Charge-Coupled-Devices/eIS BN-9780819480392/10.1117/3.374903

Persistence https://dmtn-276.lsst.io/

PersistenceMitigationVoltage https://github.com/lsst-camera-dh/e2v_voltages/blob/main/ setup_e2v_v4.py

S2024 https://ui.adsabs.harvard.edu/abs/2024SPIE13103E..21S/abstract

U2024 https://ui.adsabs.harvard.edu/abs/2024SPIE13103E..0WU/abstract

dmtn-276 https://dmtn-276.lsst.io

sequencerV23_DC https://github.com/lsst-camera-dh/sequencer-files/blob/master/run5/F P_E2V_2s_ir2_v23_DC.seq

sequencerV29 https://github.com/lsst-camera-dh/sequencer-files/blob/master/run7/FP__E2V__2s_l3cp_v29.seq

sequencerV29__Nop https://github.com/lsst-camera-dh/sequencer-files/blob/master/run7/FP__E2V__2s_l3cp_v29__Nop.seq

sequencerV29__NopSf https://github.com/lsst-camera-dh/sequencer-files/blob/master/run7/FP__E2V__2s_l3cp_v29__NopSf.seq

A FCS work

B eo-pipe reference figures

C CCS work

C.1 JGroups issue

D OCS integration

E Phosphorescence identification on ITL set of sensors

F Phosphorescence morphological comparisons with features seen in *blue* flat field response

The following images (Figures 60 through 65) are an incomplete selection of ITL sensors with phosphorescence. They compare expressed phosphorescence (transient term) with the *blue* CCOB LED flat response.

A References

References

Astier, P., Antilogus, P., Juramy, C., et al., 2019, A&A, 629, A36 (`arXiv:1905.08677`), doi:10.1051/0004-6361/201935508, ADS Link

[**DMTN-276**], Banovetz, J., Utsumi, Y., Slater, C., 2024, Effects of Persistence on E2V Sensors and its Impacts on DC2 Data, URL https://dmtn-276.lsst.io/,
Vera C. Rubin Observatory Data Management Technical Note DMTN-276

B Acronyms

Acronym	Description
2D	Two-dimensional

3D	Three-dimensional
AC	Access Control
ADC	atmospheric dispersion corrector
ADU	Analogue-to-Digital Unit
B	Byte (8 bit)
BOT	Bench for Optical Testing
CCD	Charge-Coupled Device
CCOB	Camera Calibration Optical Bench
CCS	Camera Control System
CMB	Cosmic Microwave Background
CMOS	complementary metal-oxide semiconductor
CTI	Charge Transfer Inefficiency
DC	Data Center
DMTN	DM Technical Note
EO	Electro Optical
FES	Filter Exchange System
IR	infrared
ISR	Instrument Signal Removal
ITL	Imaging Technology Laboratory (UA)
L1	Lens 1
LCA	Document handle LSST camera subsystem controlled documents
LED	Light-Emitting Diode
LSST	Legacy Survey of Space and Time (formerly Large Synoptic Survey Telescope)
LaTeX	(Leslie) Lamport TeX (document markup language and document preparation system)
MC	Monte-Carlo (simulation/process)
OCS	Observatory Control System
OpSim	Operations Simulation
PCTI	Parallel Charge Transfer Inefficiency
PM	Project Manager
PSF	Point Spread Function
PTC	Photon Transfer Curve
REB	Readout Electronics Board
RTM	Raft Tower Module

| S3	(Amazon) Simple Storage Service
SCTI	Serial Charge Transfer Inefficiency
SE	System Engineering
SLAC	SLAC National Accelerator Laboratory
TMA	Telescope Mount Assembly
UCD	Unified Content Descriptor (IVOA standard)
UT	Universal Time
UTC	Coordinated Universal Time
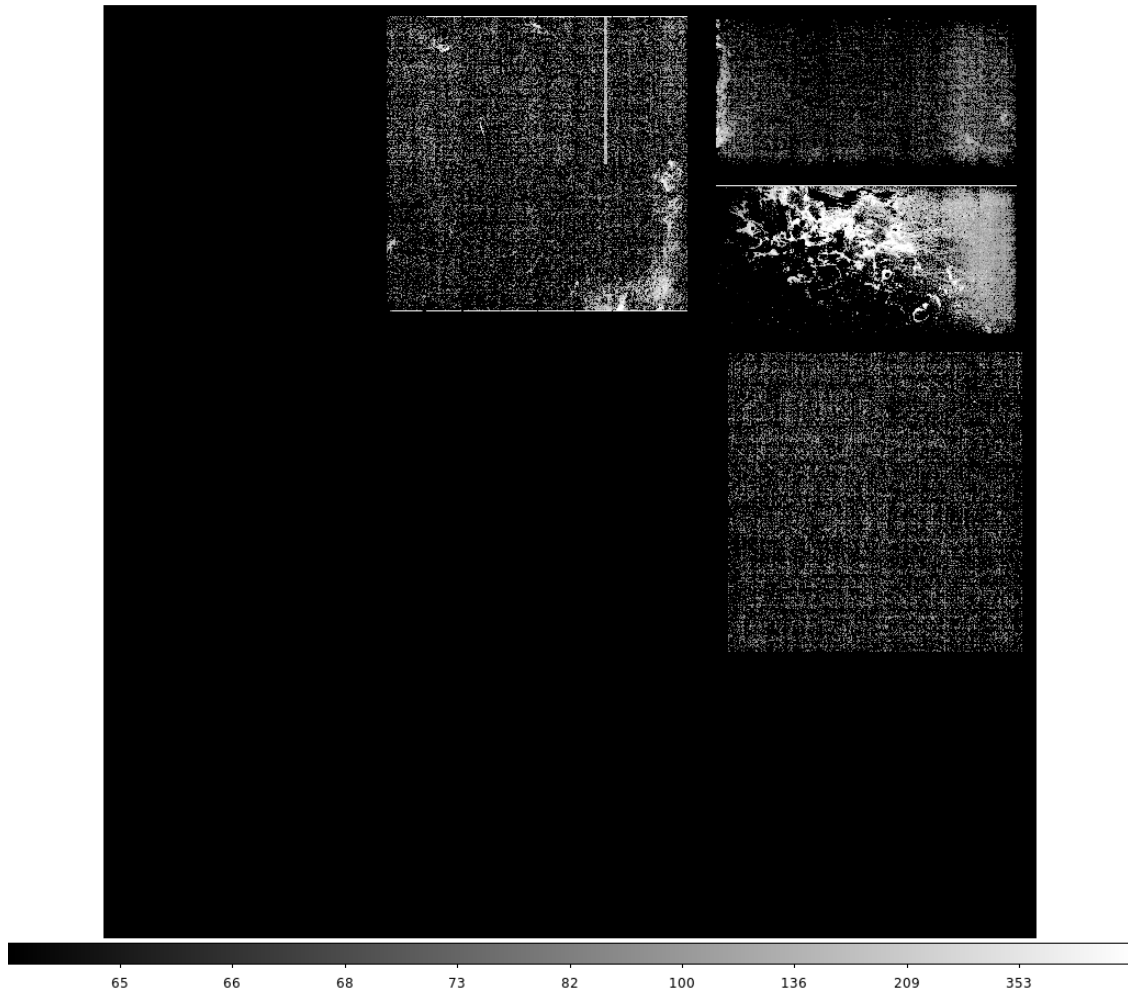
Figure 48: Phosphorescence transients for the R00 CRTM captured in the first 15 s following *red* CCOB LED at 400 ke/pix. With 8»8 blocking, the upper end of the color scale (640) corresponds to 10 e/pixel when averaged over 64 pixels contributing.

Figure 49: Phosphorescence transients for the R01 RTM captured in the first 15 s following *red* CCOB LED at 400 ke/pix. With 8»8 blocking, the upper end of the color scale (640) corresponds to 10 e/pixel when averaged over 64 pixels contributing.
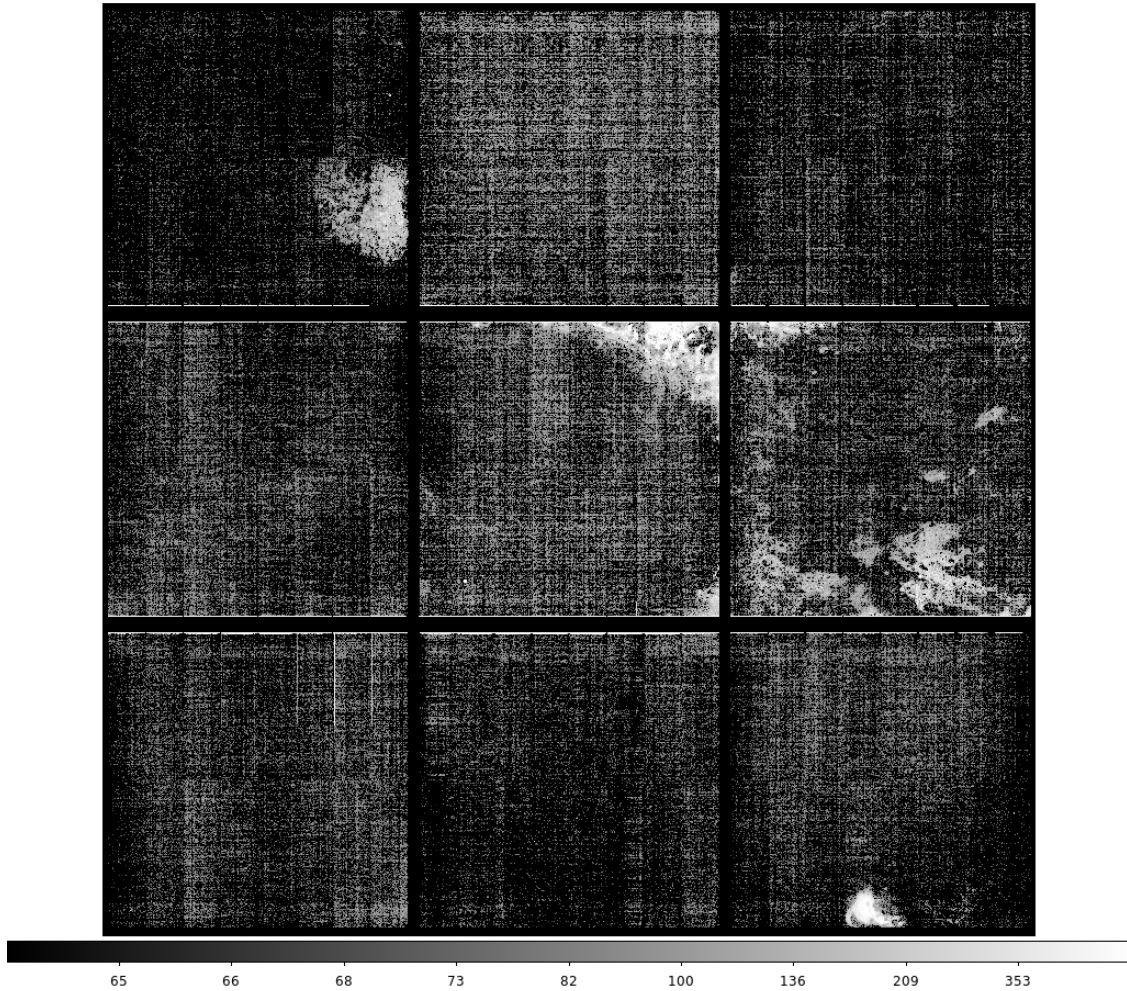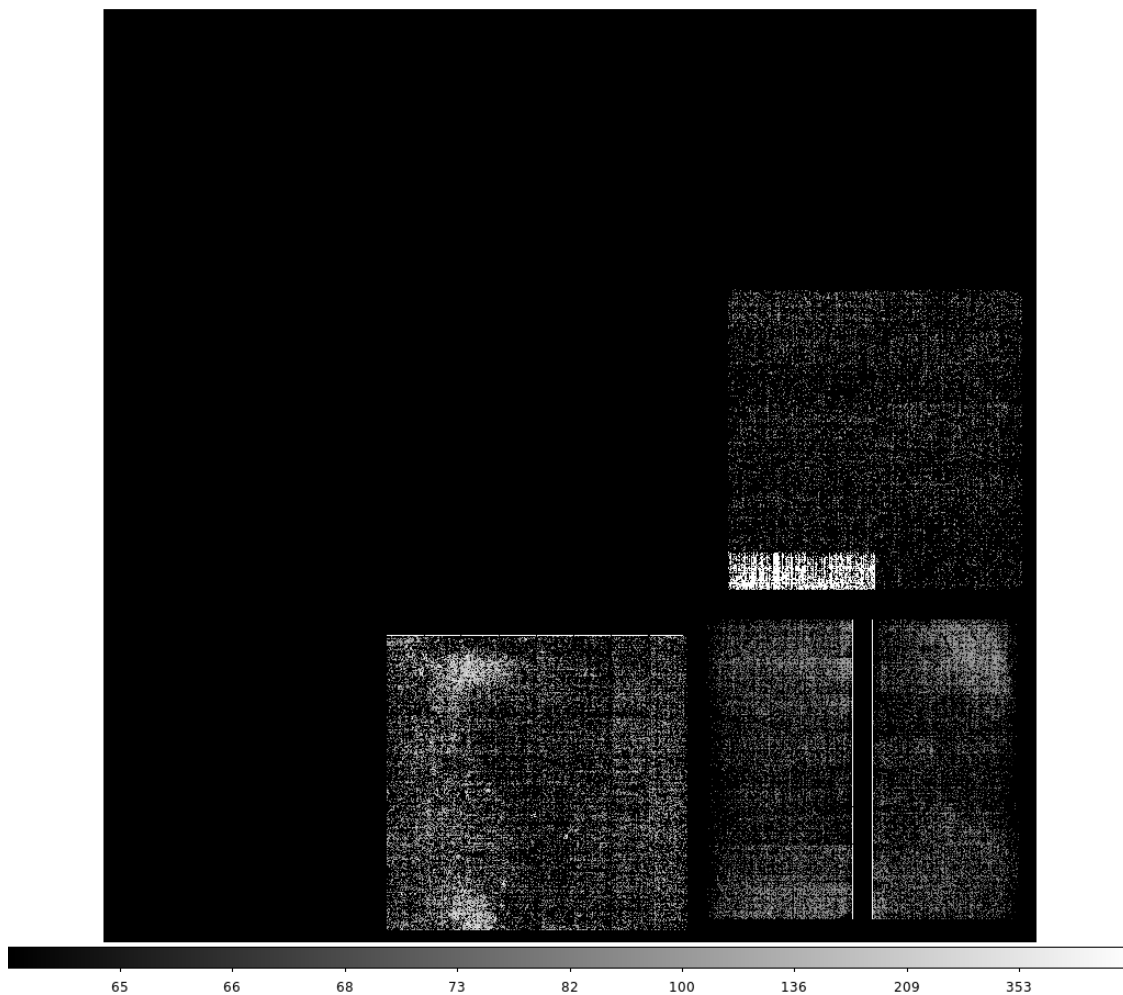
Figure 50: Phosphorescence transients for the R02 RTM captured in the first 15 s following *red* CCOB LED at 400 ke/pix. With 8»8 blocking, the upper end of the color scale (640) corresponds to 10 e/pixel when averaged over 64 pixels contributing.
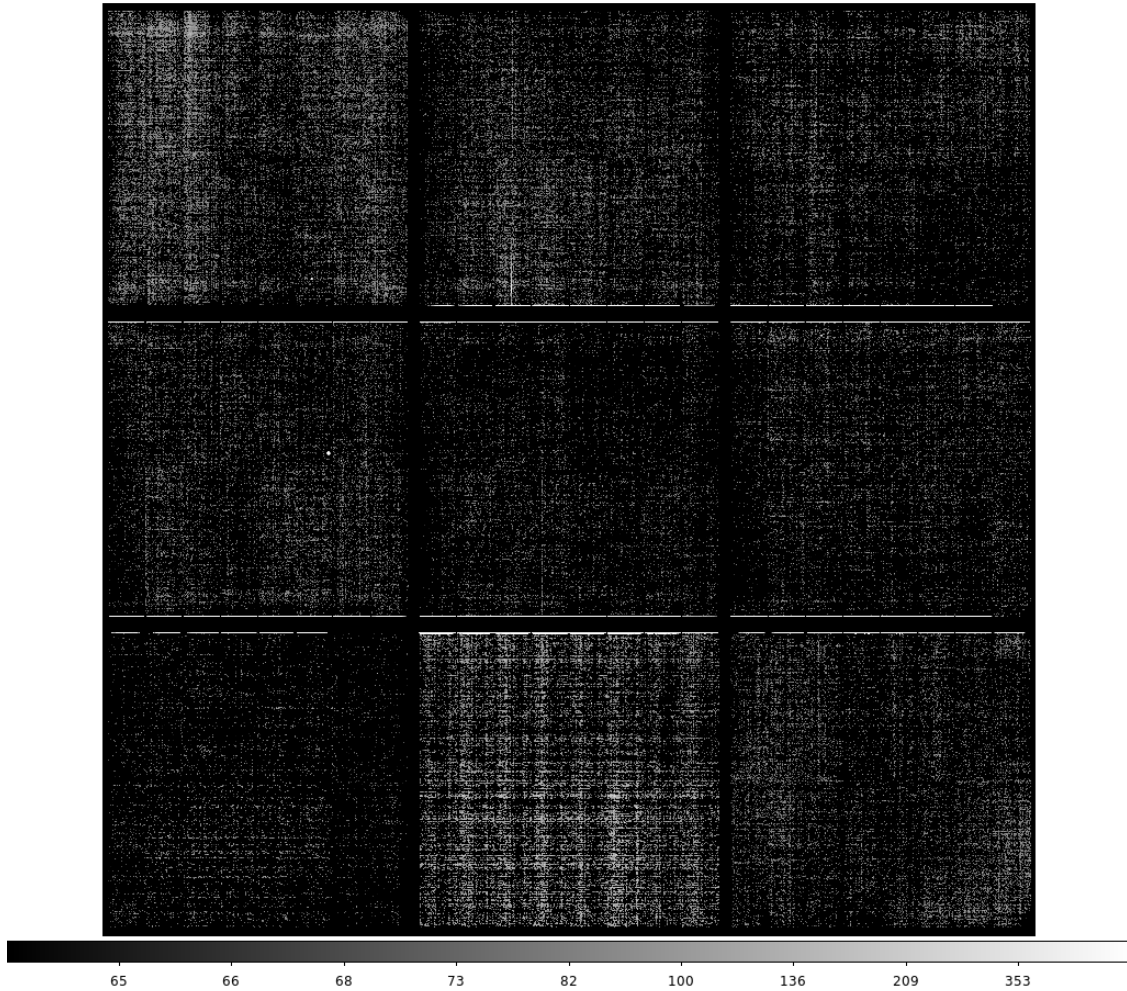
Figure 51: Phosphorescence transients for the R03 RTM captured in the first 15 s following *red* CCOB LED at 400 ke/pix. With 8»8 blocking, the upper end of the color scale (640) corresponds to 10 e/pixel when averaged over 64 pixels contributing.
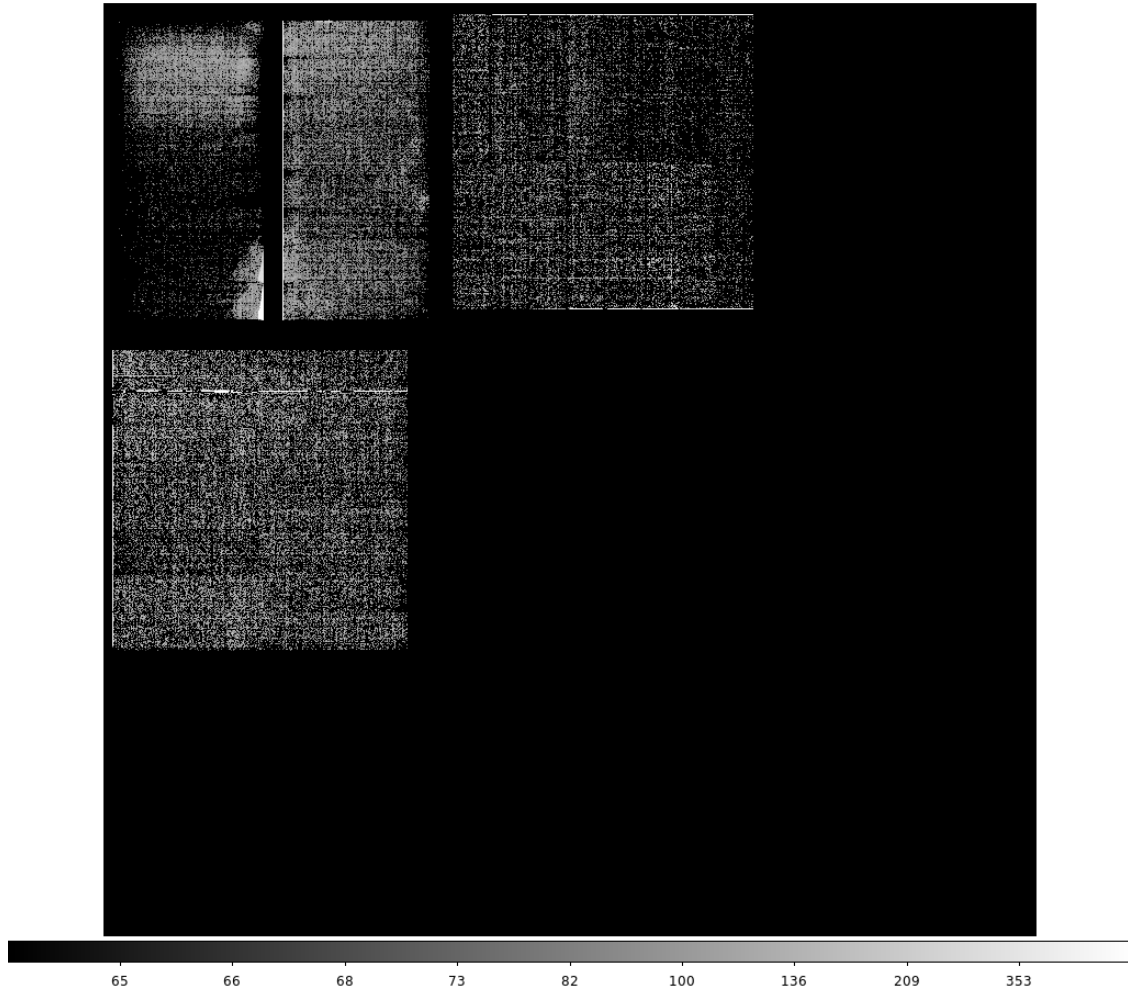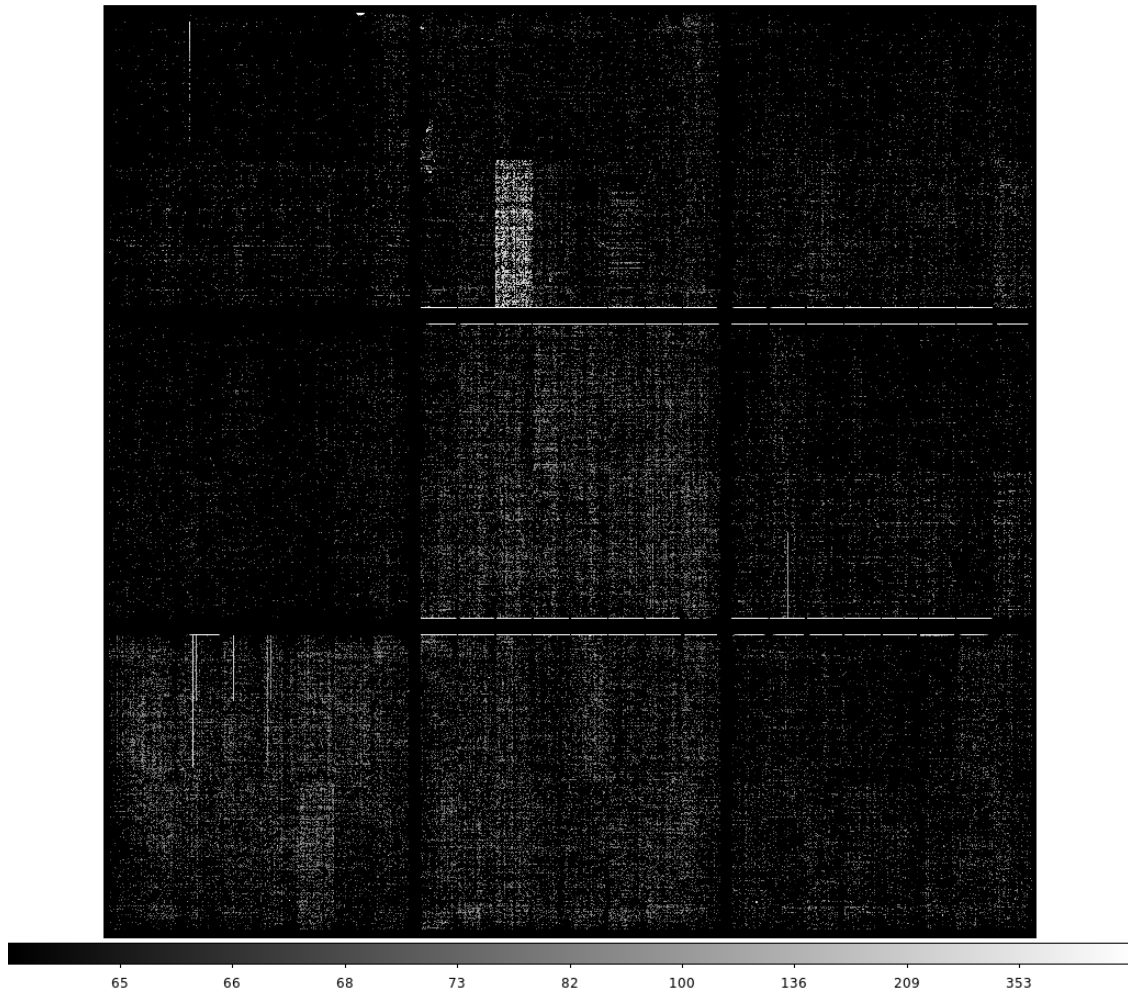
Figure 52: Phosphorescence transients for the R04 CRTM captured in the first 15 s following *red* CCOB LED at 400 ke/pix. With 8»8 blocking, the upper end of the color scale (640) corresponds to 10 e/pixel when averaged over 64 pixels contributing.
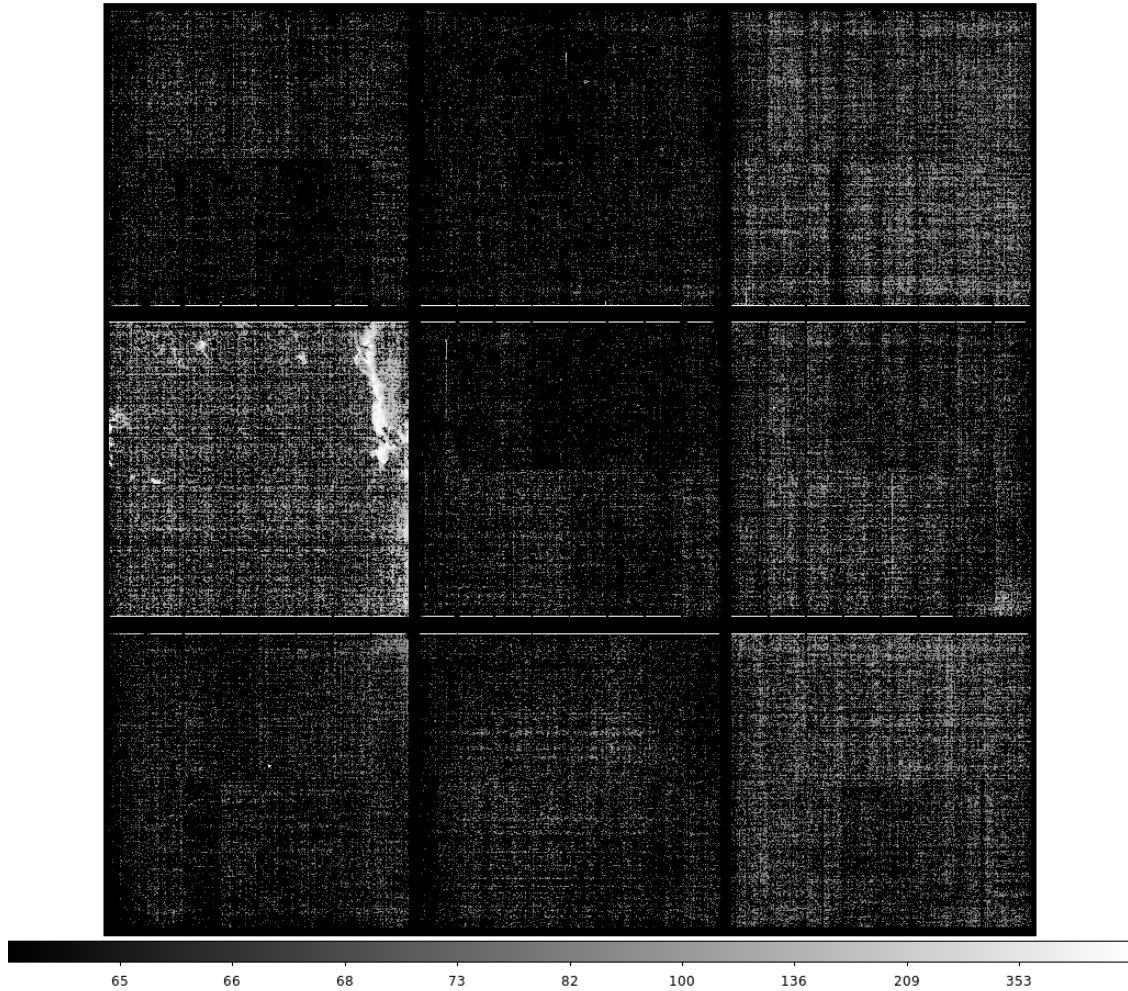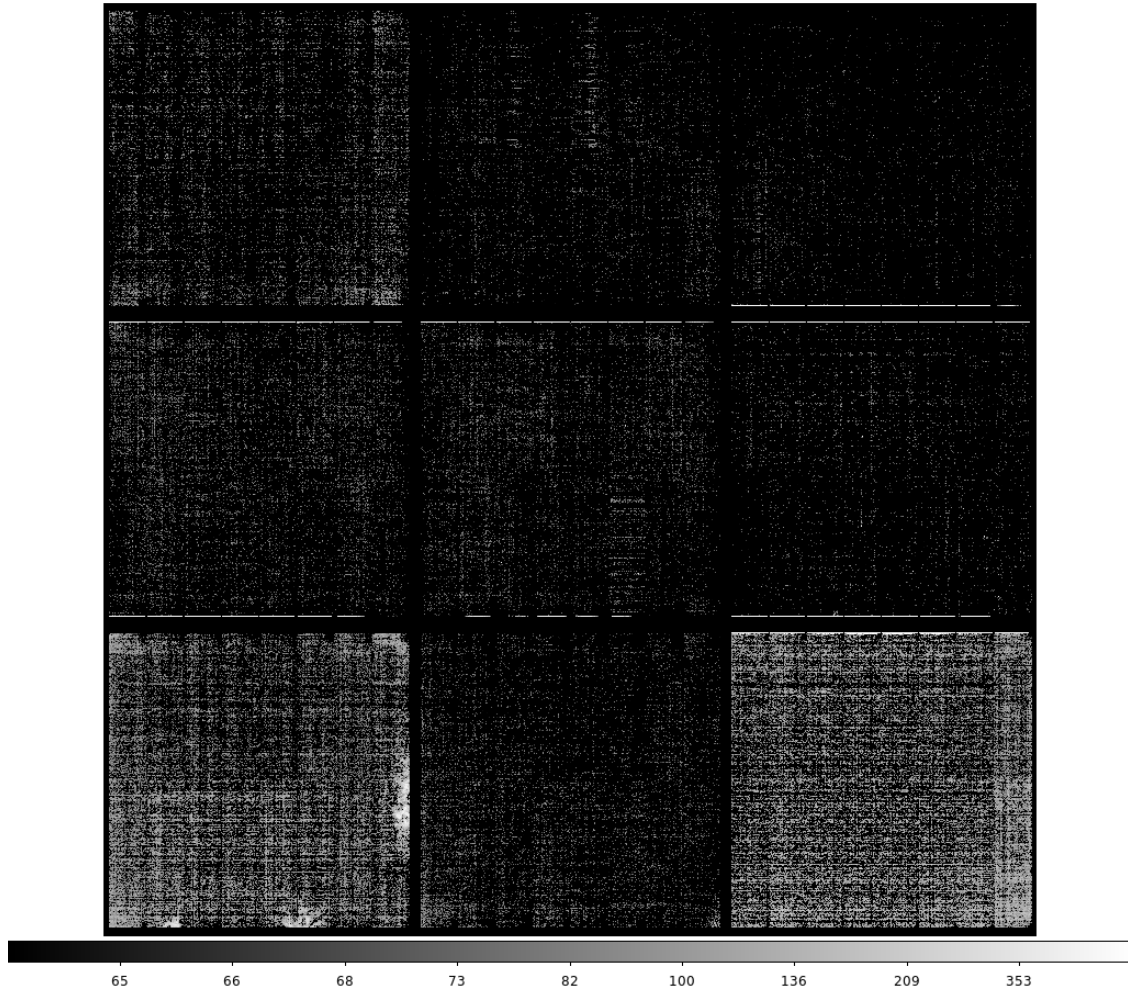
Figure 53: Phosphorescence transients for the R10 RTM captured in the first 15 s following *red* CCOB LED at 400 ke. With 8»8 blocking, the upper end of the color scale (640) corresponds to 10 e/pixel when averaged over 64 pixels contributing.
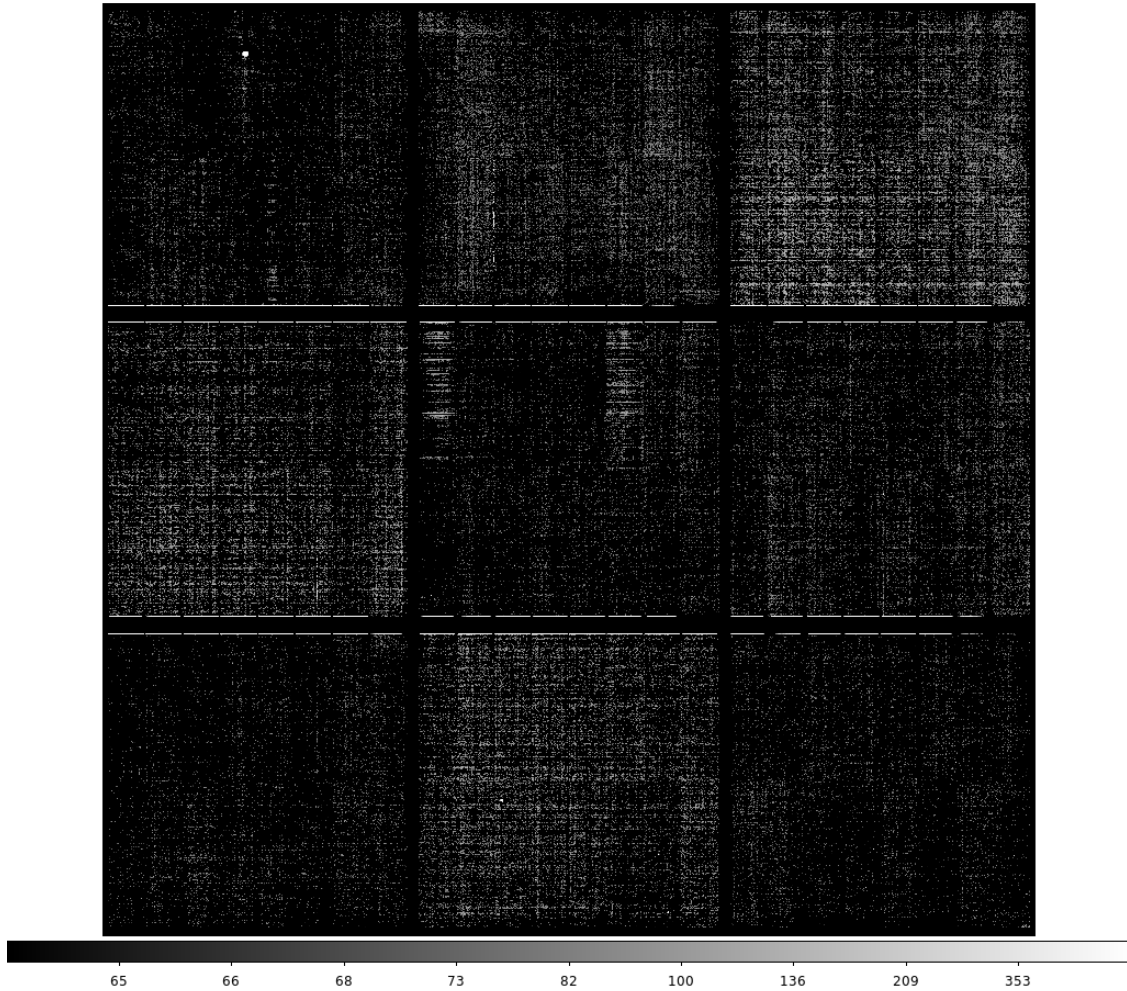
Figure 54: Phosphorescence transients for the R20 RTM captured in the first 15 s following *red* CCOB LED at 400 ke/pix. With 8»8 blocking, the upper end of the color scale (640) corresponds to 10 e/pixel when averaged over 64 pixels contributing.
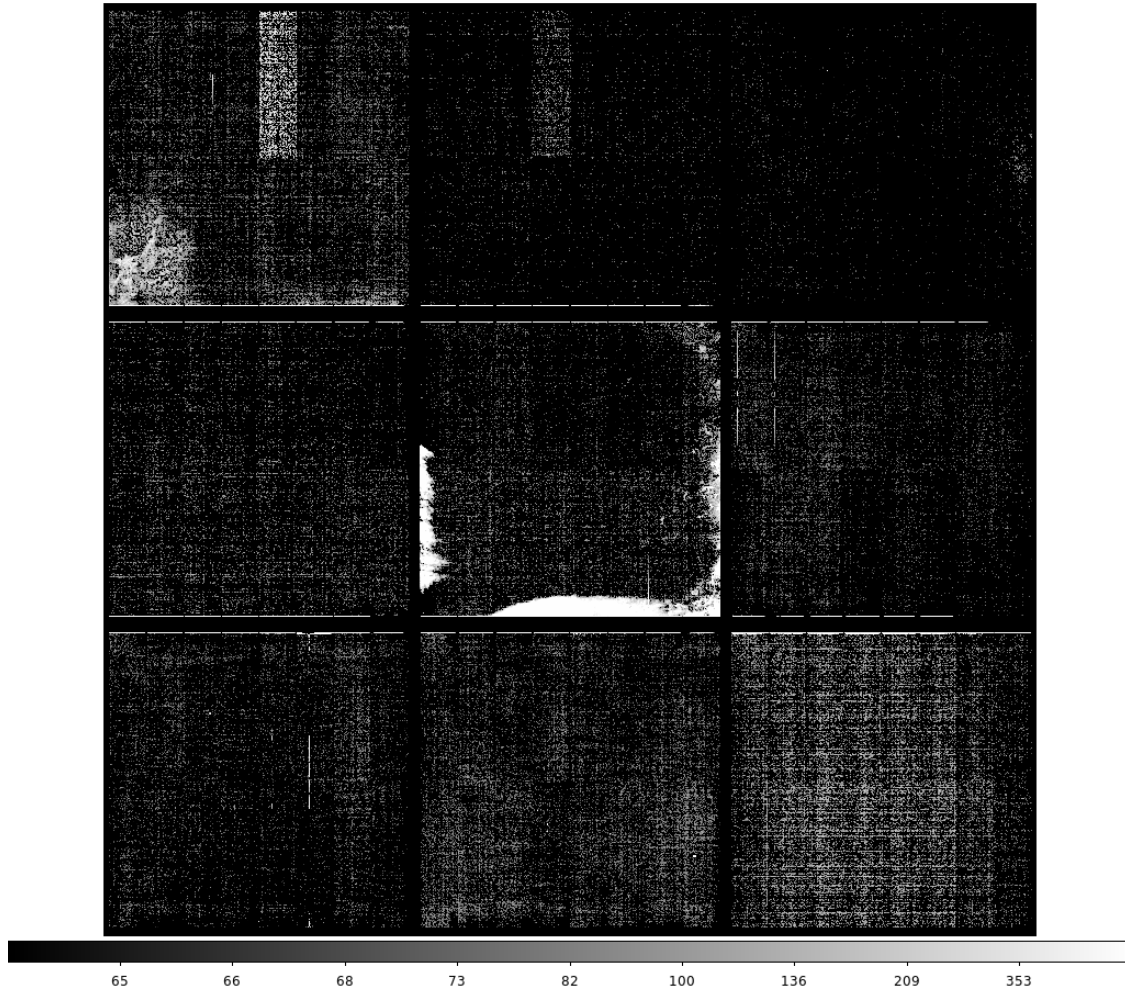
Figure 55: Phosphorescence transients for the R40 CRTM captured in the first 15 s following *red* CCOB LED at 400 ke/pix. With 8»8 blocking, the upper end of the color scale (640) corresponds to 10 e/pixel when averaged over 64 pixels contributing.
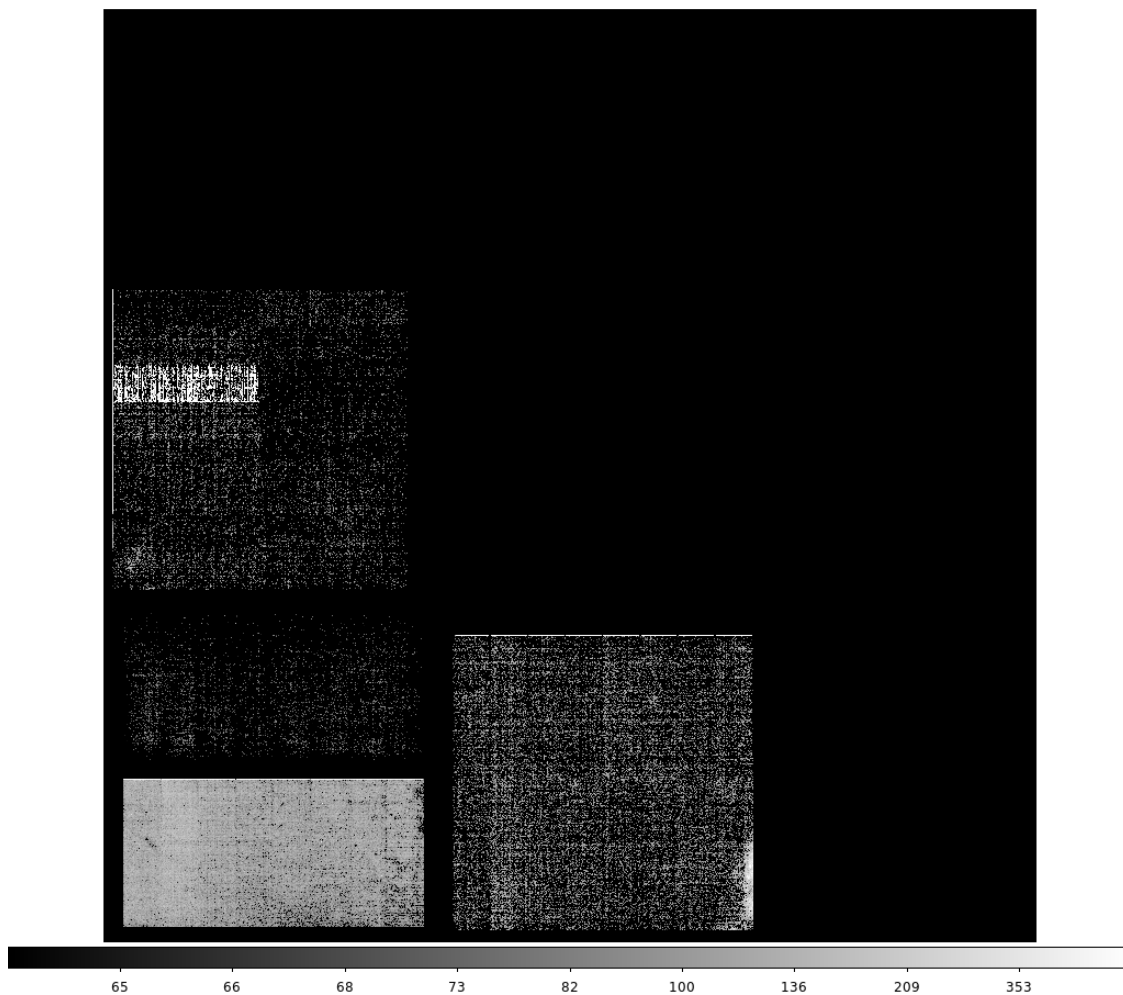
Figure 56: Phosphorescence transients for the R41 RTM captured in the first 15 s following *red* CCOB LED at 400 ke/pix. With 8»8 blocking, the upper end of the color scale (640) corresponds to 10 e/pixel when averaged over 64 pixels contributing.

Figure 57: Phosphorescence transients for the R42 RTM captured in the first 15 s following *red* CCOB LED at 400 ke/pix. With 8»8 blocking, the upper end of the color scale (640) corresponds to 10 e/pixel when averaged over 64 pixels contributing.
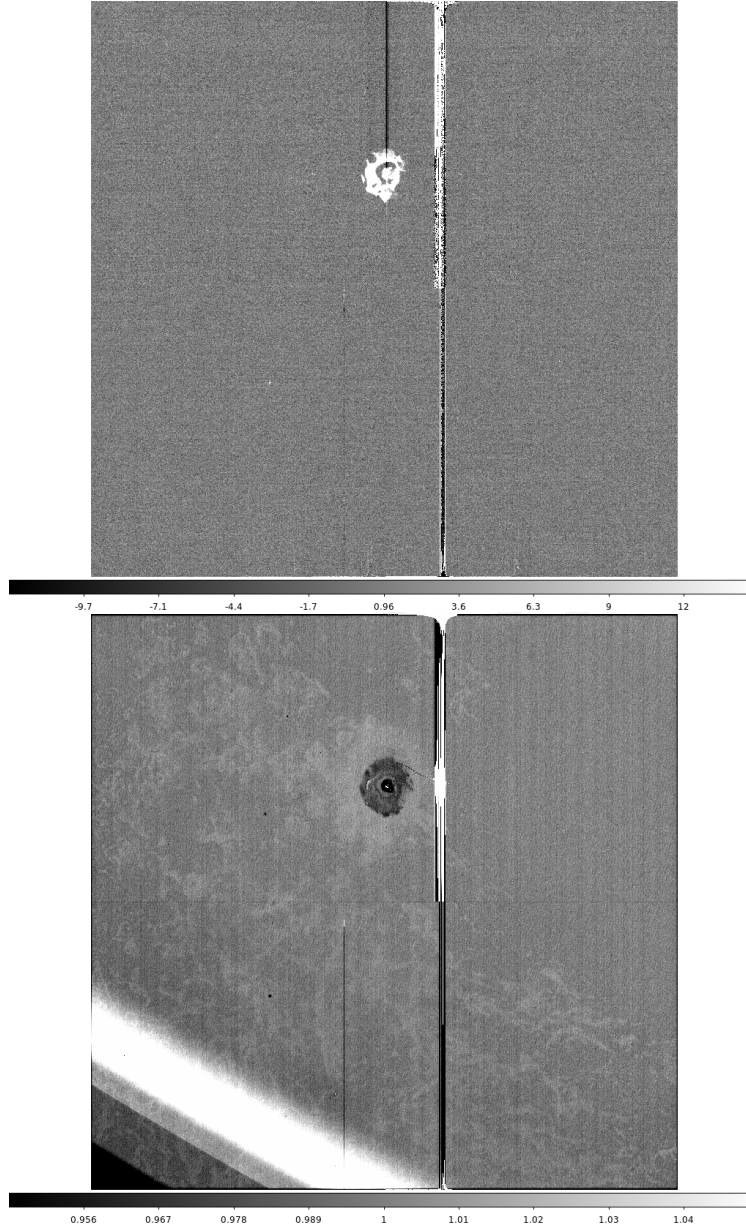
Figure 58: Phosphorescence transients for the R43 RTM captured in the first 15 s following *red* CCOB LED at 400 ke/pix. With 8»8 blocking, the upper end of the color scale (640) corresponds to 10 e/pixel when averaged over 64 pixels contributing.

Figure 59: Phosphorescence transients for the R44 CRTM captured in the first 15 s following *red* CCOB LED at 400 ke/pix. With 8»8 blocking, the upper end of the color scale (640) corresponds to 10 e/pixel when averaged over 64 pixels contributing.

Figure 60: The ITL sensor R01_S00. Top: the transient phosphorescence term. Bottom: the *blue* flat response. The large, extended spot appears to be centered on a *vampire pixel*, which also expresses a large amplitude of phosphorescence, which emits enough current to contaminate the parallel overscan in at least the first 15 s exposure following trigger. The flat response feature has opposite polarity from the phosphorescence.
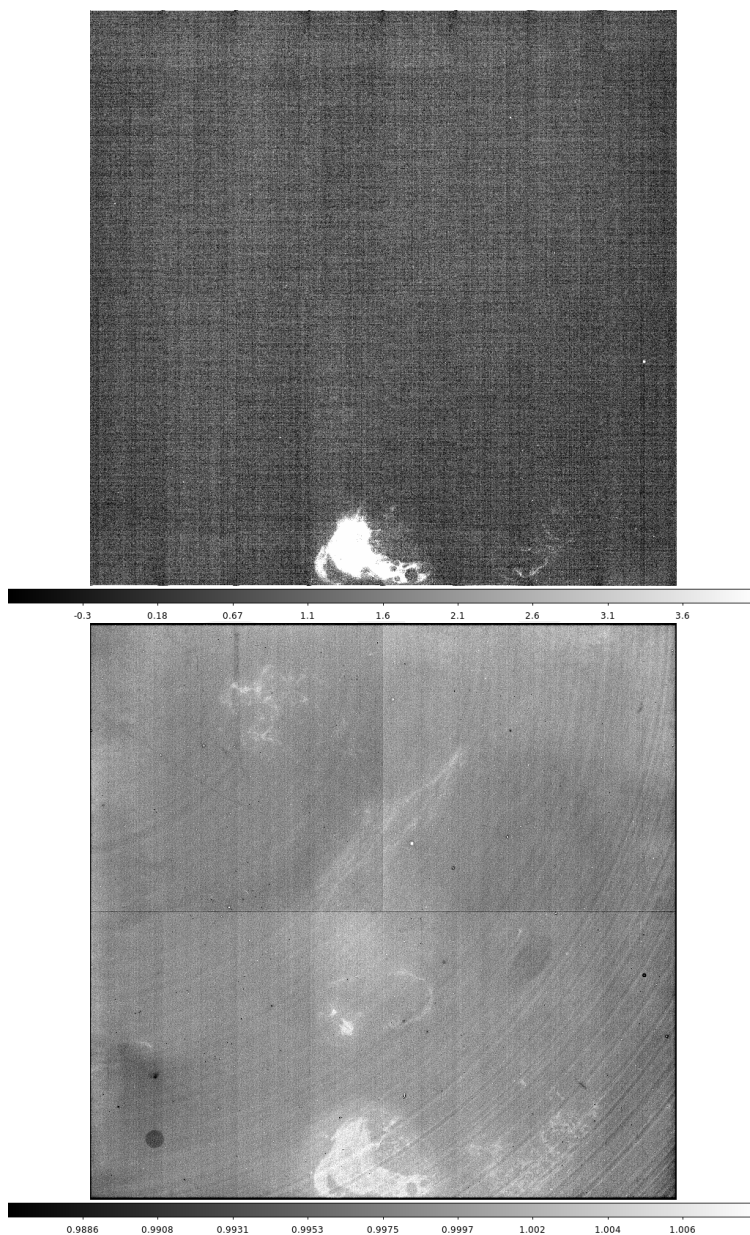
Figure 61: The ITL sensor R02_S02. Top: the transient phosphorescence term. Bottom: the *blue* flat response. The *coffee stain* feature in the flat response has the same polarity as the phosphorescence. A phosphorescent *vampire pixel* is seen in segment R02_S02_C07.
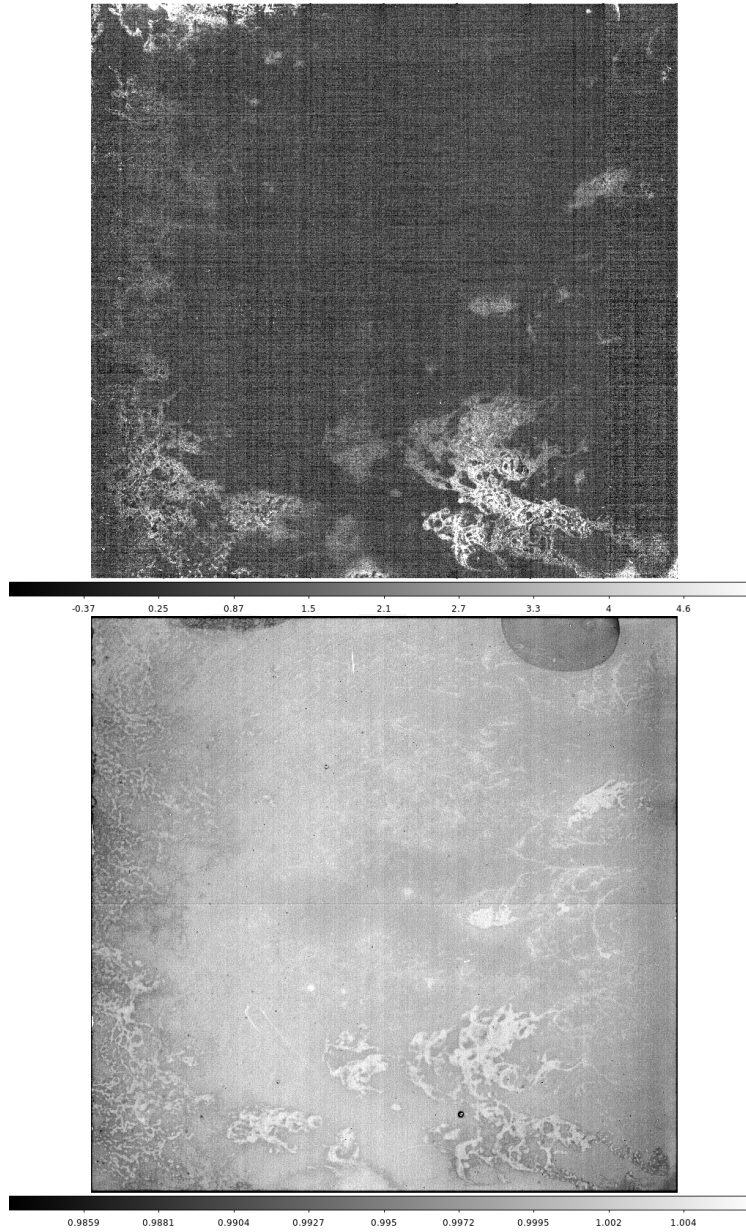
Figure 62: The ITL sensor R02_S12. Top: the transient phosphorescence term. Bottom: the *blue* flat response. Generally the polarity of the phosphorescence matches that of the *coffee stain* in the flat field response, but exceptions include the *vampire pixel* seen in segment R02_S12_C05.
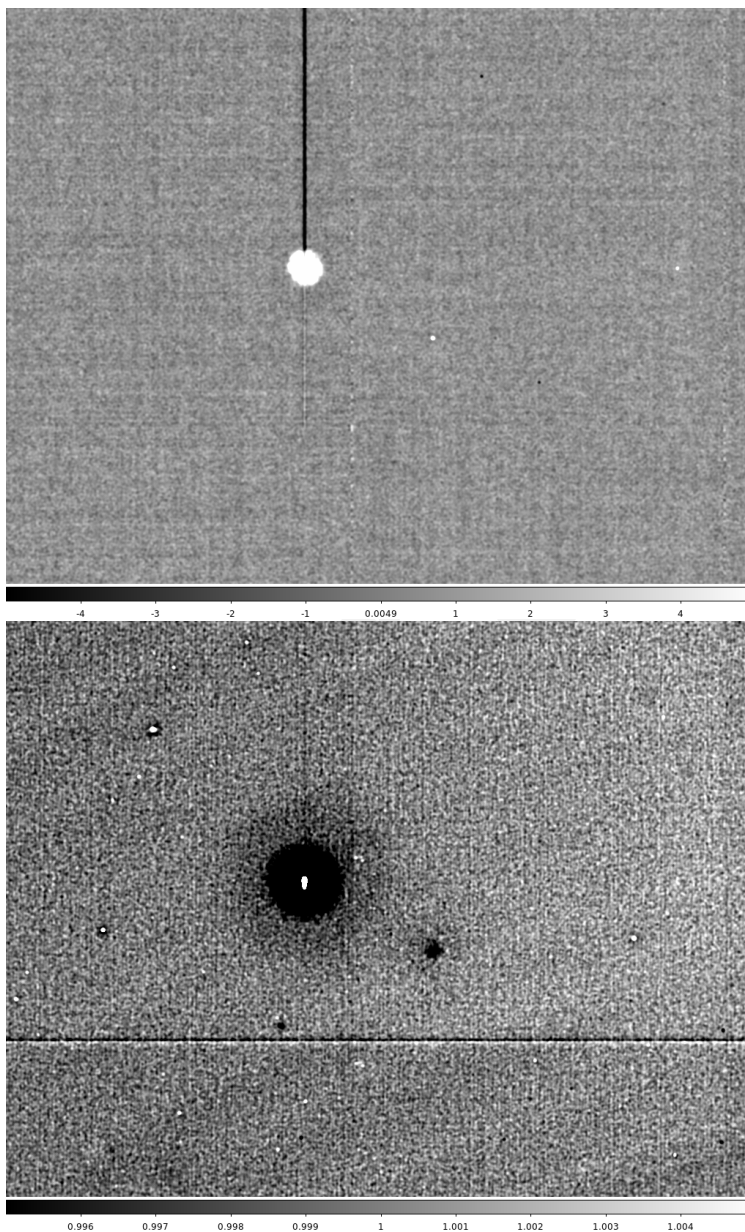
Figure 63: The ITL sensor R03_S10, detail of the *vampire pixel* of R03_S10_C15. Top: the transient phosphorescence term. Bottom: the *blue* flat response. As in previous examples, this *vampire pixel*'s transient term is large enough to contaminate the parallel overscan even after the first 15 s following trigger.
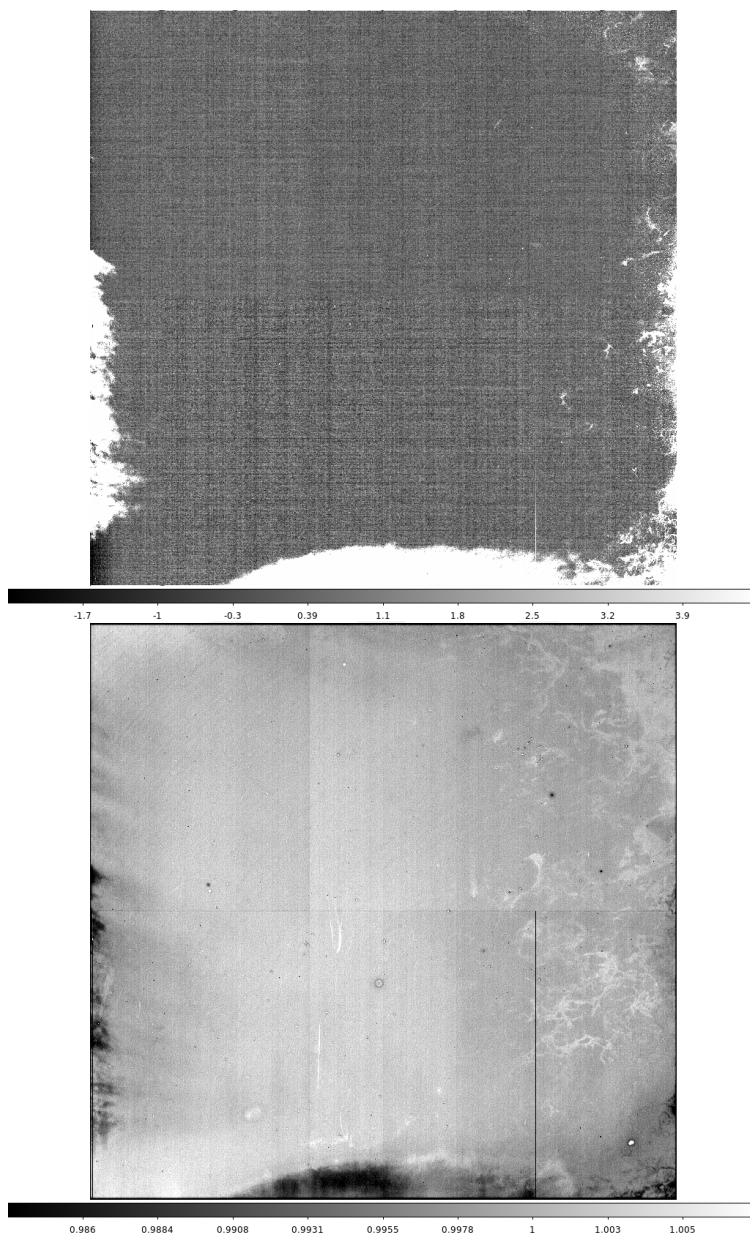
Figure 64: The ITL sensor R43_S11. Top: the transient phosphorescence term. Bottom: the *blue* flat response. This sensor appears to have the largest integrated phosphorescence among ITL sensors studied. The flat response feature has opposite polarity from the phosphorescence.
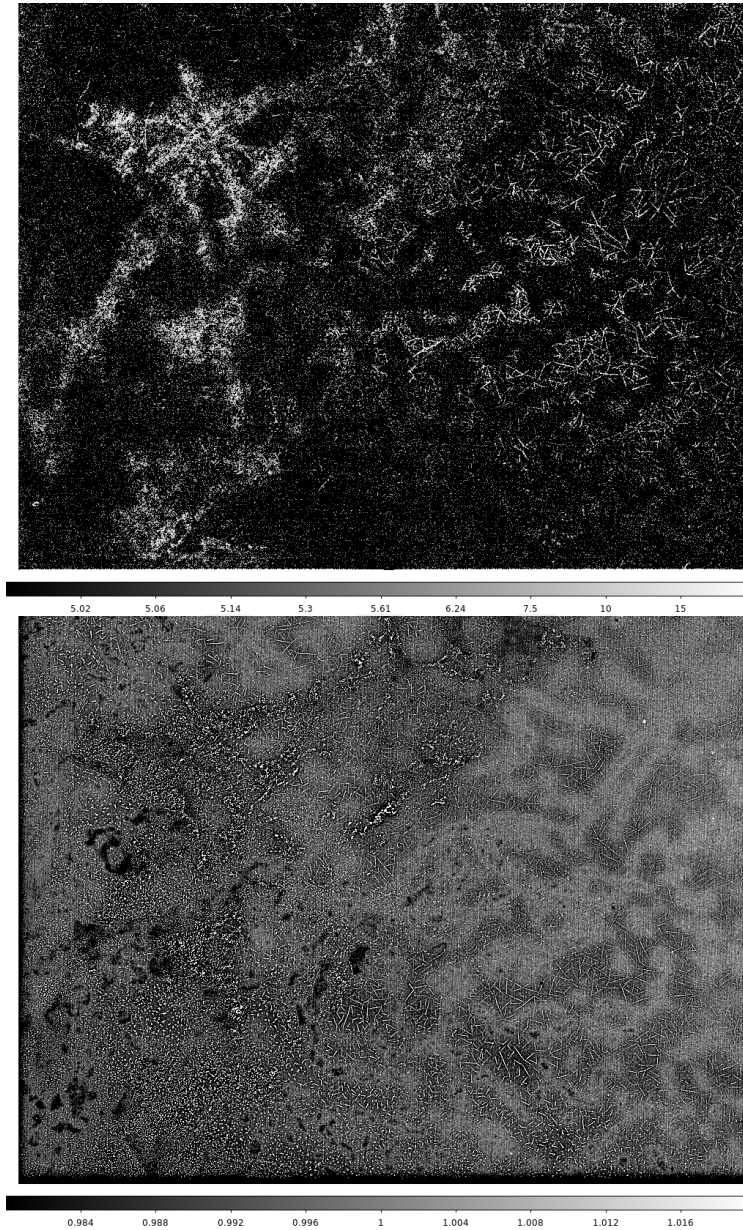
Figure 65: The ITL sensor R43_S20, segments C00 through C03. Top: the transient phosphorescence term. Bottom: the *blue* flat response. This sensor apparently exhibits peculiar radial crazing patterns seen in both phosphorescence as well as in flat field response, with polarities aligned.